COMPUTATIONAL STUDY OF STRUCTURAL, ELASTIC, ELECTRONIC, AND OPTICAL PROPERTIES OF SULFUR SUBSTITUTED PEROVSKITES, ATaO$_{3-x}$S$_x$ (A = K, Rb, Cs)

By

Hasina Akter

MSc in Physics

Student ID: 20MSPHY002F

A thesis submitted in partial fulfilment of the requirements for the degree of
MASTER of SCIENCE in Physics

Department of Physics

CHITTAGONG UNIVERSITY OF ENGINEERING AND TECHNOLOGY

May 2024

CERTIFICATION

The thesis titled "COMPUTATIONAL STUDY OF STRUCTURAL, ELASTIC, ELECTRONIC, AND OPTICAL PROPERTIES OF SULFUR SUBSTITUTED PEROVSKITES, $ATaO_{3-x}S_x$ (A = K, Rb, Cs)", submitted by **Hasina Akter,** Roll No. 20MSPHY002F, Session: 2020-2021 has been accepted as satisfactory in partial fulfilment of the requirement for the degree of Master of Science in Physics on 30 May 2024.

BOARD OF EXAMINERS

1. ______________________________

Dr. Md. Ashraf Ali (Supervisor) — Chairman
Professor
Department of Physics
Chittagong University of Engineering and Technology
Chattogram-4349

2. ______________________________

Head — Member (Ex-Officio)
Department of Physics
Chittagong University of Engineering and Technology
Chattogram-4349

3. ______________________________

Dr. Nusrat Jahan — Member
Professor
Department of Physics
Chittagong University of Engineering and Technology
Chattogram-4349

4. ______________________________ — Member (External)

Dr. Md. Khalilur Rahman Khan
Professor
University of Rajshahi (RU)
Department of Physics
Rajshahi-6000

Declaration

I hereby declare that the work contained in this thesis has not been previously submitted to meet the requirements for an award at this or any other higher education institution. To the best of my knowledge and belief, the Thesis contains no material previously published or written by another person except where due reference is cited. Furthermore, the Thesis complies with the PLAGIARISM and ACADEMIC INTEGRITY regulations of CUET.

Hasina Akter
20MSPHY002F
Department of Physics
Chittagong University of Engineering & Technology (CUET)

Dedication

I dedicate this thesis to my beloved parents, who brought me into this world and nurtured me from childhood to the person I am today.

List of Publications

Journal Article

1. Akter H, Hossain MM, Uddin MM, Naqib SH, Ali MA. Effects of S substitution on the structural, optoelectronic, and thermomechanical properties of $KTaO_3$ through density functional theory. Journal of Physics and Chemistry of Solids 2024;190:112021. https://doi.org/10.1016/j.jpcs.2024.112021.
2. Akter H, Ali MA, Hossain MM, Uddin MM, Naqib SH. Oxysulfide perovskites: reduction of the electronic band gap of $RbTaO_3$ by sulfur substitution. Physica Scripta 2024;99:045950. https://doi.org/10.1088/1402-4896/ad31f3.

Conference

1. Structural phase transition and the effect of Sulfur substitution on the physical properties of $KTaO_3$: a DFT insights. H. Akter, M. A. Ali, M. M. Hossain, M. M. Uddin, S. H. Naqib. 5th International conference on "Physics for Sustainable Development & Technology (ICPSDT-2023)" 7-8 September 2023; organized by Department of Physics, CUET.

2. Effect of S Substitution on the Physical Properties of $RbTaO_3$. H. Akter, M. A. Ali, M. M. Hossain, M. M. Uddin and S. H. Naqib. (National Conference on Physics -2023) 9-11 March, 2023; organized by Bangladesh Physical Society.

Approval/Declaration by the Supervisor(s)

This is to certify that Hasina Akter bearing roll number 20MSPHY002F has carried out this research work under my/our supervision and that she has fulfilled the relevant Academic Ordinance of the Chittagong University of Engineering and Technology so that she is qualified to submit the following Thesis in the application for the degree of MASTER OF SCIENCE in PHYSICS. Furthermore, the Thesis complies with the PLAGIARISM and ACADEMIC INTEGRITY regulations of CUET.

Dr. Md. Ashraf Ali
Professor
Department of Physics
Chittagong University of Engineering & Technology

Acknowledgement

I deeply appreciate the Almighty Allah's blessings and am thankful to my family for their continuous support, which played a crucial role in my academic achievement.

This work has been done on the supervision of Dr. Md. Ashraf Ali, Professor Department of physics Chittagong University of Engineering and Technology (CUET). I am deeply thankful to Dr. Md. Ashraf Ali for his invaluable mentorship and steadfast guidance throughout the journey of this thesis. His profound expertise, enduring patience, and consistent support have played a pivotal role in shaping the trajectory of my research.

I am also indebted to Prof. Dr. H.M.A.R. Maruf, the Head of the Physics Department at CUET, whose support throughout my research journey. I am grateful to Prof. Dr. Md. Mohi Uddin and Associate Prof. Dr. Md. Mukter Hossain for their invaluable guidance and support. I want to thank Dr. Mohammad Belal Hossen, Dr. Swapan Kumar Roy, Prof. Dr. Animesh Kumar Chakraborty, Prof. Dr. Nusrat Jahan, Mrs. Mosammat Arjumanara Bagum, Mr. Md Zahid Hasan, Sinthia Binte Kholil, and Mr. Md. Abdur Rahman for their support.

Furthermore, I express my profound gratitude to my elder sister Khaleda Akter and younger brother Abdullah Al Mubarak for their unwavering support and constant encouragement throughout this journey. Their belief in me has been a constant source of motivation, and I am truly grateful for their presence in my life.

I extend my thanks to the Department of Physics at CUET and UNESCO-TWAS for providing the necessary computing facilities at ACMRL, essential for this research endeavor.

May 2024 The Author

(Hasina Akter)

Abstract

In this study, the effects of sulfur substitution on the structural, mechanical, electronic, optical, and thermodynamic properties of $ATaO_{3-x}S_x$ have been investigated using the WIEN2k code in the framework of Density Functional Theory (DFT). The cubic phase of $ATaO_3$ (A= K, Rb and Cs) transforms to tetragonal for $ATaO_2S$ and $ATaOS_2$, the latter transforms again to a cubic phase with added sulfur for $ATaS_3$. The results indicated a notable reduction in the band gap upon substituting S for O anions in $ATaO_3$. Specifically, $KTaO_3$ exhibited a band gap of 3.57 eV, which subsequently decreased to 1.808 eV, 0.264 eV, and 0.078 eV for $KTaO_2S$, $KTaOS_2$, and $KTaS_3$, respectively. Similarly, $RbTaO_3$ exhibit a reduction in its band gap from 2.717 eV to 1.438 eV, 0.286 eV, and 0.103 eV for $RbTaO_2S$, $RbTaOS_2$, and $RbTaS_3$ compounds. $CsTaO_3$ had an initial band gap of 3.076 eV, which decreased to 0.909 eV, 0.376 eV, and 0.143 eV for $CsTaO_2S$, $CsTaOS_2$, and $CsTaS_3$ compounds, respectively. Furthermore, these compounds have displayed promising optical characteristics characterized by high absorption coefficients ($\sim 10^6$ cm^{-1}), minimal reflectivity (<30%), and robust optical conductivity within the visible spectrum, making them ideal candidates for a range of optoelectronic technologies. Our comprehensive investigation has reinforced the stability of all computed phases, showcasing exceptional electronic, mechanical, and optical properties, including semiconducting behavior, ductility, anisotropy, high absorptivity, and low reflectivity. The altered band gap and optical features observed in $KTaO_2S$ and $RbTaO_2S$ suggest significant potential for their utilization in solar cells, offering promising prospects for enhancing solar energy conversion efficiency. Additionally, the elevated lattice thermal conductivity observed in $KTaO_3$, $RbTaO_3$, and $CsTaO_3$ indicates their potential as promising candidates for heat sink materials.

বিমূর্ত

এই গবেষণায়, $ATaO_3$ এর structural, mechanical, electronic, optical, এবং thermodynamic বৈশিষ্ট্যের উপর S-প্রতিস্থাপনের প্রভাব, Density Functional Theory (DFT) এর ভিত্তিতে WIEN2k কোড ব্যবহার করে পর্যবেক্ষণ করা হয়েছে। $ATaO_3$ (A= K, Rb এবং Cs) এর cubic পর্যায়টি $ATaO_2S$ এবং $ATaOS_2$ এর জন্য tetragonal-এ রূপান্তরিত হয়, যা আরো S- প্রতিস্থাপনে ($ATaS_3$) পুনরায় cubic-এ রূপান্তরিত হয়। ফলাফলগুলো $ATaO_3$ এ O anions-এর জন্য S প্রতিস্থাপন করার পরে band gap একটি উল্লেখযোগ্য হ্রাস প্রদর্শন করে। বিশেষভাবে, $KTaO_3$ -এর band gap 3.57 eV প্রদর্শন করেছে, যা পরবর্তীতে $KTaO_2S$, $KTaOS_2$ এবং $KTaS_3$-এর জন্য যথাক্রমে 1.808 eV, 0.264 eV, এবং 0.078 eV-এ কমে এসেছে। একইভাবে, $RbTaO_3$ এর জন্য, $RbTaO_2S$, $RbTaOS_2$, এবং $RbTaS_3$ যৌগগুলোর জন্য band gap 2.717 eV থেকে 1.438 eV, 0.286 eV, এবং 0.103 eV-এ হ্রাস পেয়েছো $CsTaO_3$-এর প্রাথমিক band gap ছিল 3.076 eV, যা $CsTaO_2S$, $CsTaOS_2$ এবং $CsTaS_3$ যৌগের জন্য যথাক্রমে 0.909 eV, 0.376 eV এবং 0.143 eV- এ কমেছে। অধিকন্তু, এই যৌগগুলো high optical absorption coefficient (~10^6 cm), low optical reflectivity (<30% এর মধ্যে) এবং high optical conductivity দ্বারা আমাদের গবেষণাকৃত যৌগগুলোর, অপটোইলেকট্রনিক ক্ষেত্রে ব্যবহারের জন্য উপযুক্ততা প্রদর্শন করে । আমাদের বিস্তৃত অনুসন্ধান যৌগগুলোর stability, electronic, mechanical এবং optical বৈশিষ্ট্যগুলো প্রদর্শন করে, যার মধ্যে রয়েছে semiconducting behavior, brittleness, anisotropy, high optical absorption coefficient এবং low optical reflectivity । $KTaO_2S$ এবং $RbTaO_2S$ তে পরিবর্তিত band gap এবং optical বৈশিষ্ট্যগুলো সৌর কোষে তাদের ব্যবহারের সম্ভাবনা, সৌর শক্তি রূপান্তর দক্ষতা বাড়ানোর সক্ষমতা নির্দেশ করে । অতিরিক্তভাবে, $KTaO_3$, $RbTaO_3$, এবং $CsTaO_3$ এ high lattice thermal conductivity, এদের heat sink materials হিসেবে ব্যবহারের জন্য সম্ভাবনা নির্দেশ করে ।

Table of Contents

CHAPTER 3: THEORETICAL METHODOLOGY …….………..………......22

CHAPTER 4: Results & Discussion ………………………………..……….......45

List of Figures

List of Tables

Abbreviations

AE	All-Electron
AO	Atomic Orbital
BF	Block Function
BO	Born –Oppenheimer
BZ	Brillouin Zone
CO	Crystal Orbital
DF	Density Functional
DFPT	Density Functional perturbation Theory
DFT	Density Functional Theory
DOS	Density Of States
ECP	Effective Core Potential
eV	Electron Volts
GGA	Generalized Gradient Approximation
GPa	Giga Pascals
GS	Ground State
GSES	Ground States Electronic Structure
GTOs	Gaussian Type Functions
HF	Hartree-Fock

IR	Infrared
KS	Kohn and sham
LCAO	Linear Combination of Atomic Orbital
LDA	Local Density Approximation
LO	Longitudinal Optical
PBE	Perdew, Burke, and Ernzerhof
PDOS	Projected Density of States/ Partial Density of States
PP	Pseudopotential
PWPP	Plane Wave Pseudopotential
QST	Quadratic Synchronous Transit
RPBE	Revised Perdew-Burke-Ernzerhof
SAW	Surface Acoustic Wave
SCF	Self-Consistent Field
STOs	Slater Type Orbitals
TO	Transverse Optical
Tb-mBJ	Tran and Blaha modified Becke-Johnson potential
XC	Exchange Correlation
XRD	X-Ray Diffraction

Chapter 1: INTRODUCTION

1.1 Background

Perovskite compounds, which take their name from the Russian mineralogist Lev Perovski, have become central subjects of extensive research in materials science over the past few decades [1]. Their ABX_3 crystal structure, where A, B represent cations and X are anions, presents a unique foundation for their versatile properties and potential applications across diverse scientific and technological fields. Perovskites' intriguing crystal structure, characterized by a network involving sharing corners BX_6 octahedra with an A-site cation at the center, allows for remarkable structural flexibility and a wide range of tunable properties. Originating from Lev Perovski's discovery of the mineral perovskite in the early 19th century, the understanding and synthesis of perovskite materials gained momentum in the mid-20th century, leading to profound insights and numerous applications [2,3]. One of the distinguishing features of perovskite compounds is their ability to substitute elements at the A, B, and X sites, enabling precise control over their composition, morphology, and crystallinity. Various synthesis methods, incorporating solid-state reactions together with sol-gel scheme, and solution-based techniques like the perovskite precursor solution method, have been employed to tailor these materials according to specific requirements [4].

Several oxide perovskites, including $NaTaO_3$, $KTaO_3$, $BaZrO_3$, $SrTiO_3$, $BaTiO_3$, $CaTiO_3$, $LaFeO_3$, $EuAlO_3$, and $YMnO_3$, have exhibited favorable characteristics such as optical transparency, electrical conductivity, structural stability, and thermal properties. These materials have found utility in various domains, including energy harvesting, electronics, catalysis, sensing, and information storage. Notably, alkaline oxide perovskites like $KTaO_3$, $RbTaO_3$, and $CsTaO_3$ have garnered considerable attention due to their excellent thermal characteristics and electrical band gaps that fall within the visible region of the electromagnetic spectrum. These attributes make them particularly well-suited for applications in optoelectronics and photovoltaics [5–16]. Oxide perovskite materials, specifically $ATaO_3$ (A= K, Rb, Cs), present a formidable challenge for effective solar energy utilization due to their wide band gaps—$KTaO_3$ at 3.64 eV, $RbTaO_3$ at 2.75 eV, and $CsTaO_3$ at 3.15 eV [17,18]. These characteristics result in limited absorption of solar irradiation, particularly in the UV range. There is an imperative need to narrow their band gaps to unlock the solar energy potential of $ATaO_3$ [A = Rb, K, Cs] compounds. A promising avenue to achieve this involves the introduction of suitable anions at the oxygen (O) sites within the oxide perovskite structure. While traditional cation doping reduces the conduction band-edge potential, anion dopants at the O-sites present a novel and potentially more effective approach. Among these anion dopants, sulfur (S) emerges as a highly promising candidate due to its electron configuration resembling oxygen. By substituting O sites with S, $ATaO_3$ [A = Rb, K, Cs], compounds can transform, resulting in a shifted valence band edge and a remarkable band gap reduction by approximately 1.4 eV, all without introducing undesirable holes or defects. This innovative strategy finds support in recent theoretical discoveries. It draws parallels to the success of S-doped titanium dioxide (TiO_2), renowned for its capability to split water into hydrogen (H_2) and oxygen (O_2) [19]. Previous research has illuminated the efficacy of S-doping in reducing band gaps and enhancing visible-light activity in various perovskite materials, including sulfur-doped strontium titanate ($SrTiO_3$), barium titanate ($BaTiO_3$), and sodium tantalate ($NaTaO_3$) [20]. These studies have paved the way for investigating the reduction of the band gap in $ATaO_3$ through S doping, aiming to improve its solar energy utilization.

Our primary goal is to decrease the band gap of the previously synthesized Perovskite compound $ATaO_3$ [A = Rb, K, Cs]. Why is reducing the band gap essential? We are exploring applications of S-containing perovskites, aiming for their suitability in solar cell technology. Referring to the seminal work of W. Shockley and H. J. Queisser [21], achieving the highest solar cell efficiency requires a material with a band gap of around 1.43 eV. Reducing the band gap is vital for improving the electrical conductivity of semiconductor materials. With this goal in focus, our objective is to decrease the band gap of the specified oxide perovskite $ATaO_3$ by introducing anion doping.

1.2 Context

The versatility of perovskite materials and their diverse electronic and optical attributes make them promising candidates for various applications. While various oxide perovskites have already demonstrated favorable properties, including $BaTiO_3$, $NaTaO_3$, $BaZrO_3$, $SrTiO_3$, $KTaO_3$, $LaFeO_3$, $CaTiO_3$, $EuAlO_3$, and $YMnO_3$, their band gaps may need modification to meet the requirements of specific applications. This study focuses on S-doping to reduce band gaps and enhance the suitability of $RbTaO_3$, $KTaO_3$, and $CsTaO_3$ for solar cells, aligning with current research trends in materials science and energy technology.

1.3 Aims and Objectives

Aim: We intend to study the effect of S-substitution on the physical properties of oxide perovskite $ATaO_{3-x}S_x$ compounds [A = Rb, K, Cs]. The primary aim of this study is to reduce the band gap of oxide perovskite compounds, including $RbTaO_3$, $KTaO_3$, and $CsTaO_3$, through anion doping with sulfur (S). This reduction in band gap is sought to make these materials suitable for solar cell technology applications. Achieving a band gap of approximately 1.43 eV is critical for maximizing the efficiency of solar cells, as demonstrated by the work of W. Shockley and H. J. Queisser [21].

Objectives:

1. Investigation of the crystalline substance and determination of the lattice parameters of $ATaO_{3-x}Sx$ perovskite compounds using Wien2K [22] based on Density Functional Theory (DFT) [23].
2. Verification of the phase stability by calculating formation energy, phonon dispersion curves, and elastic constants.
3. Study of the electronic band structure and density of states of $ATaO_{3-x}S_x$ [A = Rb, K, Cs] compounds, with the aim of reducing the band gap in $RbTaO_3$, $KTaO_3$, and $CsTaO_3$ through S doping to enhance their suitability for solar cell applications.
4. Analyzing the optical properties of $ATaO_{3-x}S_x$ [A = Rb, K, Cs] perovskite compounds, including their light absorption capacity, reflectivity spectra, and photoconductivity, to gain insights into their performance in optoelectronic devices.
5. Evaluation of the mechanical properties of $ATaO_{3-x}S_x$ [A = Rb, K, Cs] compounds and their elastic anisotropic behavior to assess their structural integrity and reliability.
6. Exploration of the thermal characteristics of $ATaO_{3-x}S_x$ [A = Rb, K, Cs] compounds to comprehend their behavior under varying temperature conditions and their suitability for heat-seeking technology.

1.4 Significant Scope and Defination:

This thesis explores paramount significance, focusing on the transformative potential of sulfur (S) doping to reduce band gaps in oxide perovskite compounds, specifically $KTaO_3$, $RbTaO_3$, and $CsTaO_3$. The goal is to enhance their viability for advanced solar cell applications, aligning with the pioneering work of W. Shockley and H. J. Queisser [21]. The investigation encompasses a multifaceted approach, delving into the crystal structure, phase stability, electronic properties, optical attributes, mechanical behaviors, vibrational dynamics, and thermal characteristics of these materials. The strategic reduction of the band gap, orchestrated through S substitution, holds the promise of maximizing the efficiency of solar cells, making this research a significant contribution to materials science and renewable energy technology.

1.5 Thesis Outline:

This thesis is organized into several chapters to present the research and its findings systematically. The outline of the thesis is as follows:

Chapter 1 (Introduction): The significance of perovskite structures in science and technology, focusing on band gap modification in semiconductor materials. We introduce the core investigation S doping in oxide perovskite compounds for optoelectronic applications.

Chapter 2 (Literature Review): A comprehensive review of relevant literature on perovskite materials, their properties, and the impact of anion doping on band gaps and conductivity.

Chapter 3 (Methodology): Details the computational methods and techniques used to study S-doped $RbTaO_3$, $KTaO_3$, and $CsTaO_3$, including density functional theory (DFT) calculations.

Chapter 4 (Results and Discussion): Demonstrates the results of the DFT-based calculations, including changes in band gaps, electronic structures, and thermal conductivity, and discusses their implications.

Chapter 5 (Conclusion): This thesis summarizes research findings, emphasizing their significance in advancing our understanding of $ATaO_3$ perovskite compounds. It highlights the contribution to the exploration of their characteristics and potential applications. Furthermore, this chapter include the future research directions and recommendations for further exploration.

References:

[1] Yuan Y, Huang J. Ion Migration in Organometal Trihalide Perovskite and Its Impact on Photovoltaic Efficiency and Stability. Acc Chem Res 2016;49:286–93. https://doi.org/10.1021/acs.accounts.5b00420.

[2] Editorial BR. A History of Perovskite Solar Cells n.d. https://blog.bccresearch.com/a-history-of-perovskite-solar-cells (accessed October 16, 2023).

[3] Katz E. Perovskite: Name Puzzle and German-Russian Odyssey of Discovery. Helvetica Chimica Acta 2020;103. https://doi.org/10.1002/hlca.202000061.

[4] Assirey EAR. Perovskite synthesis, properties and their related biochemical and industrial application. Saudi Pharmaceutical Journal 2019;27:817–29. https://doi.org/10.1016/j.jsps.2019.05.003.

[5] Fresno F, Jana P, Reñones P, Coronado JM, Serrano DP, de la Peña O'Shea VA. CO_2 reduction over $NaNbO_3$ and $NaTaO_3$ perovskite photocatalysts. Photochem Photobiol Sci 2017;16:17–23. https://doi.org/10.1039/c6pp00235h.

[6] Modak B, Ghosh SK. Improving visible light photocatalytic activity of $KTaO_3$ using cation-anion dopant pair. Solar Energy Materials and Solar Cells 2017;159:590–98. https://doi.org/10.1016/j.solmat.2016.10.003.

[7] Meng J, Lan Z, Lin Q, Chen T, Chen X, Wei X, et al. Cubic-like $BaZrO_3$ nanocrystals with exposed {001}/{011} facets and tuned electronic band structure for enhanced photocatalytic hydrogen production. J Mater Sci 2019;54:1967–76. https://doi.org/10.1007/s10853-018-2995-8.

[8] Ying Z, Chen S, Peng T, Li R, Zhang J. Fabrication of an Fe-Doped $SrTiO_3$ Photocatalyst with Enhanced Dinitrogen Photofixation Performance. European Journal of Inorganic Chemistry 2019;2019:2182–92. https://doi.org/10.1002/ejic.201900098.

[9] Karthik KV, Reddy ChV, Reddy KR, Ravishankar R, Sanjeev G, Kulkarni RV, et al. Barium titanate nanostructures for photocatalytic hydrogen generation and photodegradation of chemical pollutants. J Mater Sci: Mater Electron 2019;30:20646–53. https://doi.org/10.1007/s10854-019-02430-6.

[10] Ferrari AM, Germiniano TO, Savoia JE, Marques RG, Ribeiro VA dos S, Ueda AC. $CaTiO_3$ Perovskite in the Photocatalysis of Textile Wastewater. Rev Ambient Água 2019;14:e2336. https://doi.org/10.4136/ambi-agua.2336.

[11] Gong C, Zhang Z, Lin S, Wu Z, Sun L, Ye C, et al. Electrochemical synthesis of perovskite $LaFeO_3$ nanoparticle-modified TiO_2 nanotube arrays for enhanced visible-light photocatalytic activity. New J Chem 2019;43:16506–14. https://doi.org/10.1039/C9NJ03908B.

[12] Sandeep, Rai DP, Shankar A, Ghimire MP, Khenata R, Thapa RK. Study of electronic and magnetic properties in 4*f* electron based cubic $EuAlO_3$: a first-principles calculation. Phys Scr 2015;90:065803. https://doi.org/10.1088/0031-8949/90/6/065803.

[13] Derras M, Hamdad N, Derras M, Gessoum A. New theoretical model on the electronic structure and magnetic properties of the $YMnO_3$ perovskite oxide: Implementation of the U-Hubbard Hamiltonian. Results in Physics 2013;3:219–30. https://doi.org/10.1016/j.rinp.2013.09.011.

[14] Sabir B, Murtaza G, Arif Khalil RM, Mahmood Q. First principle study of electronic, mechanical, optical and thermoelectric properties of $CsMO_3$ (M = Ta, Nb) compounds for optoelectronic devices. Journal of Molecular Graphics and Modelling 2019;86:19–26. https://doi.org/10.1016/j.jmgm.2018.09.011.

[15] Khenata R, Sahnoun M, Baltache H, Rérat M, Rashek AH, Illes N, et al. First-principle calculations of structural, electronic and optical properties of $BaTiO_3$ and $BaZrO_3$ under hydrostatic pressure. Solid State Communications 2005;136:120–25. https://doi.org/10.1016/j.ssc.2005.04.004.

[16] Ali Z, Khan I, Ahmad I, Khan MS, Asadabadi SJ. Theoretical studies of the paramagnetic perovskites $MTaO_3$ (M = Ca, Sr and Ba). Materials Chemistry and Physics 2015;162:308–15. https://doi.org/10.1016/j.matchemphys.2015.05.072.

[17] Berri S, Bouarissa N. First-principle calculations to investigate structural, electronic, optical, thermodynamic, and thermoelectric properties of ABO_3 (A = Cs, Rb and B= Ta, Nb) compounds. Emergent Mater 2022;5:1831–47. https://doi.org/10.1007/s42247-021-00324-0.

[18] Xu Y-Q, Wu S-Y, Zhang L-J, Wu L-N, Ding C-C. First-principles study of structural, electronic, elastic, and optical properties of cubic $KNbO_3$ and $KTaO_3$ crystals. Physica Status Solidi (b) 2017;254:1600620. https://doi.org/10.1002/pssb.201600620.

[19] Ohno T, Akiyoshi M, Umebayashi T, Asai K, Mitsui T, Matsumura M. Preparation of S-doped TiO_2 photocatalysts and their photocatalytic activities under visible light. Applied Catalysis A: General 2004;115–21. https://doi.org/10.1016/j.apcata.2004.01.007.

[20] Mouhib B, Dahbi S, Douayar A, Tahiri N, El Bounagui O, Ez-Zahraouy H. Theoretical investigations of electronic structure and optical properties of S, Se or Te doped perovskite $ATiO_3$ (A=Ca, Ba, and Sr) materials for eco-friendly solar cells. Micro and Nanostructures 2022;163:107124. https://doi.org/10.1016/j.spmi.2021.107124.

[21] Shockley W, Queisser HJ. Detailed Balance Limit of Efficiency of *p-n* Junction Solar Cells. Journal of Applied Physics 1961;32:510–19. https://doi.org/10.1063/1.1736034.

[22] Blaha P, Schwarz K, Madsen G, Kvasnicka D, Luitz J. WIEN2k: An Augmented Plane Wave plus Local Orbitals Program for Calculating Crystal Properties. Technische Universität Wien, Wien 2001;28.

[23] Hohenberg P, Kohn W. Inhomogeneous Electron Gas. Phys Rev 1964;136:B864–71. https://doi.org/10.1103/PhysRev.136.B864.

Chapter 2: LITERATURE REVIEW

2.1 General

The investigation of S-substituted or doped perovskite materials to modulate larger band gaps has emerged as a burgeoning area of study within advanced materials science. Perovskite materials, characterized by their distinctive electronic and optical properties, have captured significant attention and hold great promise for diverse applications in optoelectronics. Among these applications, perovskite materials are being explored for their potential in solar cells, light-emitting diodes, and photodetectors. Introducing sulfur substitution or doping within perovskite structures offers an enticing avenue to engineer and fine-tune their band gaps. Such endeavors aim to reduce band gaps and enhance these materials' stability and overall performance characteristics. This literature review aims to comprehensively summarize key findings, challenges, and prospects in the dynamic S-substituted or doped perovskite materials field.

2.2 Historical Background

Perovskite compounds have garnered considerable interest in recent times owing to their outstanding properties and wide-ranging applications. This literature review briefly overviews the latest progress and significant discoveries in perovskite materials. Within the realm of photovoltaics, hybrid organic-inorganic perovskite solar cells have arisen as a disruptive technology, showcasing impressive power conversion efficiencies surpassing 25.7% [1]. Their notable attributes, such as high absorption coefficients, adjustable bandgaps, and straightforward fabrication processes, position perovskite solar cells as promising contenders for efficient conversion of solar energy at a low cost [2,3]. Ongoing research endeavors primarily concentrate on enhancing device stability and scalability and elucidating degradation mechanisms to expedite their commercial adoption.

Furthermore, perovskite compounds have transcended their utility in photovoltaics and found applications in other domains. In light-emitting diodes (LEDs), perovskite-based emitters exhibit remarkable color purity, customizable emission wavelengths, and exceptional brightness, rivaling traditional semiconductor materials. This has prompted extensive investigations into perovskite LEDs for applications in displays, lighting, and various optoelectronic fields [4,5]. Table 2.1 provides an overview of some previously explored perovskite compounds and their corresponding methodologies.

Table 2.1: Some previously studied Perovskite compounds, along with their band gaps.

Compounds	**Methodology**	**Band Gap E_g (eV)**	**Reference**
$CsSnCl_3$	Experimentally	2.9	[6]
$CsSnBr_3$	Experimentally	1.3	[7]
$CsSnI_3$	Experimentally	1.8	[8]
$SrNbO_3$	Experimentally	1.9	[9]
$MAPbI_3$	Experimentally	1.5	[10]
$MAPbBr_3$	Experimentally	2.39	[11]
$CsPbCl_3$	DFT	2.82	[12]
$FASnI_3$	Experimentally	1.27	[13]

The table shows that certain compounds exhibit wide band gaps, while others display band gaps within the visible range. This diversity in band gaps suggests that perovskite compounds are well-suited for various optoelectronics applications.

A literature review on S-substituted or doped perovskite materials for tuning larger band gaps reveals a growing body of research in advanced materials science. Perovskite materials have captured significant attention owing to their distinct electronic and optical characteristics, positioning them as promising contenders for a range of optoelectronic uses such as solar cells, photodetectors and light-emitting diodes. The introduction of sulfur substitution or doping in perovskite structures provides an encouraging pathway to tailor the band gap, improve stability, and enhance the performance of these materials. This review summarizes key findings, challenges, and prospects in this area [14–16].

The effect of chalcogen (S, Se, Te) doping in $ATiO_3$ (A =Ba, Ca, Sr) perovskites utilizing Density Functional Theory. It reveals that up to 7.5% of chalcogen doping results in reduced bandgap widths, preserving p-type semiconductor behavior. This is particularly notable in $BaTiO_3$ incorporating 2.5% and 5% Te doping, making it a more attractive option for photovoltaic applications than $SrTiO_3Te$ and $CaTiO_3Te$ [17]. The differences between sulfide perovskite $BaZrS_3$ and its oxide counterpart $BaZrO_3$. It notes that $BaZrS_3$ possesses a lower band gap, and neither material exhibits ferroelectric behavior at absolute zero. The study also investigates the role of atomic characteristics in influencing band gaps and dielectric responses [18]. Researchers synthesize sulfur-doped titanium dioxide (TiO_2) through the annealing process of titanium disulfide (TiS_2). This process shifts the TiO_2 absorption edge to lower energy regions. Theoretical analyses suggest that this shift is due to the interaction of S 3p states with the valence band, which offers opportunities for fine-tuning electronic properties in TiO_2 [19]. Density Functional Theory to assess the impact of sulfur doping in α-Fe_2O_3. It reveals that increased sulfur concentration progressively decreases the band gap, enhancing optical absorption within the visible spectrum. Notably, at around 5.6% sulfur concentration, the material exhibits an optimal direct band gap of around 1.45 eV, exhibiting strong optical absorption and improved carrier properties, establishing α-$Fe_2O_{3-x}S_x$ as a prospective and cost-effective material for solar cell applications [20].

Table 2.2: Effect of Sulfur substitution on previously studied Perovskite compounds.

Compounds	**Methodology**	**Band Gap, E_g (eV)**	**Sulfur substituted or doped E_g (eV)**	**Reference**
$BaZrO_3$	DFT	3.9	1.7	[18]
$ZnTaO_3$	Experimentally	3.1	2.6	[21]
$CaTiO_3$	DFT	3.2	1.8	[17]
$BaTiO_3$	DFT	2.9	1.2	[17,22]
$LiNbO_3$	DFT	4.2	2.8	[23]
$NaTaO_3$	Experimentally	4.0	2.5	[24]
$SrTiO_3$	DFT	3.5	1.4	[25,26]

The data in Table 2.2 demonstrates that the sulfur substitution significantly reduces the band gap of various perovskite materials. Specifically, when sulfur is introduced, the band gap of $BaZrO_3$ decreases from 3.90 eV to 1.7 eV, while $ZnTaO_3$ exhibits a reduction from 3.1 eV to 2.65 eV [21]. Similarly, for $CaTiO_3$, the band gap decreases from 3.2 eV to 1.8 eV [17], and $BaTiO_3$ experiences a band gap reduction from 2.9 eV to 1.2 eV [17,22]. A significant reduction in band gaps upon introducing sulfur substitution in $LiNbO_3$, $NaTaO_3$, and $SrTiO_3$ is also reported, where the band gap values was found to be decreased from 2.9 eV to 1.2 eV, 4.2 eV to 2.8 eV, and 4.0 eV to 2.5 eV, respectively [23, 24].

These findings highlight a consistent trend across different perovskite materials, where sulfur substitution lowers the band gap. This observation is supported theoretically and experimentally, underscoring the efficacy of sulfur incorporation as a method for modifying the band gap in these materials. Such reductions in band gap hold significant implications for potential applications in electronic devices, photovoltaics, and optoelectronics, offering enhanced tunability and performance in these systems.

Previous studies have consistently reported our selected materials as possessing wide band gaps in the case of our selected compounds, namely $RbTaO_3$, $KTaO_3$, and $CsTaO_3$. We summarized the previously calculated data to further advance our understanding of these compounds and explored new, uncharted information.

Table 2.3: Summary of the previous studies on $ATaO_{3-x}S_x$ compounds.

Compound	Structural	Mechanical	Optical	Electronic	Thermal	Ref.
$KTaO_3$	Yes	Yes	Yes	Yes	Yes	[27,28]
$RbTaO_3$	Yes	Yes	Yes	Yes	Yes	[29,30]
$CsTaO_3$	Yes	Yes	Yes	Yes	Yes	[30,31]
$KTaO_2S$	No	No	No	No	No	
$RbTaO_2S$	No	No	No	No	No	
$CsTaO_2S$	No	No	No	No	No	
$KTaOS_2$	No	No	No	No	No	
$RbTaOS_2$	No	No	No	No	No	
$CsTaOS_2$	No	No	No	No	No	
$KTaS_3$	No	No	No	No	No	
$RbTaS_3$	No	No	No	No	No	
$CsTaS_3$	No	No	No	No	No	

The following data presents earlier findings on the absorption coefficient and optical reflectivity of various oxide perovskite compounds. Previous studies, including analyses of absorption coefficient and optical reflectivity, have demonstrated a compelling property of oxide perovskite compounds: their remarkable ability to strongly absorb light in the visible spectrum while reflecting minimal amounts—these unique characteristics position oxide perovskites as prolific candidates for application as absorber materials in solar cells.

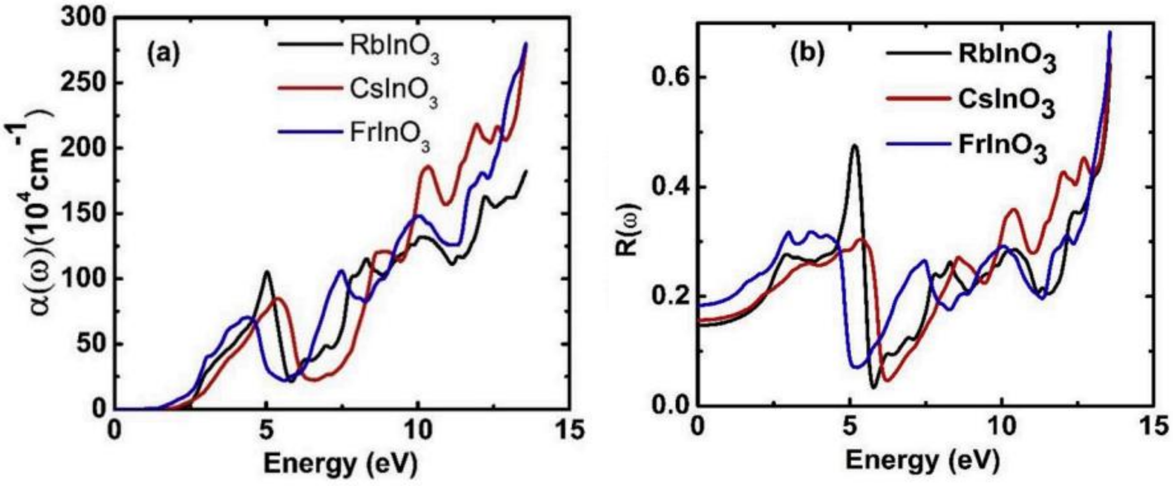

Fig 2.1 : Absorption Coefficient and Reflectivity of $YInO_3$ (Y = Rb, Cs, Fr) [32]

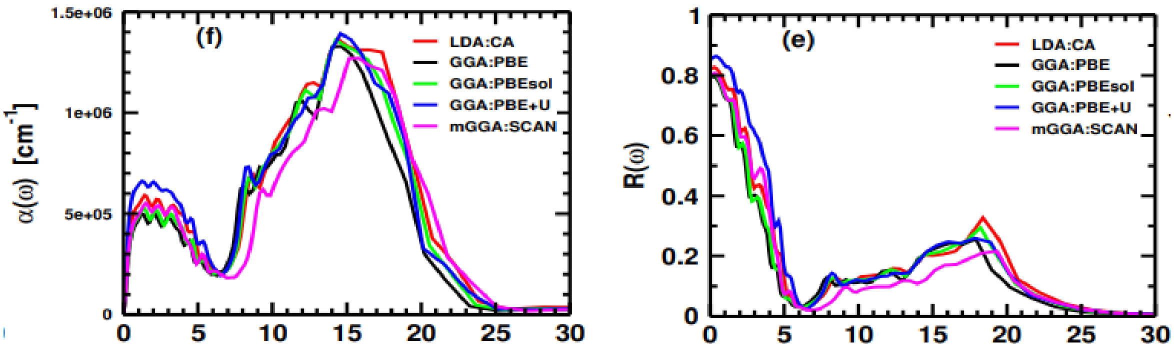

Fig 2.2: Absorption Coefficient and Reflectivity of $MgZnO_3$[33]

Previous studies, including analyses of absorption coefficient and optical reflectivity, have demonstrated a compelling property of oxide perovskite compounds: their remarkable ability to strongly absorb light in the visible spectrum while reflecting minimal amounts—these unique characteristics position oxide perovskites as prolific candidates for application as absorber materials in solar cells. The exceptional light absorption potential, coupled with potential advantages like tunable bandgaps and high carrier mobilities, has spurred our investigation of $KTaO_3$ as a particularly promising candidate within the perovskite family.

2.3 Summary and Implications

Summary:

The literature review discusses the burgeoning field of S-substituted or doped perovskite materials, aiming to modulate larger band gaps. Perovskite materials have garnered considerable interest owing to their distinct electronic and optical characteristics, positioning them as promising candidates for optoelectronic applications like solar cells, LEDs, and photodetectors. Introducing sulfur substitution or doping within perovskite structures offers a promising avenue to engineer their band gaps, enhance stability, and improve overall performance characteristics. The review highlights key findings, challenges, and prospects in this area.

Additionally, the chapter presents various studies on the effect of sulfur substitution on perovskite compounds, theoretically and experimentally. It reveals a consistent trend across different materials, where sulfur substitution reduces band gap width. This reduction holds significant implications for potential applications in electronic devices, photovoltaics, and optoelectronics, offering enhanced tunability and performance in these systems.

Implications:

1. **Band Gap Engineering:** The ability to modulate band gaps through sulfur substitution opens up new possibilities for tailoring perovskite materials to suit specific applications, such as optimizing their performance in solar cells and LEDs.

2. **Enhanced Performance:** By reducing band gaps, sulfur substitution improves the absorption characteristics of perovskite materials, potentially leading to higher efficiencies in optoelectronic devices.
3. **Stability Improvement:** Incorporating sulfur may also enhance perovskite materials' stability, addressing one of the key challenges in their commercial adoption.
4. **Cost-Effectiveness:** Some sulfur-doped materials, such as α-Fe2O$_{3-x}$S$_{x}$, exhibit promising properties for solar cell applications and offering a cost-effective alternative to traditional semiconductor materials.
5. **Diverse Applications:** The wide range of perovskite compounds explored in the literature review underscores their versatility for various optoelectronic applications beyond photovoltaics, including LEDs and photodetectors.

References

[1] Green MA, Dunlop ED, Siefer G, Yoshita M, Kopidakis N, Bothe K, et al. Solar cell efficiency tables (Version 61). Progress in Photovoltaics: Research and Applications 2023;31:3–16. https://doi.org/10.1002/pip.3646.

[2] L. Unger E, Kegelmann L, Suchan K, Sörell D, Korte L, Albrecht S. Roadmap and roadblocks for the band gap tunability of metal halide perovskites. Journal of Materials Chemistry A 2017;5:15983–15983. https://doi.org/10.1039/C7TA90141K.

[3] Stranks SD, Eperon GE, Grancini G, Menelaou C, Alcocer MJP, Leijtens T, et al. Electron-Hole Diffusion Lengths Exceeding 1 Micrometer in an Organometal Trihalide Perovskite Absorber. Science 2013;342:341–4. https://doi.org/10.1126/science.1243982.

[4] Chenna P, Gandi S, Pookatt S, Parne SR. Perovskite white light emitting diodes: A review. Materials Today Electronics 2023. https://doi.org/10.1016/j.mtelec.2023.100057.

[5] Dong H, Ran C, Gao W, Li M, Xia Y, Huang W. Metal Halide Perovskite for next-generation optoelectronics: progresses and prospects. eLight 2023;3:3. https://doi.org/10.1186/s43593-022-00033-z.

[6] Voloshinovskii AS, Myagkota SV, Pidzyrailo NS, Tokarivskii MV. Luminescence and structural transformations of $CsSnCl_3$ crystals. J Appl Spectrosc 1994;60:226–8. https://doi.org/10.1007/BF02606360.

[7] Clark SJ, Flint CD, Donaldson JD. Luminescence and electrical conductivity of $CsSnBr_3$, and related phases. Journal of Physics and Chemistry of Solids 1981;42:133–5. https://doi.org/10.1016/0022-3697(81)90072-X.

[8] Synthesis and characterization of $CsSnI_3$ thin films | Applied Physics Letters | AIP Publishing.https://pubs.aip.org/aip/apl/article-

abstract/96/22/221903/338960/Synthesis-and-characterization-of-CsSnI3-thin? (accessed February 16, 2024).

[9] Xu X, Randorn C, Efstathiou P, Irvine JTS. A red metallic oxide photocatalyst. Nature Mater 2012;11:595–8. https://doi.org/10.1038/nmat3312.

[10] Qaid SMH, Al Sobaie MohammedS, Majeed Khan MA, Bedja IM, Alharbi FahhadH, Nazeeruddin MK, et al. Band-gap tuning of lead halide perovskite using a single step spin-coating deposition process. Materials Letters 2016;164:498–501. https://doi.org/10.1016/j.matlet.2015.10.135.

[11] Ulatowski AM, Wright AD, Wenger B, Buizza LRV, Motti SG, Eggimann HJ, et al. Charge-Carrier Trapping Dynamics in Bismuth-Doped Thin Films of $MAPbBr_3$ Perovskite.J Phys Chem Lett 2020;11:3681–8. https://doi.org/10.1021/acs.jpclett.0c01048.

[12] Protesescu L, Yakunin S, Bodnarchuk MI, Krieg F, Caputo R, Hendon CH, et al. Nanocrystals of Cesium Lead Halide Perovskites ($CsPbX_3$, X = Cl, Br, and I): Novel Optoelectronic Materials Showing Bright Emission with Wide Color Gamut. Nano Lett 2015;15:3692–6. https://doi.org/10.1021/nl5048779.

[13] Role of Polar Phonons in the Photo Excited State of Metal Halide Perovskites | Scientific Reports n.d. https://www.nature.com/articles/srep28618 (accessed February 16, 2024).

[14] Abd Mutalib M, Ahmad Ludin N, Su'ait MS, Davies M, Sepeai S, Mat Teridi MA, et al. Performance-Enhancing Sulfur-Doped TiO_2 Photoanodes for Perovskite Solar Cells. Applied Sciences 2022;12:429. https://doi.org/10.3390/app12010429.

[15] Alam MdS, Saiduzzaman M, Biswas A, Ahmed T, Sultana A, Hossain KM. Tuning band gap and enhancing optical functions of $AGeF_3$ (A = K, Rb) under pressure for

improved optoelectronic applications. Sci Rep 2022;12. https://doi.org/10.1038/s41598-022-12713-14.

[16] Zuhair Abbas Shah S, Niaz S, Nasir T, Sifuna J. First principles insight into band gap tuning in bismuth based double perovskites $X_2NaBiCl_6$ (X = Cs, Rb, K) for enhanced optoelectronic and thermoelectric properties. Results in Chemistry 2023;5:100828. https://doi.org/10.1016/j.rechem.2023.100828.

[17] Mouhib B, Dahbi S, Douayar A, Tahiri N, El Bounagui O, Ez-Zahraouy H. Theoretical investigations of electronic structure and optical properties of S, Se or Te doped perovskite $ATiO_3$ (A=Ca, Ba, and Sr) materials for eco-friendly solar cells. Micro and Nanostructures 2022;163:107124. https://doi.org/10.1016/j.spmi.2021.107124.

[18] Bennett JW, Grinberg I, Rappe AM. Effect of substituting of S for O: The sulfide perovskite $BaZrS_3$ investigated with density functional theory. Phys Rev B 2009;79:235115. https://doi.org/10.1103/PhysRevB.79.235115.

[19] Umebayashi T, Yamaki T, Itoh H, Asai K. Band gap narrowing of titanium dioxide by sulfur doping. Applied Physics Letters 2002;81. https://doi.org/10.1063/1.1493647.

[20] Xia C, Jia Y, Tao M, Zhang Q. Tuning the band gap of hematite α-Fe_2O_3 by sulfur doping. Physics Letters A 2013;377. https://doi.org/10.1016/j.physleta.2013.05.026.

[21] Tavakoli-Azar T, Mahjoub AR, Sadjadi MS, Farhadyar N, Sadr MH. Improving the photocatalytic performance of a perovskite $ZnTiO_3$ through $ZnTiO_3S$ nanocomposites for degradation of Crystal violet and Rhodamine B pollutants under sunlight.Inorganic Chemistry Communications 2020. https://doi.org/10.1016/j.inoche.2020.108091.

[22] Hwang J, Kolodiazhnyi T, Yang J, Couillard M. Doping and temperature-dependent optical properties of oxygen-reduced $BaTiO_3$. Phys Rev B 2010;82:214109. https://doi.org/10.1103/PhysRevB.82.214109.

[23] Ait Brahim I, Bekkioui N, Tahiri M, Ez-Zahraouy H. Doping effect of chalcogens on electronic and optical properties of perovskite $LiNbO_3$ compound: Ab initio calculations. Chemical Physics 2021. https://doi.org/10.1016/j.chemphys.2021.111320.

[24] Li F-F, Liu D-R, Gao G-M, Xue B, Jiang Y-S. Improved visible-light photocatalytic activity of $NaTaO_3$ with perovskite-like structure via sulfur anion doping. Applied Catalysis B: Environmental 2015;166–167. https://doi.org/10.1016/j.apcatb.2014.10.049.

[25] Zhang C, Jia Y, Jing Y, Yao Y, Ma J, Sun J. Effect of non-metal elements (B, C, N, F, P, S) mono-doping as anions on electronic structure of $SrTiO_3$. Computational Materials Science 2013;79:69–74. https://doi.org/10.1016/j.commatsci.2013.06.009.

[26] Crandles DA, Nicholas B, Dreher C, Homes CC, McConnell AW, Clayman BP, et al. Optical properties of highly reduced $SrTiO_{3-x}$. Phys Rev B 1999;59:12842–6. https://doi.org/10.1103/PhysRevB.59.12842.

[27] Bouafia H, Hiadsi S, Abidri B, Akriche A, Ghalouci L, Sahli B. Structural, elastic, electronic and thermodynamic properties of $KTaO_3$ and $NaTaO_3$: Ab initio investigations. Computational Materials Science 2013;75:1–8. https://doi.org/10.1016/j.commatsci.2013.03.030.

[28] Liu X, Lv W, Chen C, Yang W, Han J, Lin J, et al. Structural, electronic and optical properties of $KTaO_3$ under high pressure based on first-principles. Materials Science in Semiconductor Processing 2022;138:106248. https://doi.org/10.1016/j.mssp.2021.106248.

[29] Sarwan M, Shukla P, Singh S. Structural stability, electronic and elastic properties of cubic $RbTaO_3$ perovskite oxide. AIP Conference Proceedings 2020;2265:030341. https://doi.org/10.1063/5.0017058.

[30] Berri S, Bouarissa N. First-principle calculations to investigate structural, electronic, optical, thermodynamic, and thermoelectric properties of ABO_3 (A = Cs, Rb and B = Ta, Nb) compounds. Emergent Mater 2022. https://doi.org/10.1007/s42247-021-00324-0.

[31] Sabir B, Murtaza G, Arif Khalil RM, Mahmood Q. First principle study of electronic, mechanical, optical and thermoelectric properties of $CsMO_3$ (M = Ta, Nb) compounds for optoelectronic devices. Journal of Molecular Graphics and Modelling 2019;86:19–26. https://doi.org/10.1016/j.jmgm.2018.09.011.

[32] Hussain MI, Khalil RMA, Hussain F, Imran M, Rana AM, Kim S. Investigations of structural, electronic and optical properties of $YInO_3$ (Y = Rb, Cs, Fr) perovskite oxides using mBJ approximation for optoelectronic applications: A first principles study. Materials Science in Semiconductor Processing 2020;113:105064. https://doi.org/10.1016/j.mssp.2020.105064.

[33] Lawati DR, Neupane HK, Chaudhary DK, Shrestha P, Adhikari RP, Joshi LP, et al. Structural, mechanical, electronic and optical properties of $MgZnO_3$ perovskite: First-principles study. Journal of Physics and Chemistry of Solids 2023;181:111547. https://doi.org/10.1016/j.jpcs.2023.111547.

Chapter 3: THEORETICAL METHODOLOGY

3.1 Introduction

The present investigation employs a rigorous methodology to validate the first-principles calculations for oxide perovskites, specifically $ATaO_{3-x}S_x$ [A = Rb, K, Cs], by utilizing the full-potential linear augmented plane wave (FP-LAPW) method, a robust approach founded on the principles of density functional theory (DFT) [1,2]. These calculations are executed using the widely recognized WIEN2k code [3], a dependable tool for computational materials science. The primary objectives of this methodology encompass the optimization of crystal structures, the computation of mechanical properties, and the determination of electronic and optical properties. The Generalized Gradient Approximation by Perdew-Burke-Ernzerhof (GGA-PBE) [4,5] is employed for crystal structure optimization to achieve these objectives. At the same time, the modified Becke-Johnson approach (TB-mBJ) [6] is used for electronic and optical property calculations. These computational tools provide a solid foundation for our research, ensuring reliable and accurate results. In the pursuit of precision, our methodology employs a substantial 10 × 10 × 10 mesh (1000 K-points) covering the primary Brillouin zone of reciprocal space. Stability is a critical consideration in our study, and to achieve this, we utilize FP-LAPW basis functions extended to RMT × Kmax = 6, RMT denotes the minimal radius of the muffin-tin spheres, while Kmax indicates the maximum magnitude of the k-vector in the expansions of plane wave. An energy convergence threshold of 10^{-5} Ry is set, and the charge density is Fourier extended to Gmax = 12. This level of detail ensures that our calculations are robust and trustworthy. Furthermore, we assess the density of states employing the tetrahedron method, a technique renowned for its precision in determining the electronic structure of materials. Various parameters are computed using the IRelast package [7] to evaluate the elastic properties, enhancing our understanding of the mechanical characteristics of the oxide perovskites under investigation. We determined the structural parameters by analyzing the relationship between energy and volume, fitting the data with the Burch-Murnaghan equation of state [8]. To investigate the crystal's vibrational characteristics, we calculated its phonon spectra using the finite displacement method within the PHONOPY code [9]. We utilized density functional perturbation theory within this code to derive phonon frequencies and force constant matrices [10]. We determine the force constants for the cubic phase by employing a supercell sized (2 × 2 × 2). Within the tetragonal phase, our calculations involve both (1 × 1 × 1) and (2 × 2 × 2) supercells, involving atomic shifts of 0.01 Å along the lattice vectors throughout the computations. These phonon dispersion curves are instrumental in elucidating the vibrational properties and stability of the materials, adding to a thorough comprehension of their behavior. This chapter presents a brief description of the theories and tools used in this study.

3.2 WIEN2k code

The WIEN2k code, initially crafted by Karlheinz Schwarz and Peter Blaha, is a powerful tool for computations of electronic structure utilizing density functional theory. It employs the FP-LAPW (Full Potential Linearized Augmented Plane-Wave) method extensively [11]. It is renowned for its ability to handle various levels of theory, including LDA, meta-GGA, GGA, hybrid-DFT and LDA+U. Notably, it's an all-electron scheme capturing relativistic effects. When interfaced with Phonopy, WIEN2k extends its capabilities to perform phonon dispersion calculations [3]. It is coded in FORTRAN90 and offers Fine-grained parallelism implemented to efficiency on clusters or multi-core machines. The W2web interface on the web also facilitates input generation and material modeling. Within WIEN2k, the self-consistent field (SCF) cycle can be run either with or without concurrent atomic position optimization.

3.3 PHONOPY

PHONOPY, developed by Atsushi Togo, is accessible as open-source tool for extending phonon at the gamma point calculations from first-principles software to complete phonon dispersion relations curves throughout Brillouin Zone (BZ) [12]. It operates within a supercell, and the precision of the phonon dispersion improves with a larger dimensions of the supercell. PHONOPY is compatible with ab initio tools like WIEN2K and VASP for force calculations. It supports both quasi-harmonic and harmonic approximations. Forces on atoms are used to create interatomic force constants (IFC) or force constants (FC) through methods like density functional perturbation theory. These constants are then used to calculate phonon frequencies via a dynamical matrix. VASP involves finite difference or DFPT methods to compute gamma-point phonon frequencies and interpolate them across high-symmetry k-points in the BZ to obtain complete phonon dispersion.

3.4 The Full Potential APW methods

A significant transition has occurred in the realm of electronic structure computations for crystalline materials. This journey has advanced from Slater's Augmented Plane Wave (APW) approach to the Linearized Augmented Plane Wave (LAPW) approach, and it has further evolved with the introduction of the innovative APW+lo technique, elucidated by Schwarz et al. in 2001 [3].

3.5 The LAPW method

The Linearized Augmented Plane-Wave method (LAPW) is a realization of the Kohn-Sham Density Functional Theory (DFT) tailored for periodic materials [13,14]. LAPW treats valence and core electrons equally within the framework of DFT and does not employ shape approximations, encompassing charge density and the complete potential. This comprehensive approach is often termed the FLAPW (Full-Potential Linearized Augmented Plane-Wave) method, which accounts for all-electron interactions [15]. It distinguishes itself by not relying on pseudopotential approximations and utilizes a systematically expandable basis set. These characteristics establish LAPW as one of the most precise DFT implementations, applicable to all crystalline materials, regardless of their chemical composition.

3.6 Schrödinger equation

The Schrödinger equation, formulated by Erwin Schrödinger in 1926, is a fundamental concept in quantum mechanics, describing how the quantum states of a physical system evolve. It is often called a wave function or state vector and plays a crucial role in physics and mathematics. In mathematical terms, Schrödinger's equation and its variations find widespread applications in partial differential equations, including geometry, spectral theory, integral systems, and scattering theory [16].

There are two primary forms of the Schrödinger equation: the Schrödinger equation with time-dependent, which describes the progression of the system over time, and the time-independent Schrödinger equation, which is suitable for systems in a stationary state.

In a general quantum system, the Schrödinger equation accounting for time evolution is represented as:

$$\Psi(x,t) = -i\hbar\,\partial\,\Psi\frac{(x,t)}{\partial t} \tag{1}$$

Here, ħ denotes the reduced Planck constant, $\Psi(x,t)$ is the wave function, and $\partial\,\Psi\frac{(x,t)}{\partial t}$ represents the time derivative of the wave function.

When considering a solitary particle within a potential, the time-independent Schrödinger equation manifests in the following manner:

$$\left[\left(-\frac{\hbar^2}{2m}\right)\nabla^2 + V(x)\right]\Psi(x) = E\,\Psi(x) \qquad (2)$$

Where, the symbol m refers to the mass of the particle, V(x) signifies the time-independent potential energy, ∇^2 represents the Laplacian operator and E denotes the energy of the particle.

Depending on the physical context, one can solve the Schrödinger equation in various dimensions, such as three-dimensional, two-dimensional or one-dimensional systems. In each case, the equation describes the quantum behavior of particles and provides solutions that help understand their energy levels and behavior. In summary, the Schrödinger equation is a foundational concept in quantum mechanics that describes the behavior of physical systems and is essential for understanding the quantum states of particles in various dimensions.

3.7 The Density Functional Theory

In the 1960s, Density Functional Theory (DFT) emerged as an alternative to the computationally intensive Hartree-Fock method. DFT is a approach for determining the properties of many-electron systems by utilizing functionals that depend on the spatial distribution of electron density instead of wavefunctions. Its roots originates from the 1927 Thomas-Fermi model, which proposed an approximately even distribution of electrons within an atom [17,18]. Yet, this model suffered from inaccuracies due to overlooked electron correlation and exchange energy. Density Functional Theory's groundwork was reinforced by the 1964 publication of the Hohenberg-Kohn theorems, providing a more rigorous theoretical framework [2].

3.7.1 The Hohenberg–Kohn Theorems

During the 1960s, the development of Density Functional Theory (DFT) offered a method to compute a system's total energy while considering exchange and correlation effects. This groundbreaking work was attributed to Pierre Hohenberg and Walter Kohn [2], who established in 1964 that the electronic energy in the ground state was exclusively determined by the electronic density, denoted as $\varrho(r)$. This development led to the formulation of two pivotal theorems:

Theorem 1: The total energy E_{total} and the external potential $V_{ext}(r)$, are both functional expressions of the electron density $\varrho(r)$.

Theorem 2: The lowest energy state of the system is achieved only when the electron density is in its ground state configuration. In simpler terms, any other energy associated with a random electron density is higher than the energy corresponding to the ground-state density:

$$E_{GS}[\rho(r)] \geq E_{GS}\left[\rho_{GS}(r)\right] \tag{3}$$

Here, the "GS" represents the ground state. In contrast, $[\rho(r)]$ represents the system's energy calculated with a random electron density, while $E_{GS}[\rho_{GS}(r)]$ is the minimum energy attainable with the ground-state electron density. To streamline subsequent expressions, we omit the "GS" subscript. As a result, the energy function, under the Born-Oppenheimer approximation, can be formulated as:

$$E[\rho(r)] = T[\rho(r)] + V_{ee}[\rho(r)] + V_{en}[\rho(r)] \tag{4}$$

In this equation, $[\rho(r)]$, $V_{ee}[\rho(r)]$ and $V_{en}[\rho(r)]$ represent the kinetic energy, electron-electron interaction energy, and electron-nuclear interaction energy, respectively. When we isolating the energy originating from the interaction between electrons and the external potential, the total power can be expressed as a function of the electron density: $E[\rho(r)] = F_{HK}[\rho(r)] + \int \rho(r)V_{ext}(r)dr$ (5)

3.7.2 The Kohn-Sham Equations

The Hohenberg-Kohn Theorems state that finding the total energy starts with identifying the density in the lowest energy state of the system. Yet, the exact link between energy and density remains unknown. In 1965, Kohn and Sham [19] devised a technique relying on the one-electron Schrödinger equation. This method helps ascertain the density (ϱ) using equations considering correlation and exchange effects. Their key equation simplifies the complex wave function of many electrons into a solitary Slater determinant made up of one-electron wavefunctions.

$$\left(-\frac{\hbar^2}{2m}\nabla^2 + \upsilon_{eff}(r)\right)\varphi_i(r) = \varepsilon_i\varphi_i(r) \tag{6}$$

In this equation, $\upsilon_{eff}(r)$ is referred to as the Kohn-Sham potential, embodying the effective external potential governing the motion of non-interacting particles. $\varphi_i(r)$ denotes the Kohn-Sham orbital function, the Kohn-Sham orbital function, with ε_i representing the eigenvalue associated with the respective Kohn–Sham orbital, indicative of its energy. The electron density calculation is expressed by the following equation:

$$\rho(r) = \sum_{i=1}^{N}|\varphi_i(r)| \tag{7}$$

Here, N represents the quantity of electrons within the system. The expression for $\upsilon_{eff}(r)$ can be presented as:

$$\upsilon_{eff}(r) = E_{ff}(r) + e^2\int\frac{\rho(r')}{|r-r'|}dr' + V_{xc}(r) \tag{8}$$

The total energy, considering the Kohn-Sham external field, can be represented as follows:

$$E(\rho) = T(\rho) + E_{ee}(\rho) + \int \upsilon_{eff}(r)\rho(r)dr + V_{xc}(\rho) \tag{9}$$

In this context, $T(\rho)$ represents the kinetic energy of non-interacting electrons, $E_{ee}(\rho)$ signifies the interaction energy among electrons, $\upsilon_{eff}(r)$ is the external potential as specified earlier, and $V_{xc}(\rho)$ stands for the exchange-correlation potential, which can be expressed as:

$$V_{xc} = \frac{\delta E_{xc}(\rho)}{\delta\rho(r)} \tag{10}$$

$E_{xc}(\rho)$ consists of four terms: the Kinetic functional, the Coulomb functional, the Correlation functional and the Exchange functional. Since some components of DFT cannot be known precisely approximations are introduced. Therefore, a proper approximation of the $E_{xc}(\rho)$ term results in a method that is both efficient and accurate, such as the Generalized Gradient Approximation (GGA), the Local Density Approximation (LDA), both widely accepted in modern DFT research.

To solve Kohn-Sham equations iteratively for a many-body system, one must define the exchange-correlation and Hartree potentials, which depend on the electron density. Initially, a trial density is used, and after each iteration, the electron density is updated based on the resulting single-electron wave functions. This process continues until the electron density converges within a chosen criterion. The converged density serves as the ground state, enabling calculating the system's total energy.

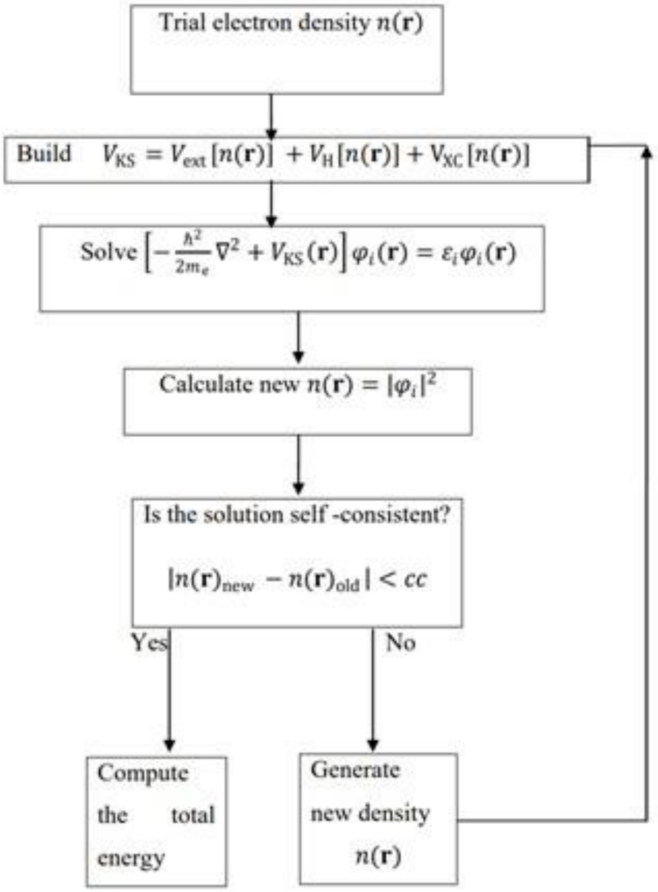

Figure 3.1: Illustration of how the self-consistent field (SCF) process works to solve Kohn-Sham equations using a chosen convergence criterion.

3.8 Approximations for the Exchange-Correlation Energy

The Hohenberg, Sham, and Kohn approach offer a precise option to the Schrödinger equation for determining the ground-state energy. However, the primary source of error in density functional theory (DFT) typically stems from the exchange-correlation function (EXC) approximations. This function can only be derived strictly for the homogeneous electron gas, where the electron density is constant $\rho(\vec{r}) = C$, a rare occurrence in real materials. Variations in electron density govern essential properties like chemical bonds. The search for suitable functionals is a significant endeavor in condensed matter physics, with four primary generations of correlation and exchange approximations: (i) gradient-corrected or generalized gradient approximation (GGA), (ii) hybrid functional, (iii) meta-GGA, and (iv) Local Density Approximation (LDA), which incorporate a segment of precise exchange from Hartree-Fock theory into the exchange-correlation term of DFT.

3.8.1 Generalized Gradient Approximation (GGA)

The Generalized Gradient Approximation (GGA) goes beyond density and considers density gradients to enhance the accuracy of ground-state energies and molecular geometries. This expression with spin is denoted as:

$$E_{XC}^{GGA}\big(\rho(r)\big) = \int \rho(r)\varepsilon_{XC}(\rho(r_{\uparrow}, r_{\downarrow}, \nabla r_{\uparrow}, \nabla r_{\downarrow}))dr \tag{11}$$

As theoretical advancements have progressed, various GGA functions like PBE [5] and PW91[20] have been developed to reduce errors. While GGA mitigates underestimations, it still has shortcomings, such as overestimating lattice constants for heavy elements and underestimating band gaps. Striking a balance between computational efficiency and accuracy, the Perdew-Burke-Ernzerhof (PBE) approach incorporating GGA functionality is widely regarded as the most appropriate approach for electronic structure calculations in this context.

3.8.2 Hybrid Functionals

Becke introduced the hybrid methodology in 1993 [21], enriches Density Functional Theory (DFT) by incorporating an exchange component from Hartree-Fock theory into the exchange-correlation term. This hybridization with Hartree-Fock exchange offers a straightforward enhancement for calculating various feature in molecular scheme, including atomization energies, vibration frequencies, and bond lengths, which often need to be more adequately described by basic DFT functionals. Correlation functional and hybrid exchange and can be expressed as:

$$E_{XC}^{hybrid} = E_C^{DFT1} + \alpha E_X^{HF} + (1-\alpha)E_X^{DFT2} \tag{12}$$

Here, DFT1 and DFT2 may be functional from LDA or GGA schemes, and the parameter α weights the contribution of Hartree-Fock (HF) and DFT. Additional widely-used parameter-free hybrid functional encompass PBE_0 and Heyd-Scuseria-Ernzerhof (HSE) [22]. These functionals differ in their selection of the exchange-correlation DFT functional term and mixing parameter α.

3.8.3 TB-mBJ

One significant challenge in KS-DFT is its failure to predict the band gaps of insulators and semiconductors precisely. Both LSDA and GGA fall short of providing an accurate portrayal of the band structure in systems with strong correlations. A new functional called the Tran-Blaha modified Becke-Johnson exchange potential (TB-mBJ) was introduced to address this issue. TB-mBJ has been successfully incorporated into the WIEN2k code, offering a solution to improve band gap predictions in these materials [23].

3.9 Volume Optimization in Wien2k: Unveiling Material Properties

Volume optimization in Wien2k is a crucial tool rooted in density functional theory (DFT) for manipulating a material's characteristics by adjusting its unit cell volume. This method allows researchers to systematically investigate the impact of volume changes on electronic structure, energy levels, and stability. The software can determine the equilibrium volume at which the material is most stable by computing the total energy across various volumes while keeping atomic positions constant. This information is essential for understanding phase transitions, structural stability, and electronic properties under varying conditions. The applications of volume optimization are diverse, spanning from understanding pressure-induced phase changes to enhancing material properties in fields like semiconductors and photovoltaics. Overall, volume optimization in Wien2k serves as a powerful approach to unveil the intricate relationship between unit cell volume and material behavior, driving progress in various scientific domains.

3.10 Mechanical Properties

Three essential accepted elastic stability criteria exist for cubic crystals [24].

$$C_{11}+2C_{12} > 0,\ C_{44} > 0,\ C_{11}-C_{12} > 0 \tag{13}$$

The six independent elastic constants acquired for the tetragonal crystal, namely C_{11}, C_{12}, C_{13}, C33, C_{44}, and C_{66}, validate the elastic stability criteria. The spinodal, shear, and born criteria are employed in conjunction with the bulk, shear, and tetragonal shear moduli, respectively. The following expressions represent them [25].

$$C_{11} - C_{12} > 0 \tag{14}$$

$$C_{11} + C_{33} - 2C_{13} > 0 \tag{15}$$

$$C_{11} > 0,\ C_{33} > 0 \tag{16}$$

$$C_{44} > 0,\ C_{66} > 0 \tag{17}$$

$$2C_{11} + C_{33} + 2C_{12} + 4C_{13} > 0 \tag{18}$$

$$\frac{1}{3}(C_{11} + 2C_{13}) < B < \frac{1}{3}(C_{11} + 2C_{33}) \tag{19}$$

In tetragonal crystals, the resistances to linear compression are measured by C_{11} and C_{33} along the x and z directions, respectively [26].

The bulk modulus and the shear modulus in Hill's average for cubic [27] and tetragonal [28] systems are given as,

$$B_V = \frac{1}{3}(C_{11} + 2C_{12}) \tag{20}$$

$$G_V = \frac{1}{5}[(C_{11} - C_{12}) + 3C_{44}] \tag{21}$$

And, $B_V = \frac{1}{9}(2C_{11} + C_{12} + C_{33} + 4C_{13})$ (22)

$$G_V = \frac{1}{30}(M + 3C_{11} - 3C_{12} + 12C_{44} + 6C_{66}) \tag{23}$$

The above quantities can be taken in the Reuss average [28,29],

$$B_R = \frac{1}{3} C_{11} + 2C_{12}) = B_V \tag{24}$$

$$G_R = [\frac{4}{5}(C_{11} - C_{12})^{-1} + \frac{3}{5} {C_{44}}^{-1}]^{-1} \tag{25}$$

and, $B_R = \frac{C^2}{\mathrm{M}}$ (26)

$$G_R = 15/[\frac{18\mathrm{B}_V}{C^2} + \frac{6}{C_{11} - C_{12}} + \frac{6}{C_{44}} + \frac{3}{C_{66}}] \tag{27}$$

Where, $M = C_{11}+C_{12}+2C_{33}-4C_{13}$ and $C^2 = (C_{11} + C_{12})C_{33} - 2C_{13}^2$.

Also, in Hill empirical average [30], the Bulk modulus and share modulus are expressed by,

$$B = \frac{1}{2}(B_V + B_R) \tag{28}$$

$$G = \frac{1}{2}(G_V + G_R) \tag{29}$$

respectively. The young modulus (Y) and Poisson's (ν) ratio for polycrystalline materials [31] are frequently calculated by using the following relationships:

$Y = \frac{9\mathrm{BG}}{3\mathrm{B+G}}$ and $\nu = \frac{3\mathrm{B-Y}}{6\mathrm{B}}$ (30)

3.10.1 Elastic Anisotropy

Various formalisms are available to evaluate the elastic anisotropy of crystals. For cubic crystals, the Zener anisotropy is utilized to quantify their anisotropic behavior [32].

$$A^U = \frac{2C_{44}}{(C_{11} - C_{12})} \tag{31}$$

For the tetragonal crystal, shear anisotropy factors $A_{\{100\}}$ and $A_{\{001\}}$ for the {100} and {001} planes, respectively, were calculated by the following equation:

$$A_{100} = \frac{4C_{44}}{(C_{11}+C_{33}-2C_{13})} \text{ and } A_{001} = \frac{2C_{66}}{(C_{11}-2C_{13})} \qquad (32)$$

The factors A_{100} and A_{001}, smaller or greater than unity, measure the degree of anisotropy, while the values equal to unity reveal completely isotropic properties.

By utilizing the relationship between the highest anisotropy (Voigt, V) and the lowest anisotropy (Reuss, R) of the bulk and shear modulus, one can compute the percentage anisotropy in compressibility (A_B), percentage shear anisotropy (A_G), and the universal anisotropy index A^U [33],

$$A^U = 5\frac{G_V}{G_R} + \frac{B_V}{B_R} - 6,\ A_B \frac{B_V-B_R}{B_V+B_R} \times 100\% \times 100\%, \text{ and } A_G = \frac{G_V-G_R}{G_V+G_R} \times 100\% \qquad (33)$$

3.11 Electronic Properties

3.11.1 Band Structure

In the field of solid-state physics, the electronic band structure of a material delineates the permissible and forbidden energy states for electrons. This phenomenon emerges from the scattering of electron waves governed by quantum mechanics within the periodic crystalline lattice. A band structure diagram encapsulates information about both intramolecular (within the molecule) and intermolecular (between molecules) interactions. Understanding this diagram provides crucial insights into a material's electronic conductivity, optical characteristics, and resistance to oxidation or reduction through doping. Consequently, comprehension of the structure of electronic bands facilitates the predictive understanding of critical solid-state properties. The structure of electronic bands hinges on the of individual atomic orbitals and the arrangement of the crystal lattice. It is the pivotal link between a material's crystal structure and physical characteristics. Within the Brillouin zone (BZ), each state is defined by a wave number (K), and these wave numbers densely populate the BZ in large crystals. Constructing a BZ around each lattice wave number results in a complete space-filling, with one zone for everyone. The Brillouin zone volume aligns with the primitive cell volume in the wave number lattice, equating the quantity of K points within the BZ with the primitive cells in the crystal. This equality between the states in the Brillouin zone and primitive cells is significant when considering electron occupation in crystal band states. Given a finite set of wave numbers defining states and an endless array of states, each wave number must correspond to an infinite set of states. When specifying a state, we define its wave number and position within the energy hierarchy. The state with the lowest energy at a specific wave number is termed the first band, with subsequent states at the equal wave number denoted as the second band, and so forth. Therefore, every electronic state is identified by both its wave number and band index, each with a clearly defined energy value. The energy of the nth band is denoted as $E_n(k)$, forming a nearly continuous function of wave number for each band, especially in extensive crystals where wave numbers allowed by periodic boundary conditions are densely packed. This set of functions $E_n(k)$, together forms the energy band structure. In a band structure diagram, the quantity of bands aligns with the count of atomic orbitals within the unit cell. The spectrum of energy eigenvalues in a periodic system culminates in the band structure, underscoring the profound impact of lattice periodicity on the behavior of electrons. In essence, the electronic band arrangement of the crystal emerges from the spreading out of isolated energy levels of atoms to form bands of allowable electron energies. This intricate interplay between electrons and the crystalline lattice ultimately defines the material's electronic properties.

3.11.2 Density of state (DOS)

The density of states (DOS) stands as a fundamental concept used to describe the electronic properties of solid materials. It arises from forming electronic energy bands within solids [34]. The DOS measures the quantity of electronic states electronic states per energy unit interval. We commonly express in relation to the density of states, denoted as $D(\varepsilon)$, which can be represented as: $D(\varepsilon) = \sum_i \delta(\varepsilon - \varepsilon_i)$.

In this equation, the summation extends over all the Kohn-Sham eigenvalues $\varepsilon_i(k)$. To gain insights into the electronic states surrounding individual atoms; we define the local density of states (LDOS) as the count of electronic states within a specific energy range within a volume around an atom [35]. We can further conceptualize the total DOS as the sum of the LDOS for all atoms in a crystal: $D(\varepsilon) = \sum_n d_n(\varepsilon)$.

In this equation, 'n' represents the different atoms within the unit cell, and $d_n(\varepsilon)$ is each atom's local density of states. The detailed decomposition of these local states into the state-resolved density of states is referred to as the projected density of states (PDOS).

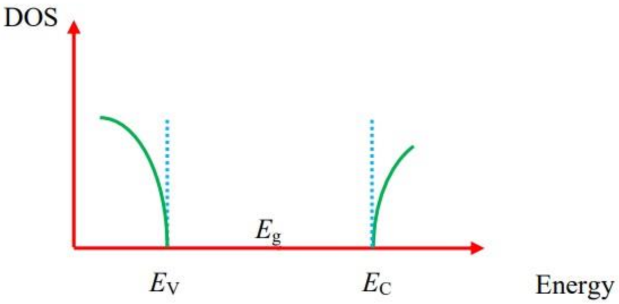

Figure 3.2: The Electronic Density of States (DOS) in crystalline solids near the band gap. The DOS can be segregated into two distinct regions: conduction and valence bands.

For a perfect crystal, the density of states exhibits a characteristic behavior: zero within the band gap. This is because the band gap (E_g) represents an energy range without electronic energy levels. In crystalline solids, the band gap is the boundary between two distinct regions known as the valence and conduction bands, as illustrated in Figure 3.2.

3.12 Optical Properties

Calculating optical spectra doesn't just consider occupied and unoccupied electronic states but also band characteristics. Therefore, exploring optical properties provides a deeper understanding of a material's electronic structure. The dielectric functions were calculated to analyze the frequency-dependent optical properties of semiconductors. The dielectric function (ε) is a well-known parameter that describes solid materials' optical behavior. Both components, the real part ($\varepsilon_1(\omega)$) and the imaginary part ($\varepsilon_2(\omega)$), were considered in the study as follows. [36]:

$$\varepsilon(\omega) = \varepsilon_1(\omega) + i\varepsilon_2(\omega) \qquad (34)$$

The real part ($\varepsilon_1(\omega)$) of the dielectric function describes how electromagnetic radiation polarizes and disperses, whereas the imaginary part ($\varepsilon_2(\omega)$) reflects the material's absorptive behavior. These elements are linked through the Kramers-Kronig relations [37]. The equation employed to calculate the real part ($\varepsilon_1(\omega)$) of the dielectric function based on the imaginary part is as follows [38]:

$$\varepsilon_1(\omega) = 1 + \frac{2}{\pi} p \int_0^\infty d\omega' \frac{\omega' \varepsilon_2(\omega')}{\omega'^2 - \omega^2} \qquad (35)$$

The principal value of the integral is denoted by P. The imaginary component ($\varepsilon_2(\omega)$) of the dielectric function elucidates the transitions between occupied and unoccupied states for a fixed Brillouin zone k-vector. This parameter relies on both the momentum matrix element and the density of states. The subsequent expression can be employed to compute $\varepsilon_2(\omega)$ [38,39]:

$$\varepsilon_2(\omega) = \left(\frac{h^2 e^2}{\pi m^2 \omega^2}\right) \sum_{i\,j} \int d^3 \mathrm{k} < i_k|p^\alpha|j_k >< j_k|p^\beta|i_k > x^\delta (\varepsilon_{i_k} - \varepsilon_{j_k} - \omega) \qquad (36)$$

The momentum matrix element (p) signifies the interaction between the states of bands α and β at the crystal momentum k. Here, the crystal wave vector k denotes the wave functions associated with the valence and conduction bands as i_k and j_k, respectively.

Through the utilization of the dielectric function, crucial optical parameters such as the absorption coefficient ($\alpha(\omega)$), refractive index ($n(\omega)$), and extinction coefficient ($k(\omega)$) can be determined.

$$\alpha(\omega) = \sqrt{2}\omega\left(\sqrt{\varepsilon_1^2(\omega) + \varepsilon_2^2(\omega)} - \varepsilon_1(\omega)\right)^{1/2} \tag{37}$$

$$n(\omega) = \frac{1}{\sqrt{2}}\left(\sqrt{\varepsilon_1^2(\omega) + \varepsilon_2^2(\omega)} + \varepsilon_1(\omega)\right)^{1/2} \tag{38}$$

$$k(\omega) = \frac{1}{\sqrt{2}}\left(\sqrt{\varepsilon_1^2(\omega) + \varepsilon_2^2(\omega)} - \varepsilon_1(\omega)\right)^{1/2} \tag{39}$$

The reflectance and optical conductivity can be inferred as provided below

$$R(\omega) = \left|\frac{\sqrt{\varepsilon(\omega)-1}}{\sqrt{\varepsilon(\omega)+1}}\right|^2 \tag{40}$$

$$\sigma(\omega) = -\frac{i\omega}{4\pi}\varepsilon(\omega) \tag{41}$$

3.13 Thermal Properties

The Debye temperature (Θ_D) serves as a parameter indicating the temperature of the highest normal mode of vibration within a crystal. It can be estimated utilizing the average sound velocity (V_m), which is contingent upon the elastic constants (the bulk modulus B and the shear modulus G). The Debye temperature can be calculated using the following expression [40]:

$$\Theta_D = \frac{h}{k_B}\left[\left(\frac{3n}{4\pi}\right)N_A\rho/M\right]V_m \tag{42}$$

In this equation, the parameters h, k_B, n, N_A, ρ, and M represent Planck's constant, Boltzmann's constant, the number of atoms in the molecule, Avogadro's number, the mass density, and the molar mass, respectively. The subsequent equation can approximate the average sound velocity in polycrystalline material:

$$V_m = \left[\frac{1}{3}\left(\frac{1}{v_l^3} + \frac{2}{v_t^3}\right)\right]^{-1/3} \tag{43}$$

Where, the longitudinal sound velocity (ν_l) and transverse sound velocity (ν_t) in a solid are connected to the elastic moduli (bulk and shear modulus) and density. Employing Navier's equation yields the following expression:

$$V_l = [(3B + 4G)/3\rho]^{1/2} \text{ and } V_t = [G/\rho]^{1/2} \qquad (44)$$

The empirical formula to ascertain the lattice thermal conductivity (K_{ph}) of ATaO3-xSx, derived by Slack [41], relies on the heat conduction stemming from the vibration of the lattice ions within a solid. It can be articulated as:

$$K_{ph} = \mathrm{A}(\gamma)\frac{M_{av}\Theta_D^3}{\gamma^2 n^{2/3} T} \text{ and } \gamma = \frac{3(1+\upsilon)}{2(2-3\upsilon)} \qquad (45)$$

Where the Grüneisen parameter, γ, represents the anharmonicity of the phonon, Upon computing the Grüneisen parameter, the coefficient $\mathrm{A}(\gamma)$ can be approximated utilizing the subsequent formula: $\mathrm{A}(\gamma) = \frac{4.85628\times10^7}{2(1-\frac{0.514}{\gamma}+\frac{0.228}{\gamma^2})}$ (46)

The modified Clarke's model [42] provides an expression for the theoretical minimum intrinsic thermal conductivity, given as: $K_{min} = K_B V_m \left(\frac{M}{n\rho N_A}\right)^{-\frac{2}{3}}$ (47)

The melting temperature (T_m) for $\mathrm{ATaO}_{3-x}\mathrm{S}_x$ has been conducted using the following equations [43]:

For cubic phases: $T_m(K) = 553 + (5.911)C_{11}$ (48)

For tetragonal phases: $T_m(K) = 3C_{11} + (1.5)C_{33} + 354$ (49)

References

[1] Wu Z, Cohen RE. More accurate generalized gradient approximation for solids. Phys Rev B 2006;73:235116. https://doi.org/10.1103/PhysRevB.73.235116.

[2] Hohenberg P, Kohn W. Inhomogeneous Electron Gas. Phys Rev 1964;136:B864–71. https://doi.org/10.1103/PhysRev.136.B864.

[3] Blaha P, Schwarz K, Madsen G, Kvasnicka D, Luitz J. WIEN2k: An Augmented Plane Wave plus Local Orbitals Program for Calculating Crystal Properties. Technische Universität Wien, Wien 2001;28.

[4] Pilania G, Ghosh A, Hartman ST, Mishra R, Stanek CR, Uberuaga BP. Anion order in oxysulfide perovskites: origins and implications. Npj Comput Mater 2020;6:1–11. https://doi.org/10.1038/s41524-020-0338-1.

[5] Perdew JP, Burke K, Ernzerhof M. Generalized Gradient Approximation Made Simple. Phys Rev Lett 1996;77:3865–8. https://doi.org/10.1103/PhysRevLett.77.3865.

[6] Koller D, Tran F, Blaha P. Merits and limits of the modified Becke-Johnson exchange potential. Phys Rev B 2011;83:195134. https://doi.org/10.1103/PhysRevB.83.195134.

[7] Jamal M, Bilal M, Ahmad I, Jalali-Asadabadi S. IRelast package. Journal of Alloys and Compounds 2018;735:569–79. https://doi.org/10.1016/j.jallcom.2017.10.139.

[8] Murnaghan FD. The Compressibility of Media under Extreme Pressures. Proc Natl Acad Sci USA 1944;30:244–7. https://doi.org/10.1073/pnas.30.9.244.

[9] Togo A, Tanaka I. First principles phonon calculations in materials science. Scripta Materialia 2015;108:1–5. https://doi.org/10.1016/j.scriptamat.2015.07.021.

[10] Baroni S, de Gironcoli S, Dal Corso A, Giannozzi P. Phonons and related crystal properties from density-functional perturbation theory. Rev Mod Phys 2001;73:515–62. https://doi.org/10.1103/RevModPhys.73.515.

[11] Andersen OK, Jepsen O. Explicit, First-Principles Tight-Binding Theory. Phys Rev Lett 1984;53:2571–4. https://doi.org/10.1103/PhysRevLett.53.2571.

[12] Togo A, Oba F, Tanaka I. First-principles calculations of the ferroelastic transition between rutile-type and $CaCl_2SiO_2$ at high pressures. Phys Rev B 2008;78:134106. https://doi.org/10.1103/PhysRevB.78.134106.

[13] Andersen OK. Linear methods in band theory. Phys Rev B 1975;12:3060–83. https://doi.org/10.1103/PhysRevB.12.3060.

[14] Koelling DD, Arbman GO. Use of energy derivative of the radial solution in an augmented plane wave method: application to copper. J Phys F: Met Phys 1975;5:2041. https://doi.org/10.1088/0305-4608/5/11/016.

[15] Wimmer E, Krakauer H, Weinert M, Freeman AJ. Full-potential self-consistent linearized-augmented-plane-wave method for calculating the electronic structure of molecules and surfaces: O_2 molecule. Phys Rev B 1981;24:864–75. https://doi.org/10.1103/PhysRevB.24.864.

[16] Dürr D, Teufel S. Schrödinger's Equation. In: Teufel S, Dürr D, editors. Bohmian Mechanics: The Physics and Mathematics of Quantum Theory, Berlin, Heidelberg: Springer; 2009, p. 129–43. https://doi.org/10.1007/b99978_7.

[17] Thomas LH. The calculation of atomic fields. Mathematical Proceedings of the Cambridge Philosophical Society 1927;542. https://doi.org/10.1017/S0305004100011683.

[18] Elbadawi AA, Yassin OA, Siddig MA. Effect of the Cation Size Disorder at the A-Site on the Structural Properties of SrAFeTiO Double Perovskites (A = La, Pr or Nd). MSCE 2015;03:21–9. https://doi.org/10.4236/msce.2015.35003.

[19] Kohn W, Sham LJ. Self-Consistent Equations Including Exchange and Correlation Effects. Phys Rev 1965;140:A1133–8. https://doi.org/10.1103/PhysRev.140.A1133.

[20] Perdew JP, Wang Y. Accurate and simple analytic representation of the electron-gas correlation energy. Phys Rev B 1992;45. https://doi.org/10.1103/PhysRevB.45.13244.

[21] Becke AD. Density-functional thermochemistry. III. The role of exact exchange. Journal of Chemical Physics 1993;98:5648–52. https://doi.org/10.1063/1.464913.

[22] Perdew JP, Ernzerhof M, Burke K. Rationale for mixing exact exchange with density functional approximations. The Journal of Chemical Physics 1996;105:9982–5. https://doi.org/10.1063/1.472933.

[23] Tran F, Blaha P. Accurate Band Gaps of Semiconductors and Insulators with a Semilocal Exchange-Correlation Potential. Phys Rev Lett 2009;102:226401. https://doi.org/10.1103/PhysRevLett.102.226401.

[24] Wang J, Yip S, Phillpot SR, Wolf D. Crystal instabilities at finite strain. Phys Rev Lett 1993;71:4182–5. https://doi.org/10.1103/PhysRevLett.71.4182.

[25] Kuma S, Woldemariam MM. Structural, Electronic, Lattice Dynamic, and Elastic Properties of $SnTiO_3$ and $PbTiO_3$ Using Density Functional Theory. Advances in Condensed Matter Physics 2019;2019:3176148. https://doi.org/10.1155/2019/3176148.

[26] Yan H, Wei Z, Zhang M, Wei Q. Exploration of stable stoichiometries, ground-state structures, and mechanical properties of the W–Si system. Ceramics International 2020;46:17034–43. https://doi.org/10.1016/j.ceramint.2020.03.290.

[27] Voigt, W. (1889) Ueber die Beziehung zwischen den beiden Elastizita tskonstanten isotroper Korper. Annalen der Physik, 38, 573-587. - References - Scientific Research Publishing.https://www.scirp.org/(S(lz5mqp453edsnp55rrgjct55))/reference/ReferencesPapers.aspx?ReferenceID=1704455 (accessed October 3, 2023).

[28] Hachemi A, Hachemi H, Ferhat-Hamida A, Louail L. Elasticity of $SrTiO_3$ perovskite under high pressure in cubic, tetragonal and orthorhombic phases. Phys Scr 2010;82:025602. https://doi.org/10.1088/0031-8949/82/02/025602.

[29] Zuo L, Humbert M, Esling C. Elastic properties of polycrystals in the Voigt-Reuss-Hill approximation. J Appl Cryst 1992;25. https://doi.org/10.1107/S0021889892004874.

[30] Hill R. The Elastic Behaviour of a Crystalline Aggregate. Proc Phys Soc A 1952;65:349. https://doi.org/10.1088/0370-1298/65/5/307.

[31] Ju L, Dar SA. Probing the Structural, Electronic, Mechanical Strength and Thermodynamic Properties of Tungsten-Based Oxide Perovskites $RbWO_3$ and $CsWO_3$: First-Principles Investigation. J Electron Mater 2019;48. https://doi.org/10.1007/s11664-019-07277-5.

[32] Zener CM, Siegel S. Elasticity and Anelasticity of Metals. ACS Publications 2002. https://doi.org/10.1021/j150474a017.

[33] Tvergaard V, Hutchinson JW. Microcracking in Ceramics Induced by Thermal Expansion or Elastic Anisotropy. Journal of the American Ceramic Society 1988;71:157–66. https://doi.org/10.1111/j.1151-2916.1988.tb05022.x.

[34] Mistrik J, Kasap S, Ruda HE, Koughia C, Singh J. Optical Properties of Electronic Materials: Fundamentals and Characterization. In: Kasap S, Capper P, editors. Springer Handbook of Electronic and Photonic Materials, Cham: Springer International Publishing; 2017, p. 1–1. https://doi.org/10.1007/978-3-319-48933-9_3.

[35] Sholl DS, Steckel JA. Density functional theory: a practical introduction. John Wiley & Sons; 2022.

[36] Hilal M, Rashid B, Khan SH, Khan A. Investigation of electro-optical properties of InSb under the influence of spin-orbit interaction at room temperature. Materials Chemistry and Physics 2016;184. https://doi.org/10.1016/j.matchemphys.2016.09.009.

[37] Xiong K, Robertson J, Clark SJ. Defect states in the high-dielectric-constant gate oxide $LaAlO_3$. Applied Physics Letters 2006;89. https://doi.org/10.1063/1.2221521.

[38] Ahmad Dar S, Sharma R, Srivastava V, Kumar Sakalle U. Investigation on the electronic structure, optical, elastic, mechanical, thermodynamic and thermoelectric properties of wide band gap semiconductor double perovskite Ba_2InTaO_6. RSC Advances 2019;9:9522–32. https://doi.org/10.1039/C9RA00313D.

[39] Noor NA, Rashid M, Alay-e-Abbas SM, Raza M, Mahmood A, Ramay SM, et al. Shift of indirect to direct bandgap and thermoelectric response of the cubic $BiScO_3$ via DFT-mBJ studies. Materials Science in Semiconductor Processing 2016;49:40–7. https://doi.org/10.1016/j.mssp.2016.03.014.

[40] Anderson OL. A simplified method for calculating the debye temperature from elastic constants. Journal of Physics and Chemistry of Solids 1963;24:909–17. https://doi.org/10.1016/0022-3697(63)90067-2.

[41] Slack GA. The Thermal Conductivity of Nonmetallic Crystals. In: Ehrenreich H, Seitz F, Turnbull D, editors. Solid State Physics, vol. 34, Academic Press; 1979, p. 1–71. https://doi.org/10.1016/S0081-1947(08)60359-8.

[42] Clarke DR. Materials selection guidelines for low thermal conductivity thermal barrier coatings. Surface and Coatings Technology 2003;163–164:67–74. https://doi.org/10.1016/S0257-8972(02)00593-5.

[43] Fine ME, Brown LD, Marcus HL. Elastic constants versus melting temperature in metals. Scripta Metallurgica 1984;18:951–6. https://doi.org/10.1016/0036-9748(84)90267-9.

Chapter 4: RESULTS AND DISCUSSION

In this research, we utilized DFT-based methodologies to determine the physical characteristics of $ATaO_{3-x}S_x$ (A = K, Rb, Cs). This chapter covers the presentation of the obtained properties, relevant discussion, and correlation among them.

4.1 Structural Properties

$ATaO_3$ exhibits a perovskite structure with a cubic crystal lattice belonging to space group Pm3m (#221). The atomic coordinates consist of A (= K, Rb, Cs) located at the unit cell center (0, 0, 0), Ta situated at the corner (0.5, 0.5, 0.5), and O positioned at the face center (0, 0.5, 0.5) [1–3]. In $ATaO_2S$, the atomic arrangements are as follows: A (0, 0, 0), Ta (0.5, 0.5, 0.5), O (0.5, 0, 0.5), and S (0, 0.5, 0.5). For $ATaOS_2$, the atomic positions are: A (0, 0, 0), Ta (0.5, 0.5, 0.5), O (0.5, 0.5, 0), and S (0.5, 0, 0.5). This substitution induces a shift in crystal structure from cubic to tetragonal, with the space group for these transitions being P4/mmm (123). Furthermore, when three sulfur atoms replace oxygen in the parent compound, $ATaS_3$ is formed, maintaining a cubic structure with identical space group and atomic positions as $ATaO_3$. For better understanding we also perform 2x1x1 supercell crystal structure calculation for $ATaO_2S$ and $ATaOS_2$ phases.

Volume optimization was conducted for the cubic structures of $ATaO_3$ and $ATaS_3$, resulting in the determination of their respective minimum energy volumes, as depicted in the figure. To assess the structural stability and the correlation between total energy and volume for these compounds, we employed the third-order Birch-Murnaghan equation of state [4,5].

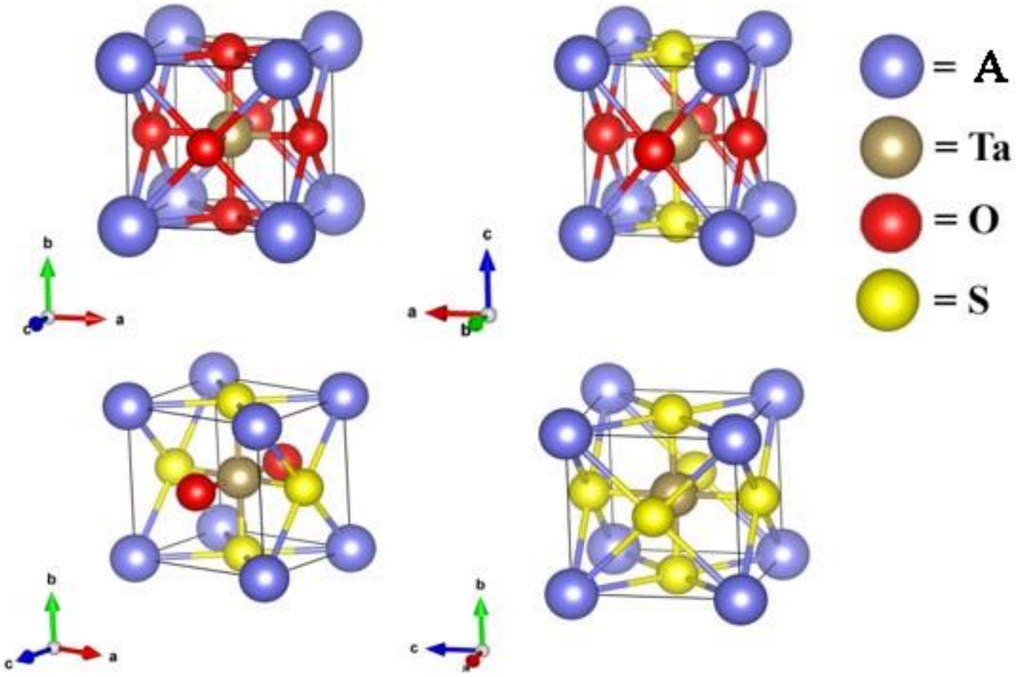

Fig. 4.1: The unit cells of $ATaO_{3-x}S_{x}$.

For the remaining two tetragonal structures, structure optimization was conducted in two stages. Initially, volume variation was carried out while keeping the c/a ratio constant. The obtained volume data was then fitted using the Birch-Murnaghan equation of state (EOS), as illustrated in Figure 4.2-4.4.

Subsequently, the equilibrium volume was held constant while the *c/a* ratio was varied, determined through a parabolic fit. The result of this geometrical optimization, including lattice parameters and other structural data for both cubic and tetragonal compounds, is included in Table 4.1. The deviation of lattice parameters for parent compounds is very low (~ 0.1%), which justifies the present calculation accuracy.

Table 4.1: The optimized crystallographic lattice parameters, *a* and *c* (both in Å), volume of unit cell V (Å^3) of perovskite ATaO$_{3-x}$S$_x$ compounds, and the percentage of deviation from the reference data.

Compounds	***a* (Å)**	***c*(Å)**	**% of deviation**	**V (Å^3)**	**Formation energy**	**Ref**
KTaO$_3$	4.0321	-	1.093	65.553	-3.0220	3.9885 [6] 3.988 [7]^{expt}
RbTaO$_3$	4.0750	-	0.1769	67.838	-2.8328	4.0678 [8]
CsTaO3	4.1415	-	1.259	71.035	-2.0322	4.09 [3]
KTaO$_2$S	4.1385	4.9164	-	84.204	-1.7310	This study
RbTaO$_2$S	4.1962	4.8936	-	86.129	-1.6410	This study
CsTaO$_2$S	4.2723	4.9130	-	89.677	-1.3156	This study
KTaOS$_2$	4.9432	4.1239	-	100.769	-1.0789	This study
RbTaOS$_2$	4.9698	4.1587	-	102.67	-0.9524	This study
CsTaOS$_2$	5.0188	4.2052	-	105.923	-0.6452	This study
KTaS$_3$	4.8690	-	-	115.437	-0.7353	This study
RbTaS$_3$	4.8940	-	-	117.217	-0.6809	This study
CsTaO$_3$	4.9335	-	-	120.078	-0.5781	This study

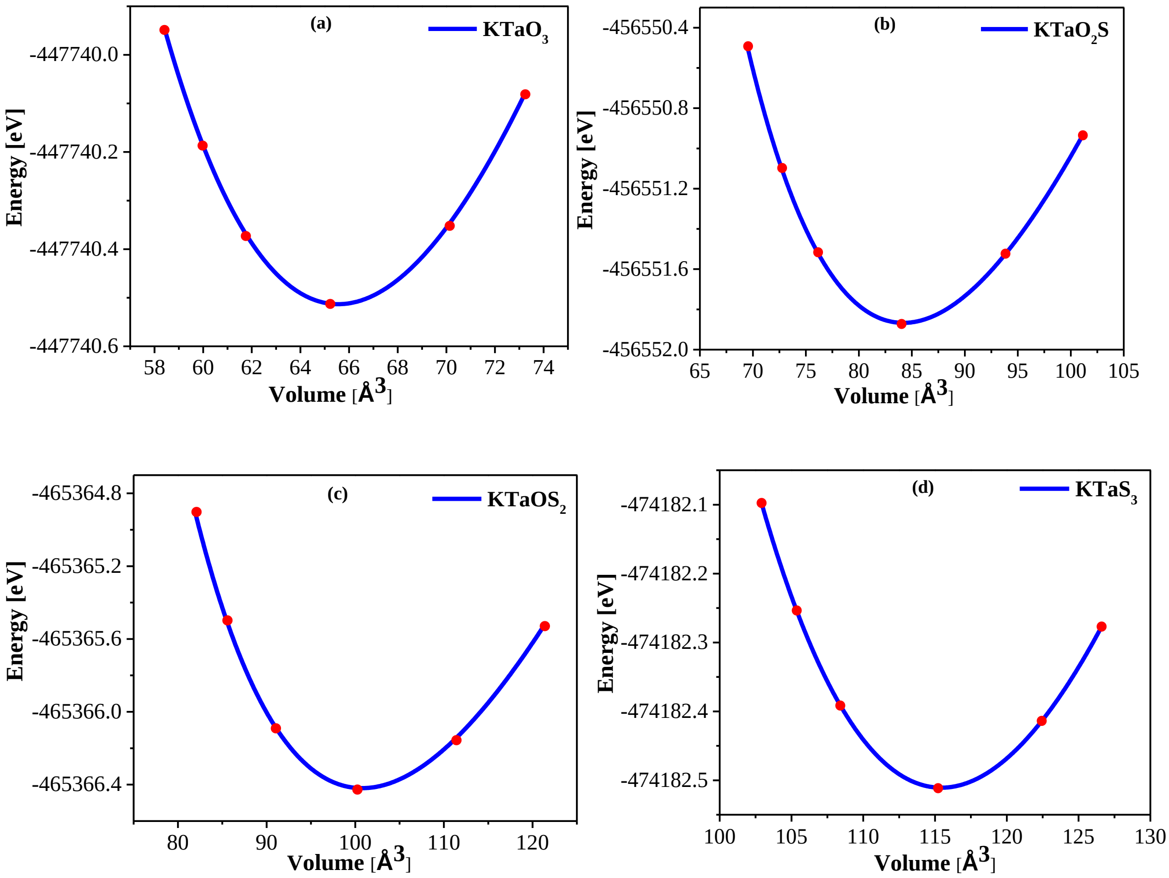

Figure 4.2: Volume vs. total energy curves for (a) KTaO$_3$, (b) KTaO$_2$S, (c) KTaOS$_2$, and (d) KTaS$_3$.

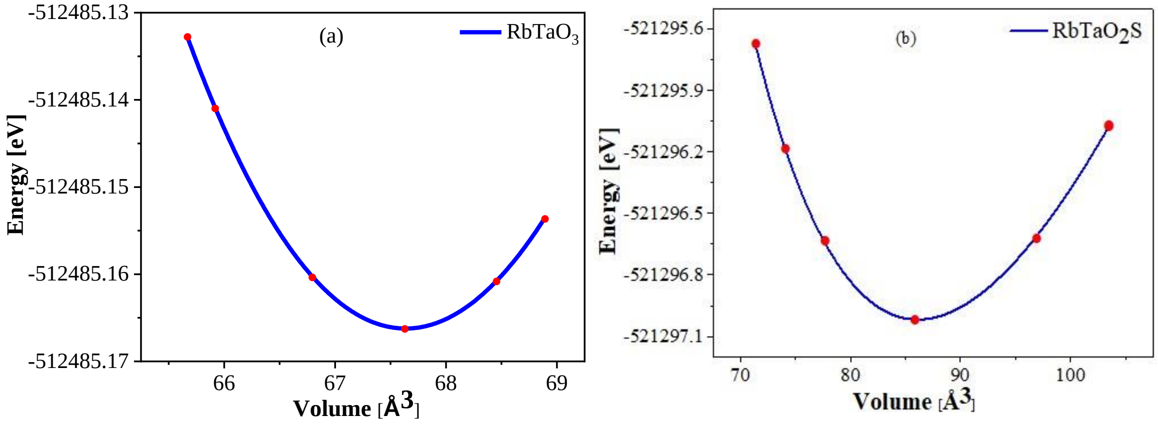

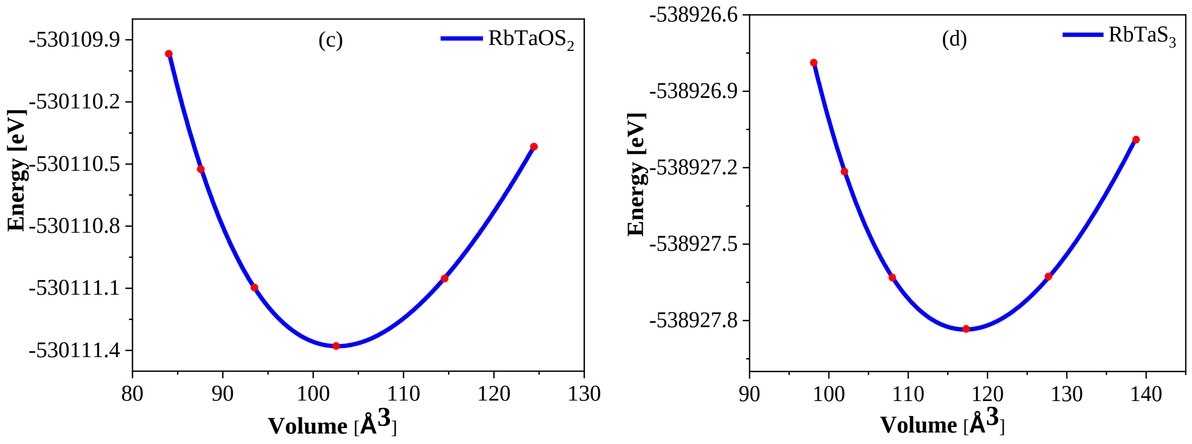

Figure 4.3: Volume vs. total energy curves for (a) $RbTaO_3$, (b) $RbTaO_2S$, (c) $RbTaOS_2$, and (d) $RbTaS_3$.

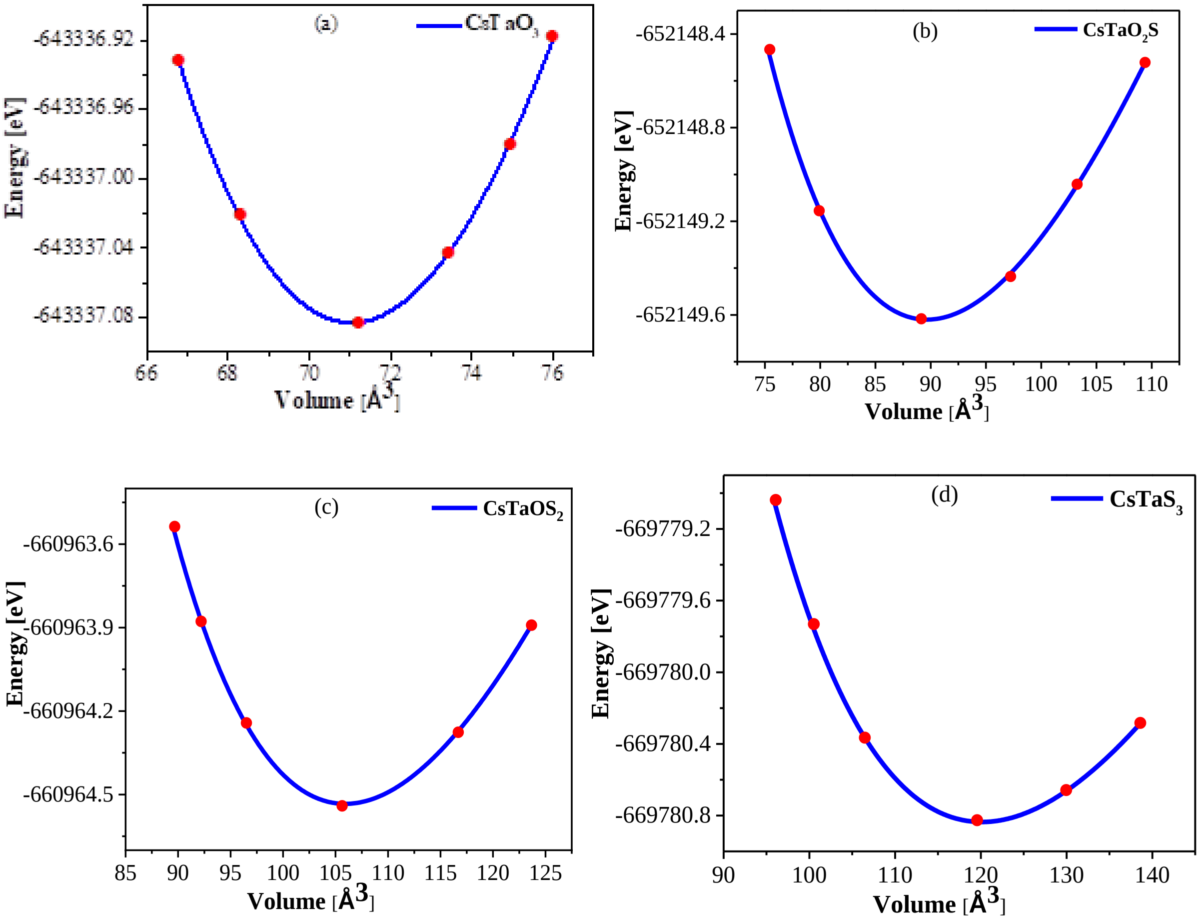

Figure 4.4: Volume vs. total energy curves for (a) $CsTaO_3$, (b) $CsTaO_2S$, (c) $CsTaOS_2$, and (d) $CsTaS_3$.

The formation energy of a compound is a measure of the stability of that compound relative to its constituent elements in their most stable forms. It's usually defined as the energy change associated with the formation of one mole of a compound from its elements in their standard states. Table 4.1 presents the predicted formation energies for $ATaO_3$, $ATaO_2S$, $ATaOS_2$, and $ATaS_3$. These values provide insight into their relative stability and illuminate their chemical behavior.

4.2 Dynamical stability

we assessed the dynamic stability of the system by calculating the phonon dispersions, which represent the system's ability to withstand small atomic displacements caused by either thermal or imposed periodic motions [9]. We employed the finite displacement method using the PHONOPY software [10] to derive the phonon dispersions. For the cubic phase, we computed the force constants using a (2 × 2 × 2) supercell, while for the tetragonal phase, calculations were conducted with both (1 × 1 × 1) and (2 × 2 × 2) supercells. During the calculations, atomic displacements of 0.01 Å were applied along the lattice vectors. The analysis of the phonon frequency range spanned the entire Brillouin zone, with positive frequencies indicating stability and negative frequencies indicating instability. Fig. 4.5, 4.6, and 4.7 indicate that the phonon dispersion curves of the $ATaO_{3-x}S_x$ (A = K, Rb, Cs) compounds do not exhibit any negative frequencies, demonstrating their dynamic stability. Unfortunately, no experimental investigations are available on the dynamic characteristics of these compounds.

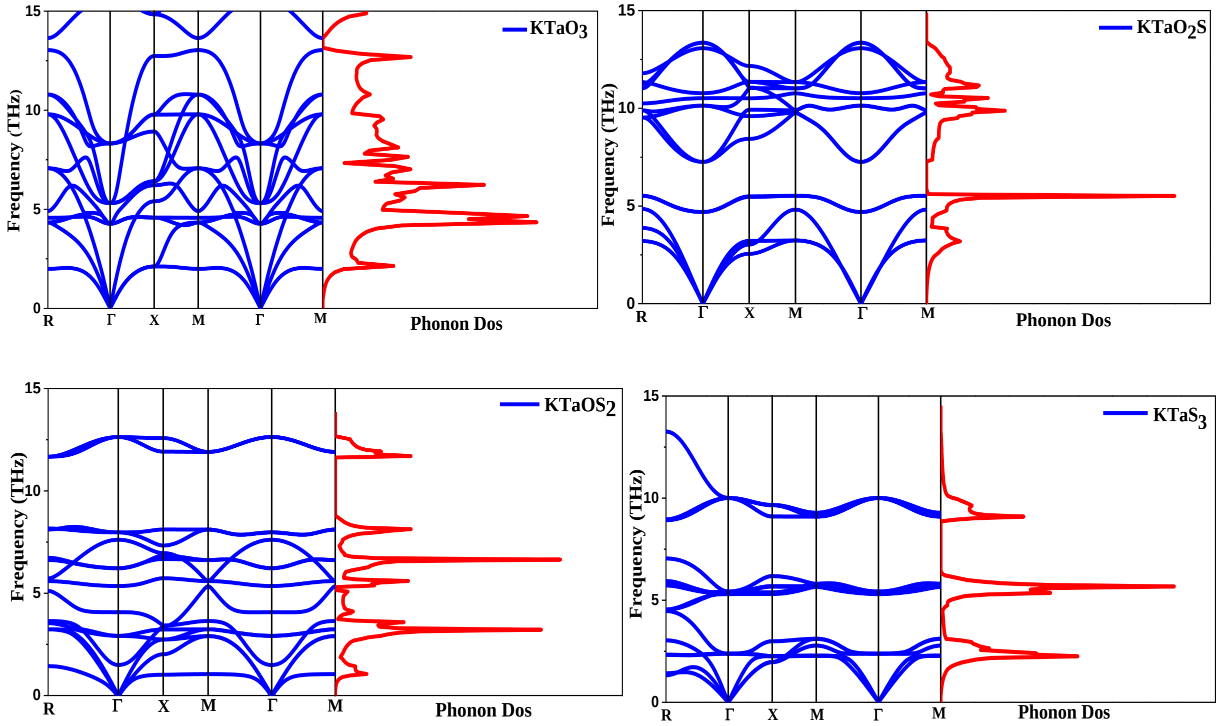

Figure 4.5: Phonon dispersion curve and phonon DOS of $KTaO_{3-x}S_x$ compounds.

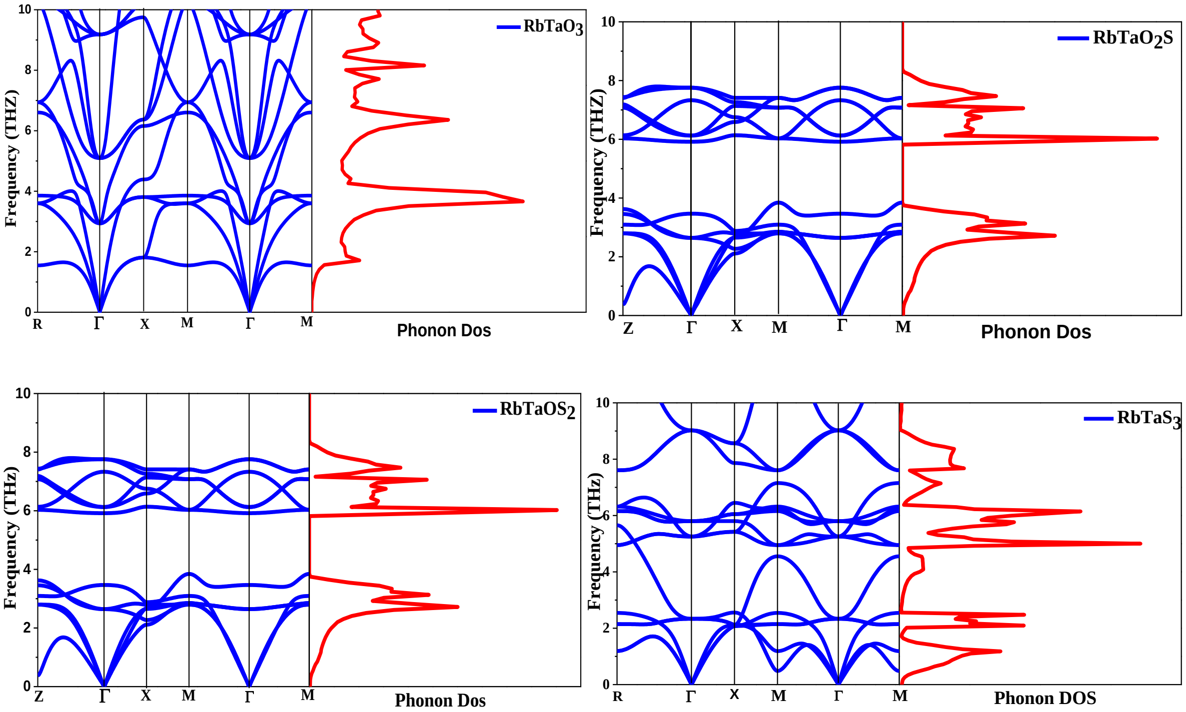

Fig. 4.6: Phonon dispersion curve and phonon DOS of $RbTaO_{3-x}S_x$ compounds.

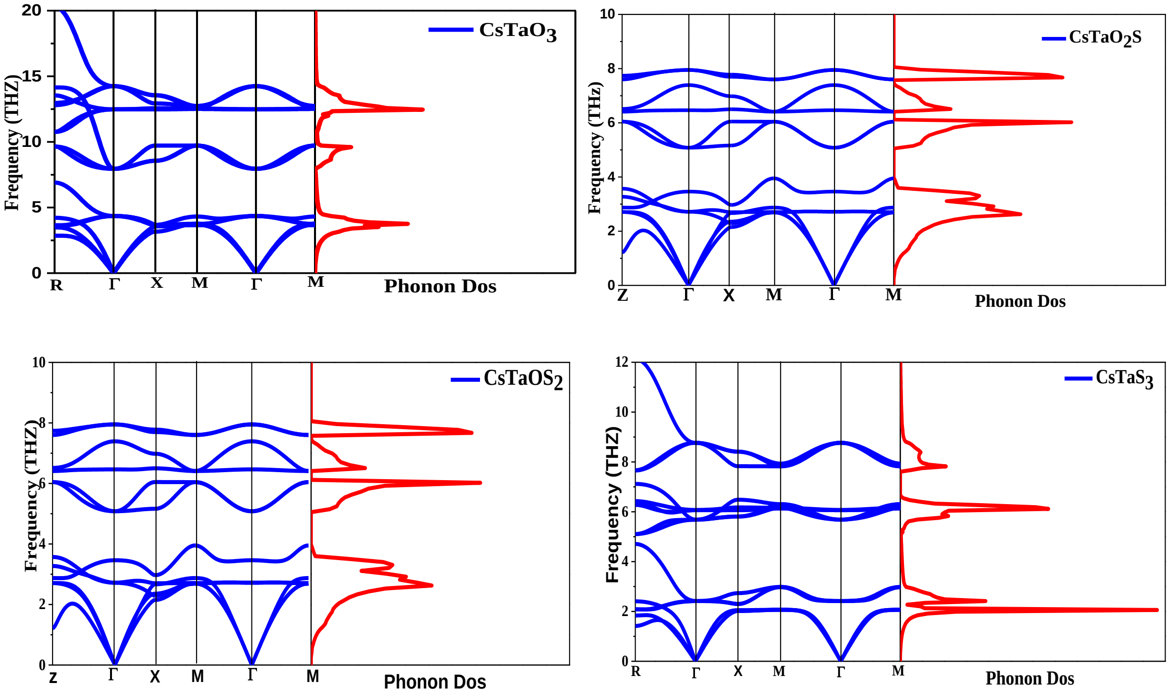

Fig. 4.7: Phonon dispersion curve and phonon DOS of CsTaO$_{3-x}$S$_x$ compounds.

The PDCs provide additional information regarding the studied compounds. Due to the presence of five atoms in the unit cell of these compounds, the PDCs exhibit a total of 15 vibrational modes. Three modes are acoustic modes, while the remaining 12 are optical modes. At low values of the crystal wave vector, the three lowest modes exhibit a dispersion curve in the form of $\omega = vk$, which corresponds to the $\omega(k)$ relationship observed in sound waves and belongs to the acoustic branch. Out-of-phase oscillations of atoms induced by photon excitation give rise to the upper vibrational modes, which constitute the optical branch. At the Γ-point, acoustic modes have zero frequency. No phononic band gap is found in the cubic phases of ATaO$_3$ and ATaS$_3$, but the tetragonal phases of ATaO$_2$S and ATaOS$_2$ have a band gap between acoustic modes and lower optical branches.

4.3 *Electronics Properties*

The band structure, electronic density of states (DOS), and charge density distribution of $ATaO_{3-x}S_x$ have been investigated to illustrate the electronic properties and chemical bonding nature of the material. The modified Becke-Johnson exchange potential, known for its accuracy in predicting energy band gaps of semiconducting and insulating materials, was employed [11,12]. Both TB-mBJ and GGA-PBE approaches were utilized to search for band gaps, and Table 4.2 presents the estimated band gap values for $ATaO_{3-x}S_x$ compounds, showcasing significant variation across different functionals. The electronic band structure and density of states (DOS) were calculated using the TB-mBJ potential, as illustrated in the figure. Band structure results are presented for $ATaO_{3-x}S_x$ along high symmetry directions within the Brillouin zone, covering the R, Γ, X, M, Γ paths for cubic structures, and Z, Γ, X, M, Γ for tetragonal structures, with the Fermi-Level set at 0 eV. In all calculated phases, the top of the valence band (TVB) and the bottom of the conduction band (BCB) are situated at different k-points, suggesting the indirect band gap semiconductor nature of the investigated phases.

The uppermost energy region of the valence band (near the Fermi level) predominantly arises from the *p* states of O or *S* atoms and the *d* state of Ta atoms in $ATaO_{3-x}S_x$. Similarly, the lower end of the conduction bands is attributed to the hybridization involving the *d* states of the Ta atom. The computed band gap values for $ATaO_3$ using the GGA and TB-mBj potential are as follows: 2.320 eV and 3.572 eV for $KTaO_3$, 2.219 eV and 2.717 eV for $RbTaO_3$, and 2.05 eV and 3.076 eV for $CsTaO_3$, respectively. These values are reasonably consistent with other predicted band gap values, as reported in Table 4.2.

Table 4.2: Estimated bandgaps of perovskite $ATaO_{3-x}S_x$ compounds.

Compounds	**Approach**	**Bandgap (eV)**	**Ref**
$KTaO_3$	GGA-PBE	2.320 2.11	This study [13]
	TB-mBJ	3.572 3.64, 3.50, 3.60	This study [13–15]
$RbTaO_3$	GGA-PBE	2.219 2.053, 2.16	This study [8,16]
	TB-mBJ	2.717 2.75	This study [3]
$CsTaO_3$	GGA-PBE	2.055 2.03, 2.07	This study [3]
	TB-mBJ	3.076 3.15, 2.83, 2.9	This study [3]
$KTaO_2S$	GGA-PBE TB-mBJ	1.033 1.808	This study This study
$KTaO_2S$ (SC)	GGA-PBE TB-mBJ	0.909 1.706	This study This study
$RbTaO_2S$	GGA-PBE TB-mBJ	0.710 1.438	This study This study
$RbTaO_2S$ (SC)	GGA-PBE TB-mBJ	0.635 1.378	This study This study
$CsTaO_2S$	GGA-PBE TB-mBJ	0.307 0.909	This study This study

CsTaO$_2$S (SC)	GGA-PBE TB-mBJ	0.229 0.854	This study This study
KTaOS$_2$	GGA-PBE TB-mBJ	0 0.264	This study This study
KTaOS$_2$ (SC)	GGA-PBE TB-mBJ	0 0.241	This study This study
RbTaOS$_2$	GGA-PBE TB-mBJ	0 0.286	This study This study
RbTaOS$_2$ (SC)	GGA-PBE TB-mBJ	0 0.263	This study This study
CsTaOS$_2$	GGA-PBE TB-mBJ	0.036 0.376	This study This study
CsTaOS$_2$ (SC)	GGA-PBE TB-mBJ	0 0.353	This study This study
KTaS$_3$	GGA-PBE TB-mBJ	0 0.078	This study This study
RbTaS$_3$	GGA-PBE TB-mBJ	0 0.103	This study This study
CsTaS$_3$	GGA-PBE TB-mBJ	0 0.143	This study This study

The band gap calculated using TB-mBJ potential for other compounds is 1.808 eV ($KTaO_2S$), 0.264 eV ($KTaOS_2$), 0.078 eV ($KTaOS_3$), 1.438 eV ($RbTaO_2S$), 0.286 eV ($RbTaOS_2$), 0.103 eV ($RbTaS_3$), 0.909 eV ($CsTaO_2S$), 0.376 eV ($CsTaOS_2$), and 0.143 eV ($CsTaS_3$). These results indicate that substituting S can dramatically decrease the band gap of $ATaO_3$. The band gap of $RbTaO_2S$ is very close to that of the Shockley-Queiser limit for the band gap of solar cell materials to achieve the highest efficiency [17]. Moreover, the band gap is further reduced with increased S contents. Thus, the electrical conductivity of the S-substituted compositions is expected to be improved with the band gap reduction. For $KTaO_3$, our calculated values agree with the experimental results. Moreover, they closely resemble previously computed values for the indirect band gap [7,15,18,19]. However, no experimental data regarding these parameters for $RbTaO_3$ and $CsTaO_3$ is currently available in the literature. The band gap for $ATaO_2S$ and $ATaOS_2$ is also calculated via the 211 super-cell (SC) approach using GGA and TB-mBJ functionals. It is found to be consistent with each other [Table 4.2], which ensures the accuracy of the obtained results.

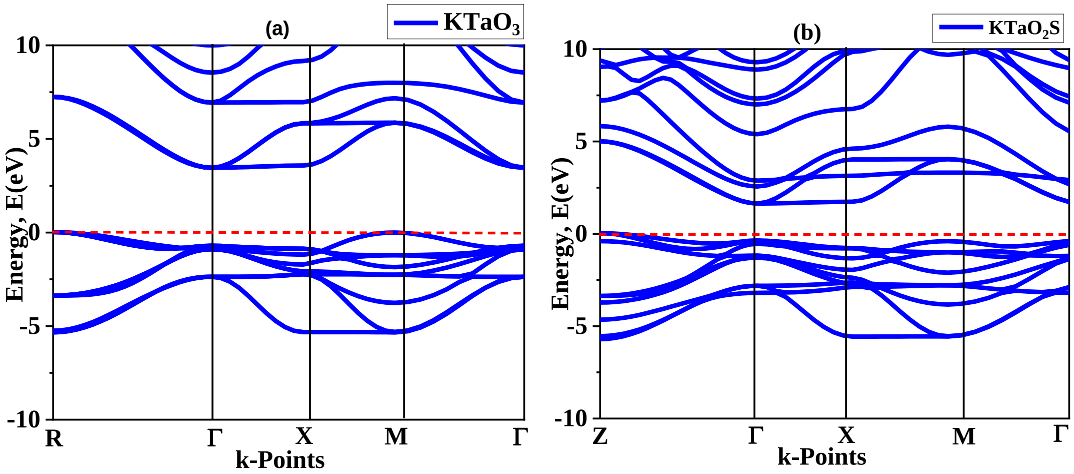

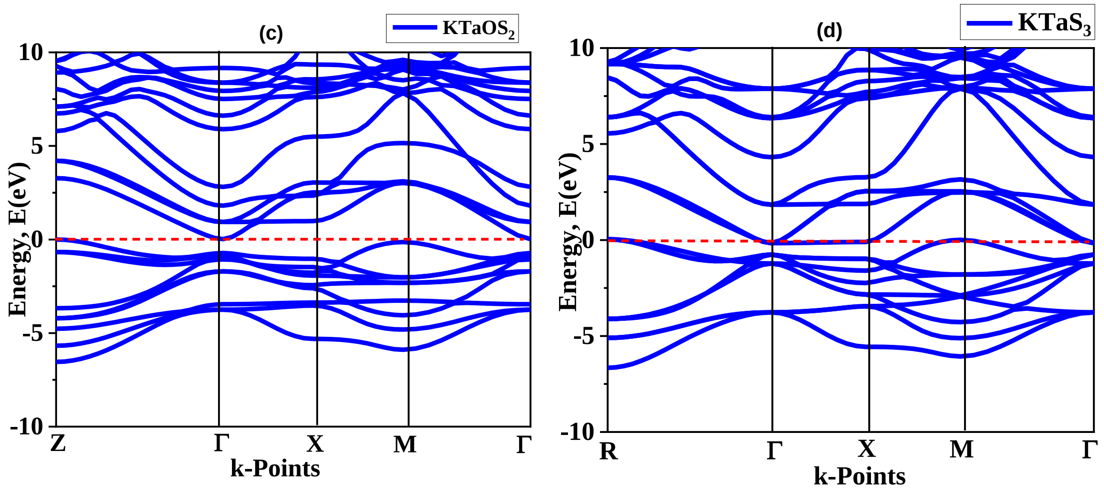

Fig. 4.8: Electronic band structures of KTaO$_{3-x}$S$_x$ compounds using TB-mBJ.

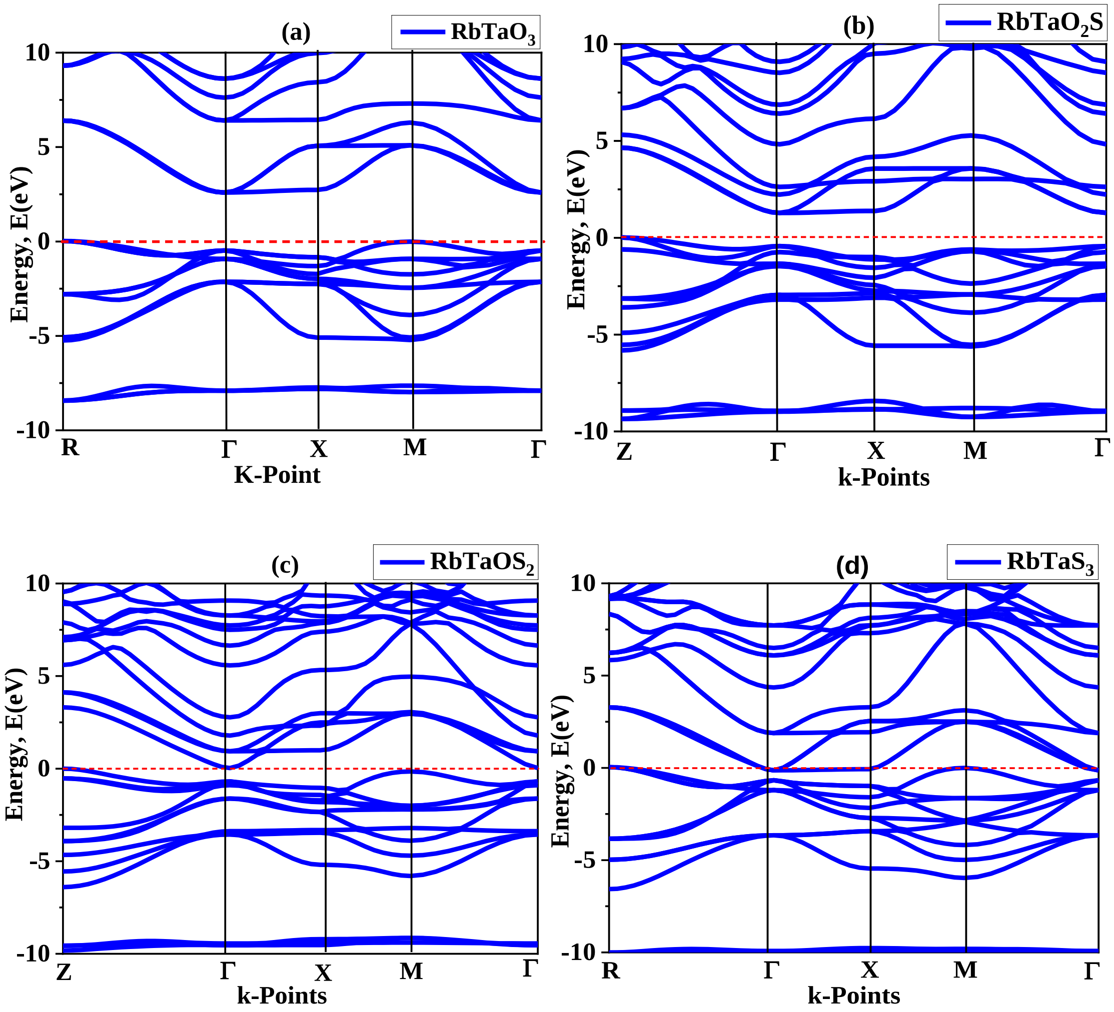

Fig. 4.9: Electronic band structures of RbTaO$_{3-x}$S$_x$ compounds using TB-mBJ.

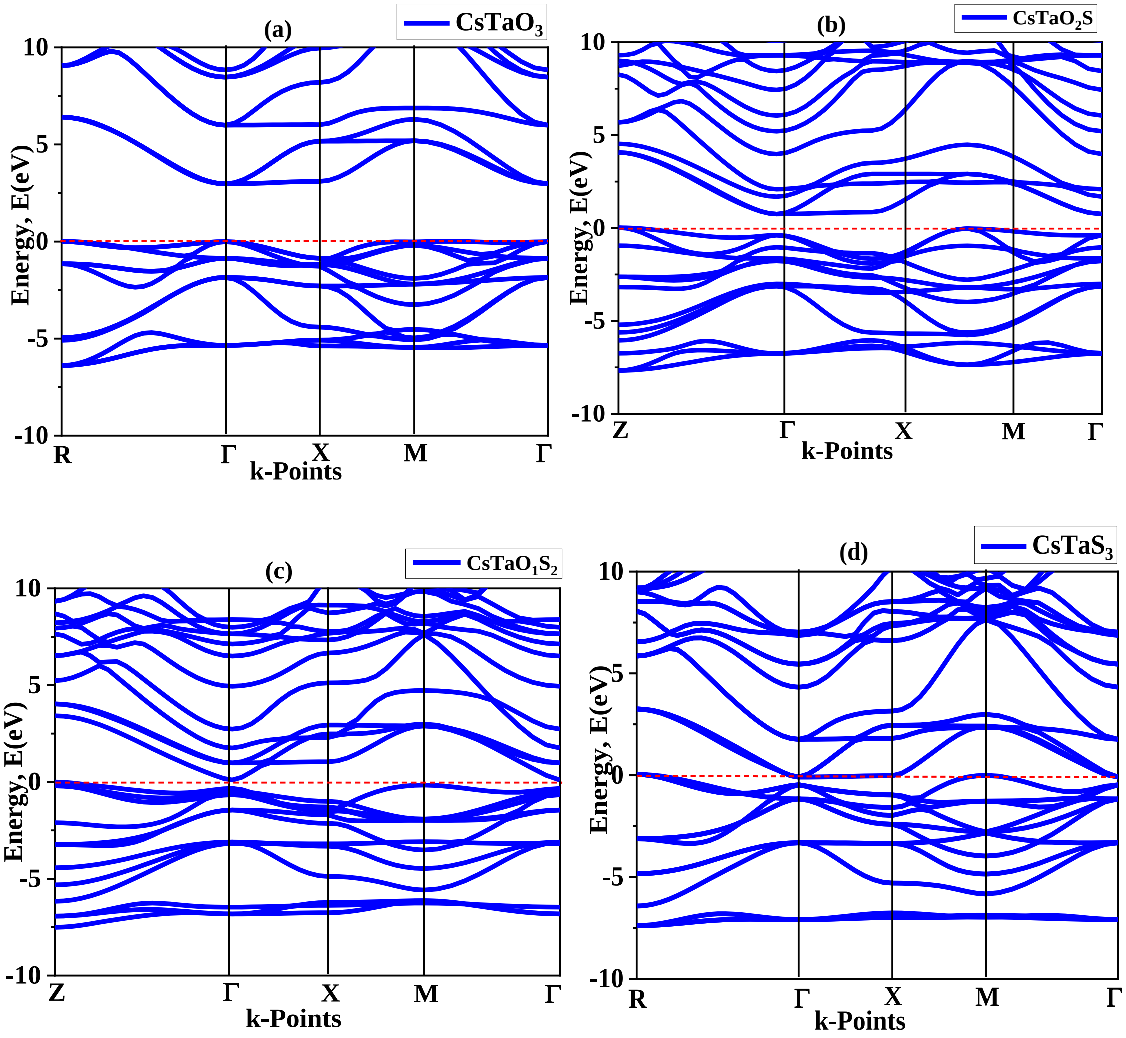

Fig. 4.10: Electronic band structures of $CsTaO_{3\text{-}s}S_x$ compounds using TB-mBJ.

The total and partial density of states (DOS) have been studied to understand the orbital contributions to atomic bonding and the formation of valence and conduction states. The band structure and density of the state of various compositions exhibit considerable similarities. In $ATaO_3$ (A= K, Rb, Cs), the PDOS plot revealed that A-*p*, Ta-*d*, and O-*p* states contributed to the valence band in the deeper region, indicating a pronounced hybridization among them. Upon substituting one, two, and three sulfur atoms in $ATaO_3$, a noticeable reduction in the contribution of A-*p* states in the valence band near the Fermi level was observed. However, an increase in the contribution of S-*p* states compensated for this reduction in the A-*p* contribution. Consequently, the substitution of S for O in $ATaO_3$ induced alterations in the material's electronic structure, leading to changes in the contributions of the atomic orbitals to the valence band. Specifically, the S-*p* states began to significantly contribute to the valence band, while the A-*p* contribution decreased. The conduction band of $ATaO_3$ displayed notable hybridization between Ta-*d* and O-*p* states near the Fermi level, primarily responsible for forming the band gap. At higher energy levels in the conduction band (around 10 eV), hybridization occurred among A-*d*, Ta-*d*, and O-*p* states, albeit with a modest contribution from O-*p* states. Upon substitution of one, two, or three sulfur atoms for oxygen, S-*p* states contributed near the Fermi level and hybridized with Ta-*d* states. Pseudo-states of tantalum (Ta-*d*) played a significant role in forming both valence and conduction bands.

The electron charge density provides crucial insights into the chemical bonding within a unit cell, often visualized through charge density maps (CDMs) [20]. When investigating $ATaO_{3-x}S_x$ compounds, understanding bonding characteristics relies heavily on electronic charge density contour plots. These plots, computed using the TB-mBJ functional, offer a comprehensive exploration of bonding properties and charge conveyance within the material. Figures 4.11-4.13 depict charge density contour plots obtained for various planes, providing insights into the chemical bonds in $ATaO_{3-x}S_x$. These plots reveal predominantly ionic bonds with some covalent features. Circular patterns in charge density surrounding the A-cations (K, Rb, Cs) indicate their distinctive ionic character. Meanwhile, the closely packed lines around Ta and O atoms suggest shared electrons, highlighting significant covalent contributions to the Ta-O bonds. Additionally, these contour plots illustrate the charge flow between valence and conduction bands, influencing variations in charge distribution around oxygen and tantalum atoms in $ATaO_3$. Replacing one or two oxygen atoms with sulfur maintains the strength of the covalent bond between Ta and O, while simultaneously introducing new covalent bonds between Ta and S atoms. However, the covalent bonds between O and Ta atoms are stronger than the newly formed Ta-S bonds. Substituting three sulfur atoms for oxygen leads to a weaker covalent bond between S and Ta atoms, which notably impacts the mechanical properties of the compound. This leads to reduced hardness and a lower melting temperature than compounds with fewer sulfur substitutions, primarily due to the weakened covalent bond between Ta and S. This weakened bond also has implications for stability and intermolecular interactions, impacting the thermomechanical characteristics of the phase. The selection of atoms for replacement plays a pivotal role in shaping the properties of the final compound. Electronegativity values, as determined by the Linus-Pauling scale, are crucial for assessing covalent bond strength [21]. When atoms engage in a covalent bond, its strength hinges on their respective tendencies to attract electrons. Oxygen exhibits a greater affinity for electron acquisition compared to sulfur. Consequently, when tantalum forms a bond with oxygen, electrons tend to localize more towards the oxygen side, resulting in a stronger Ta-O bond compared to when bonding with sulfur (Ta-S bond). This detail is pivotal in understanding the distribution of charge and the bonding patterns within compounds like $ATaO_{3-x}S_x$. It's akin to deciphering why certain bonds are more resilient based on the atoms involved.

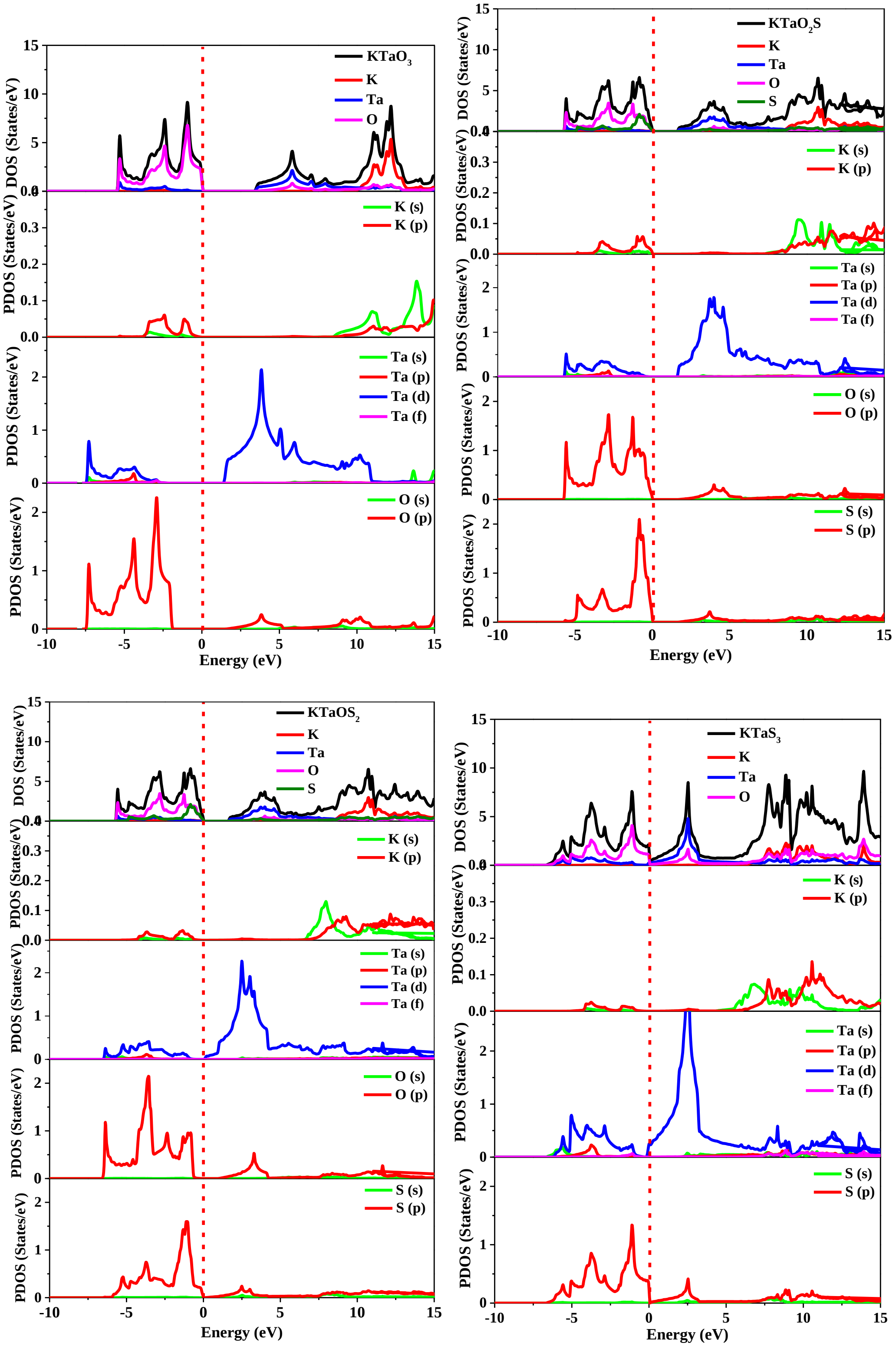

Figure 4.11: The density of states (DOS) of (a) $KTaO_3$, (b) $KTaO_2S$, (c) $KTaOS_2$, and (d) $KTaS_3$ compounds.

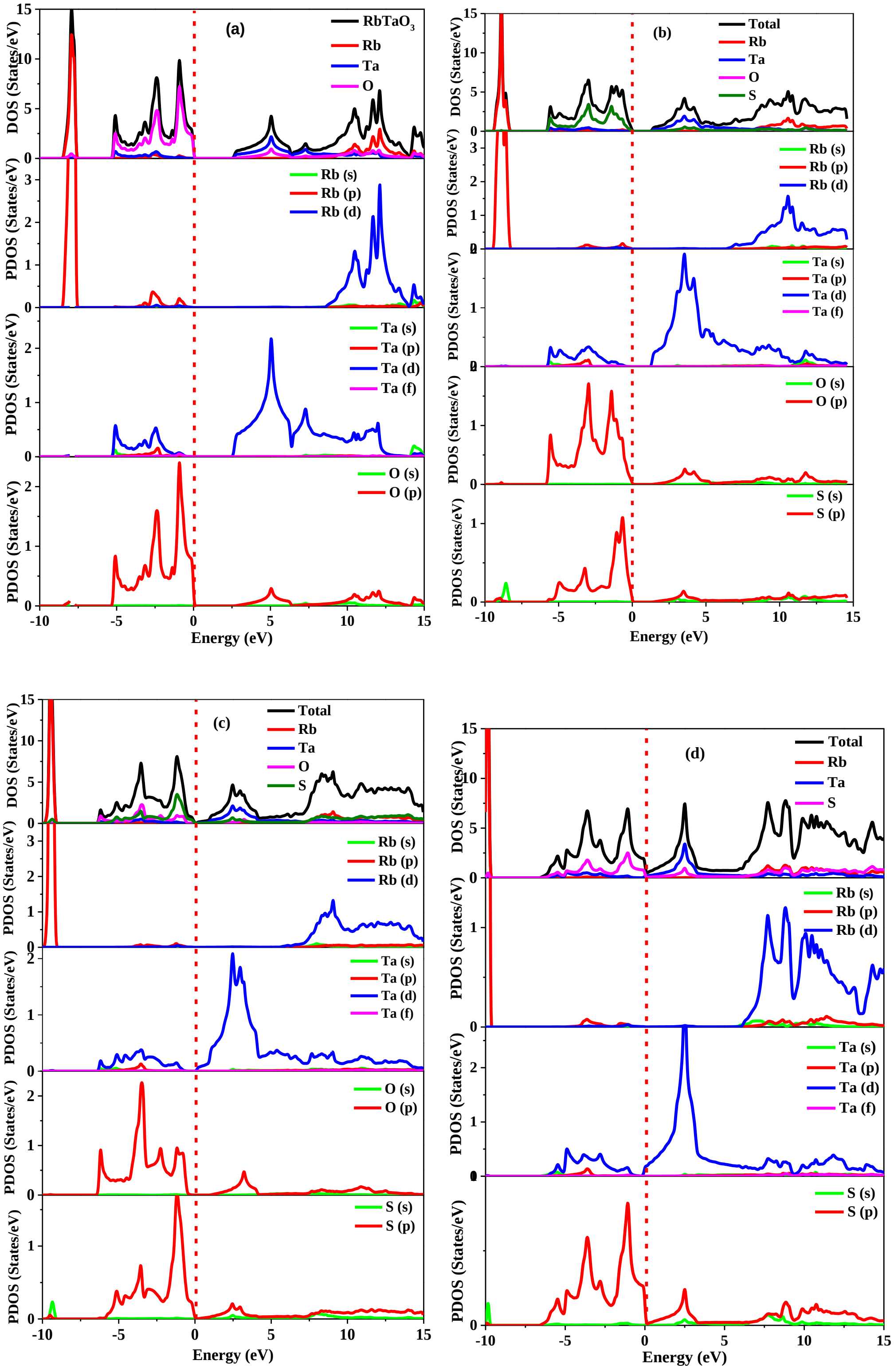

Fig. 4.12: Density of states (DOS) of (a) $RbTaO_3$, (b) $RbTaO_2S$, (c) $RbTaOS_2$, and (d) $RbTaS_3$ compounds.

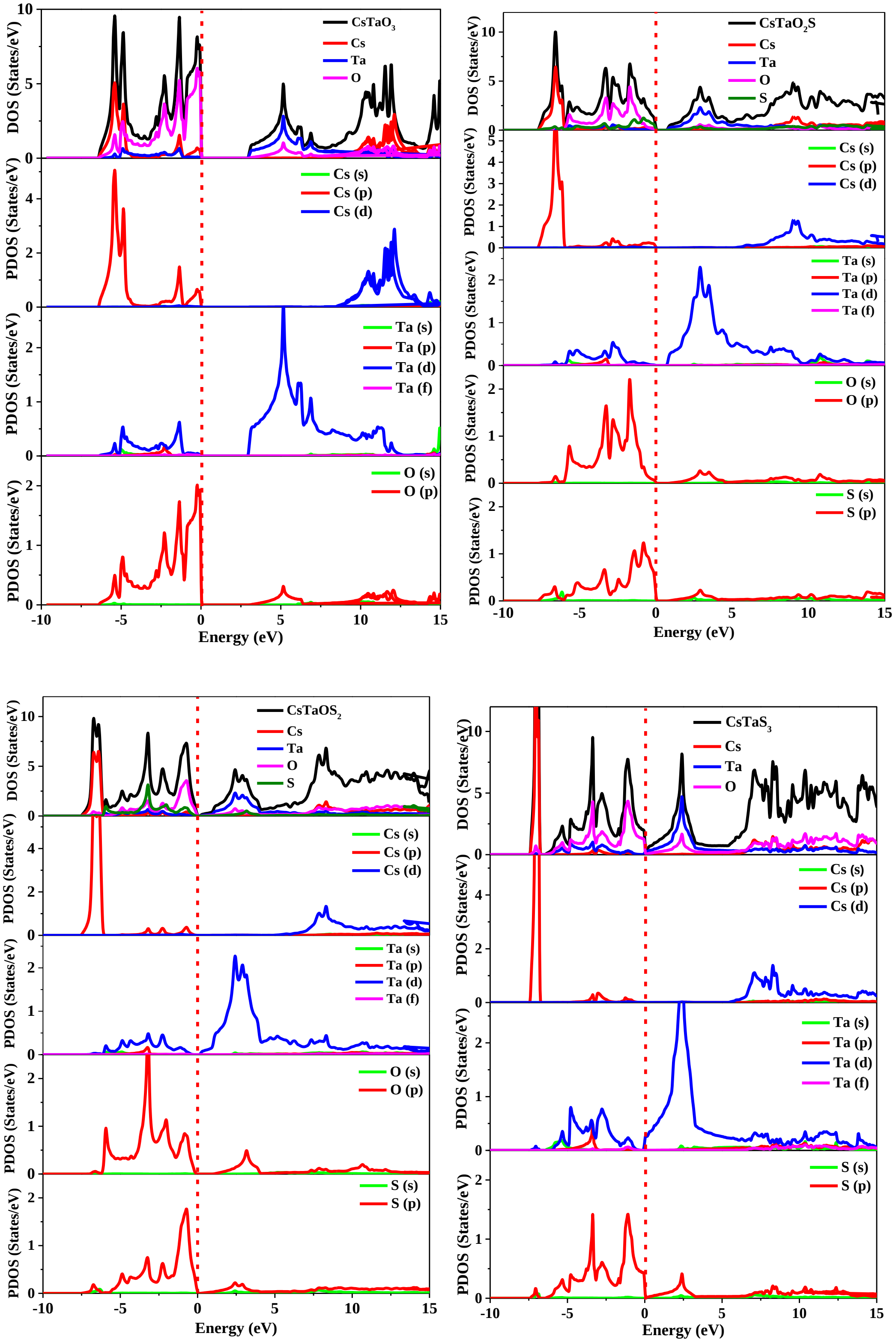

Fig. 4.13: Density of states (DOS) of (a) $CsTaO_3$, (b) $CsTaO_2S$, (c) $CsTaOS_2$, and (d) $CsTaS_3$ compounds.

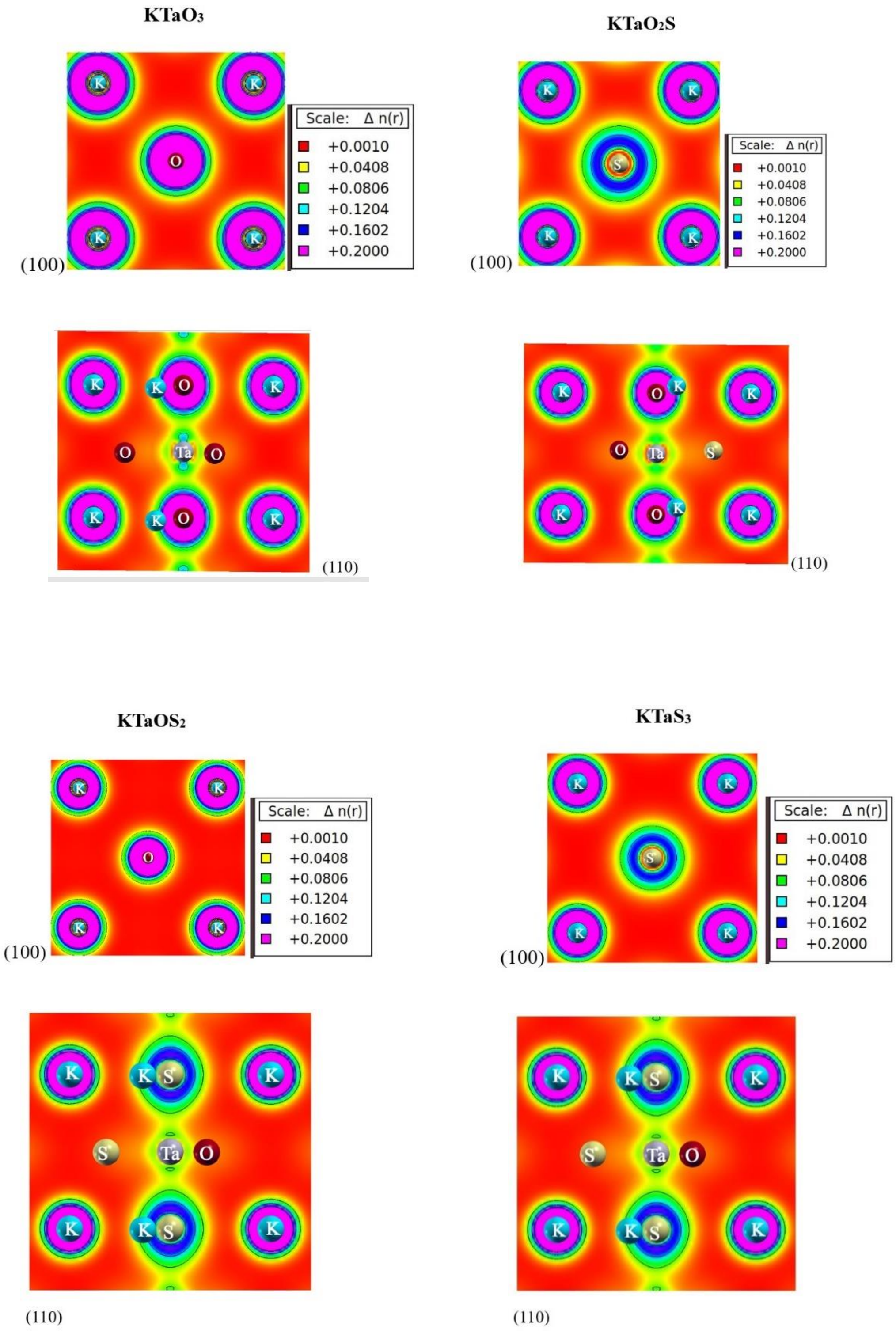

Figure 4.14: Charge density mapping of $KTaO_{3-x}S_x$ compounds.

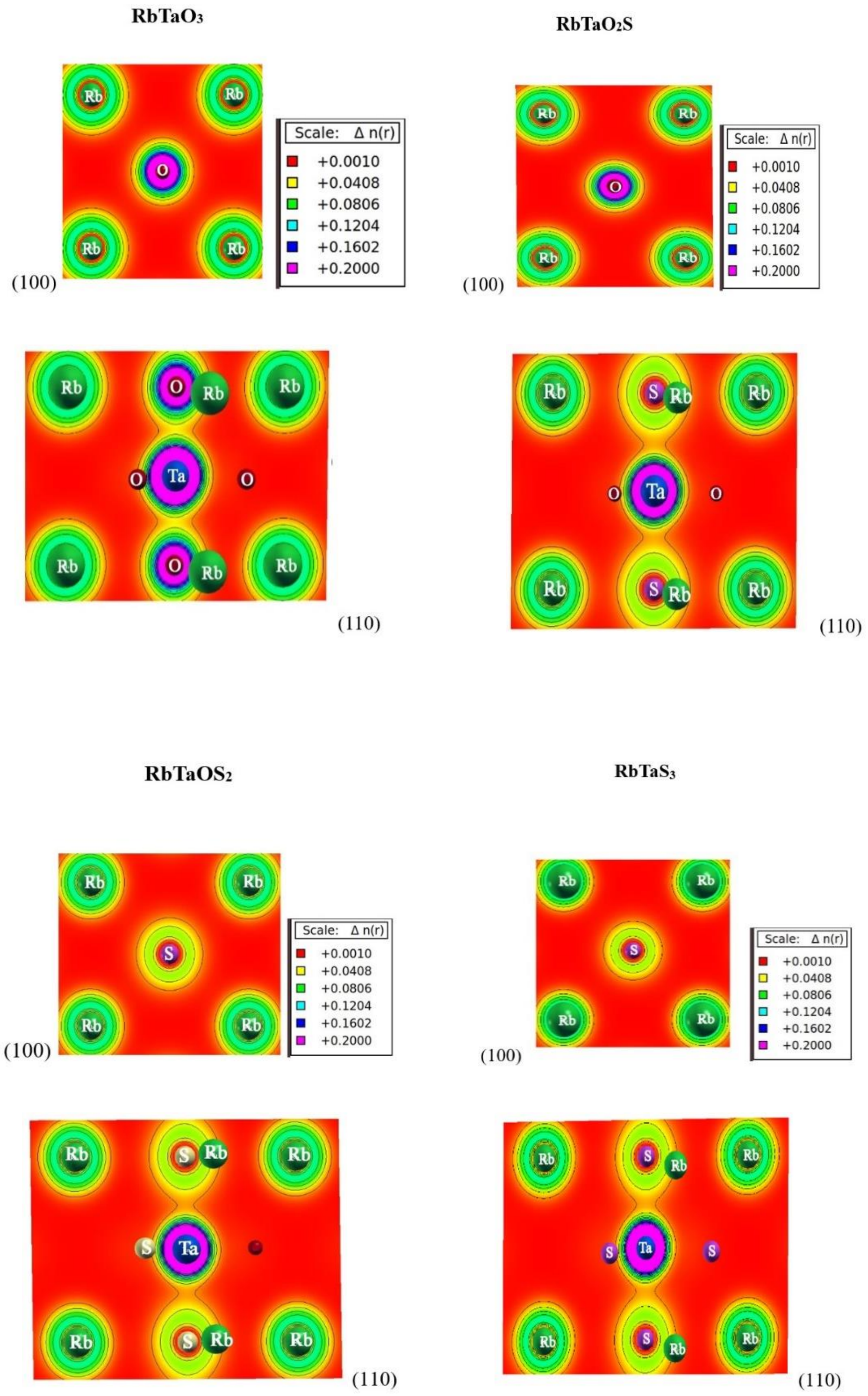

Figure 4.15: Charge density mapping of $RbTaO_{3-x}S_x$ compounds.

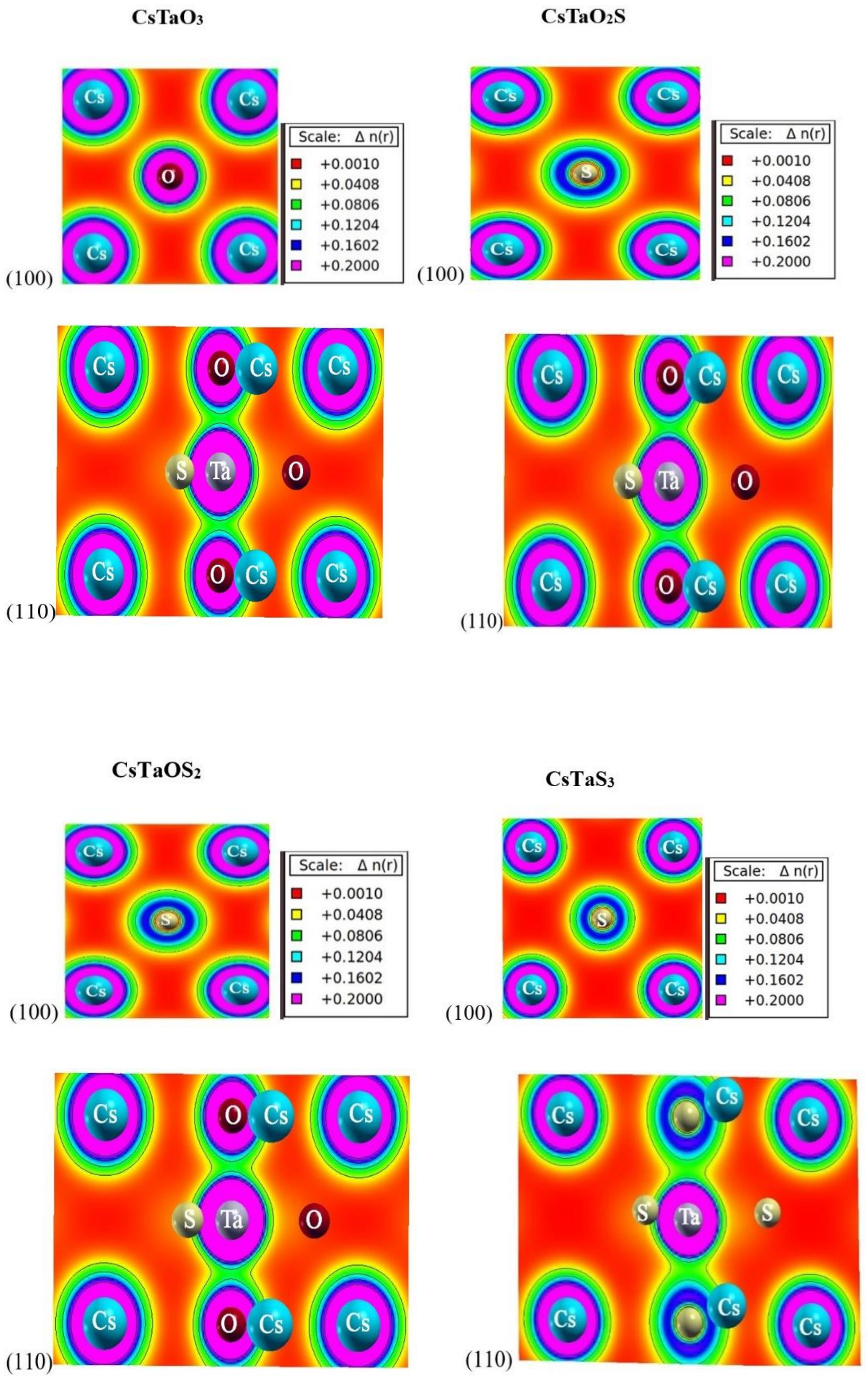

CsTaO$_3$

CsTaO$_2$S

CsTaOS$_2$

CsTaS$_3$

Figure 4.16: Charge density mapping of CsTaO$_{3-x}$S$_x$ compounds.

4.4 Optical Properties

This section delves into the impact of sulfur substitution on the optical properties of perovskite semiconductors, specifically $ATaO_{3-x}S_x$. Optical constants such as the dielectric function (ε), absorption coefficient (α), reflectivity (R), loss function (L), refractive index (n), and extinction coefficient (k) are pivotal in comprehending semiconductor nature. Determining these constants is crucial for exploring the optical characteristics essential for various applications. It's noteworthy that the optical properties of the two tetragonal phases, $ATaO_2S$ and $ATaOS_2$, are notably influenced by the phase transition from cubic to tetragonal symmetry. Additionally, these properties exhibit differences between the xx and zz directions due to the symmetry alteration. Therefore, the impact of S substitution on the optical properties of semiconductors must be carefully examined in both directions to understand their properties better. Comparing the optical properties calculated via unit cell and supercell, we find that all results are in excellent agreement with supercell and unit cell.

4.4.1. Dielectric Function

The dielectric constant (ε) is a fundamental property that reveals a material's response to an electric field. In this study, $\varepsilon_1(0)$ signifies the material's capacity to store electric energy at zero frequency, reflecting its intrinsic polarizability. Conversely, $\varepsilon_2(\omega)$ characterizes the material's absorption of electromagnetic energy, with peaks indicating electronic transitions between energy bands. This knowledge is crucial for comprehending the optical and electronic characteristics of materials, shaping their applications across various technological fields. The calculated real ($\varepsilon_1(\omega)$) and imaginary ($\varepsilon_2(\omega)$) parts of the dielectric function For $ATaO_{3-x}S_x$ are presented in Fig. 4.17, 4.18, and 4.19 in the energy range of 0-25 eV. The static real dielectric constants ($\varepsilon_1(0)$) are presented in Table 3.

Notable peaks in the spectra of ε_{1max} are presented in Table 3. Generally, negative real dielectric tensors indicate inadequate light transmission through the material and high reflection [22]. All these compounds exhibit negative values again after the 20 eV energy range; in this particular energy range, the materials behave like metals [23,24].

The imaginary part of the dielectric function tensor, $\varepsilon_2(\omega)$, is shown in Fig. 4.17(b), 4.18(b), and 4.19(b). It is notable from the figures that the static $\varepsilon_2(0)$ increases with the band gap energy; this is closely associated with the band structure. Hence, it remains zero until the band gap energies of these phases are reached. The spectra of $\varepsilon_2(\omega)$, shown in Figure 4.17(b), reveal maximum values of all calculated compounds are presented in Table 4.3. These compounds exhibit a wide range of absorption spectra, making them suitable for various optical applications.

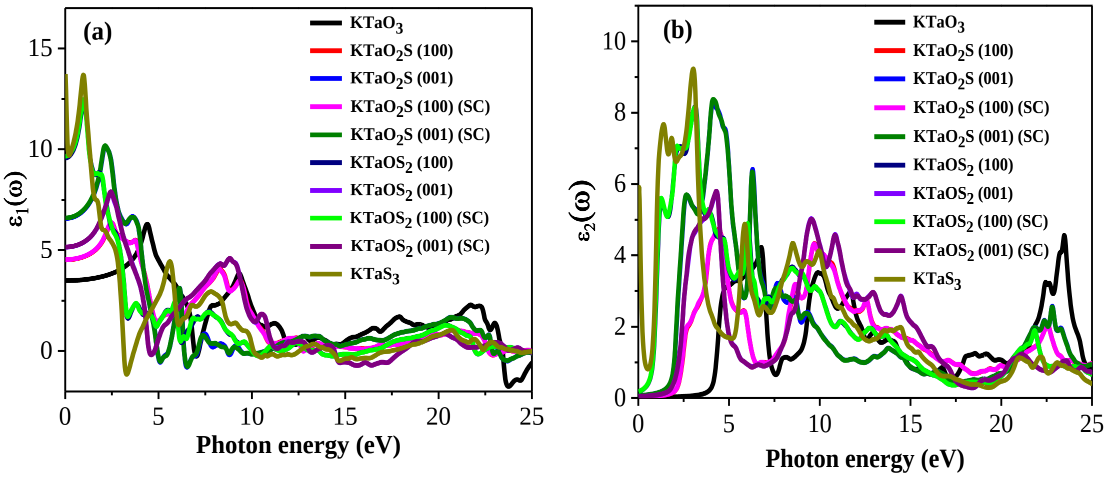

Fig. 4.17: The calculated (a) real part of dielectric constant and (b) imaginary part of dielectric constant of $KTaO_{3-x}S_x$ compounds.

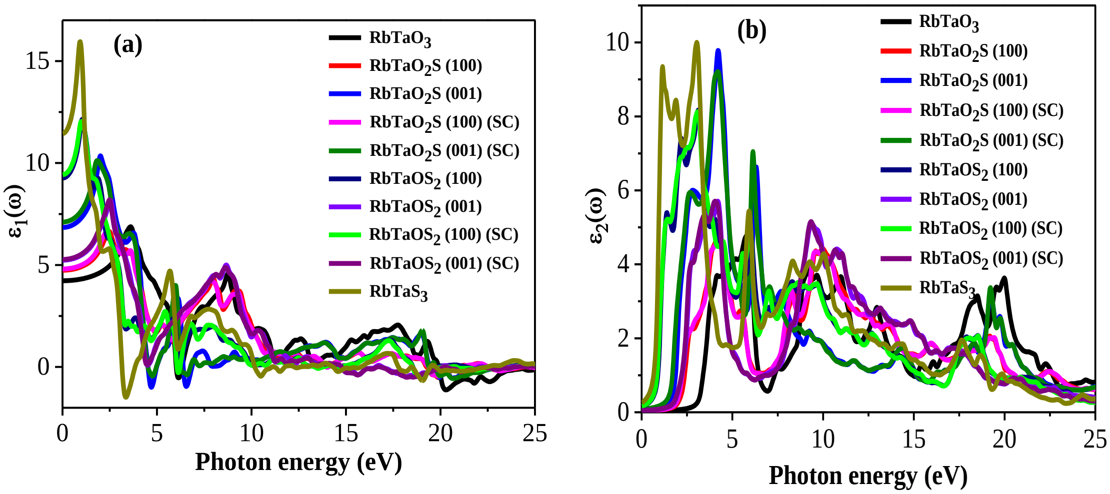

Fig. 4.18: The calculated (a) real part of dielectric constant, (b) imaginary part of dielectric constant of $RbTaO_{3-x}S_x$ compounds.

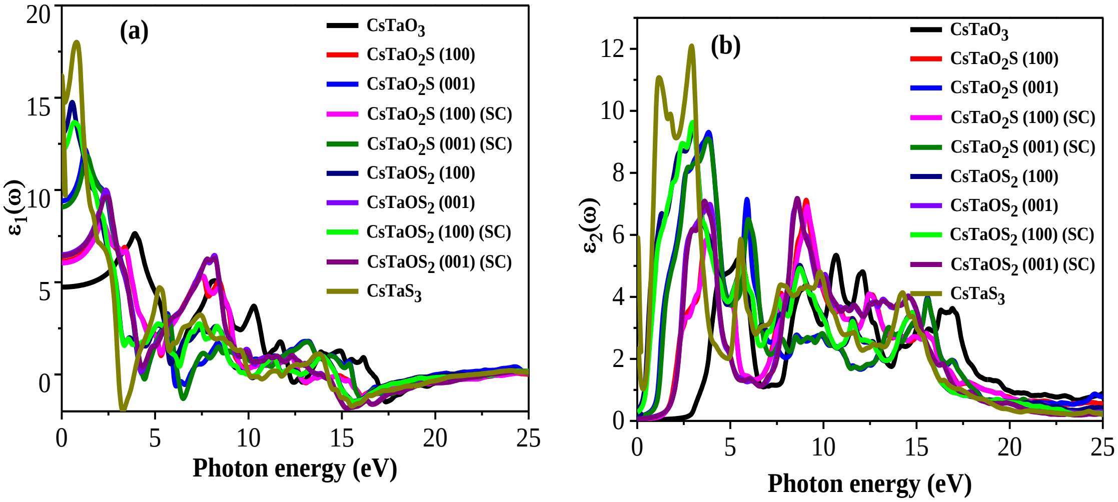

Fig. 4.19: The calculated (a) real part of dielectric constant, (b) imaginary part of dielectric constant of $CsTaO_{3-x}S_x$ compounds.

4.4.2 Absorption Coefficient

The absorption coefficient α(ω) is closely related to the dielectric function [25]. The plasmon frequency is related to the energy loss function. The correlation between frequency and incident light is responsible for plasma resonance. The investigated and other semiconductor materials exhibit zero value for α(ω) within the energy band gap.

The absorption coefficient α(ω) in all of the studied compounds is found to be 10^5-10^6 cm $^{-1}$ at their respective absorption edges, which occur at 3.5 eV, 2.2 eV, 1.7 eV, 0.3 eV, 0.5 eV, and 0.4 eV for $KTaO_3$, $KTaO_2S$ [100], $KTaO_2S$ [001], $KTaOS_2$ [100], $KTaOS_2$ [001], and $KTaS_3$, respectively. The absorption edges, as shown in Fig. 4.20(b), are 2.7 eV, 1.6 eV, 1.4 eV, 1.7 eV, 0.7 eV, and 0.4 eV for $RbTaO_3$, $RbTaO_2S$ [100], $RbTaO_2S$ [001], $RbTaOS_2$ [100], $RbTaOS_2$ [001], and $RbTaS_3$, respectively.

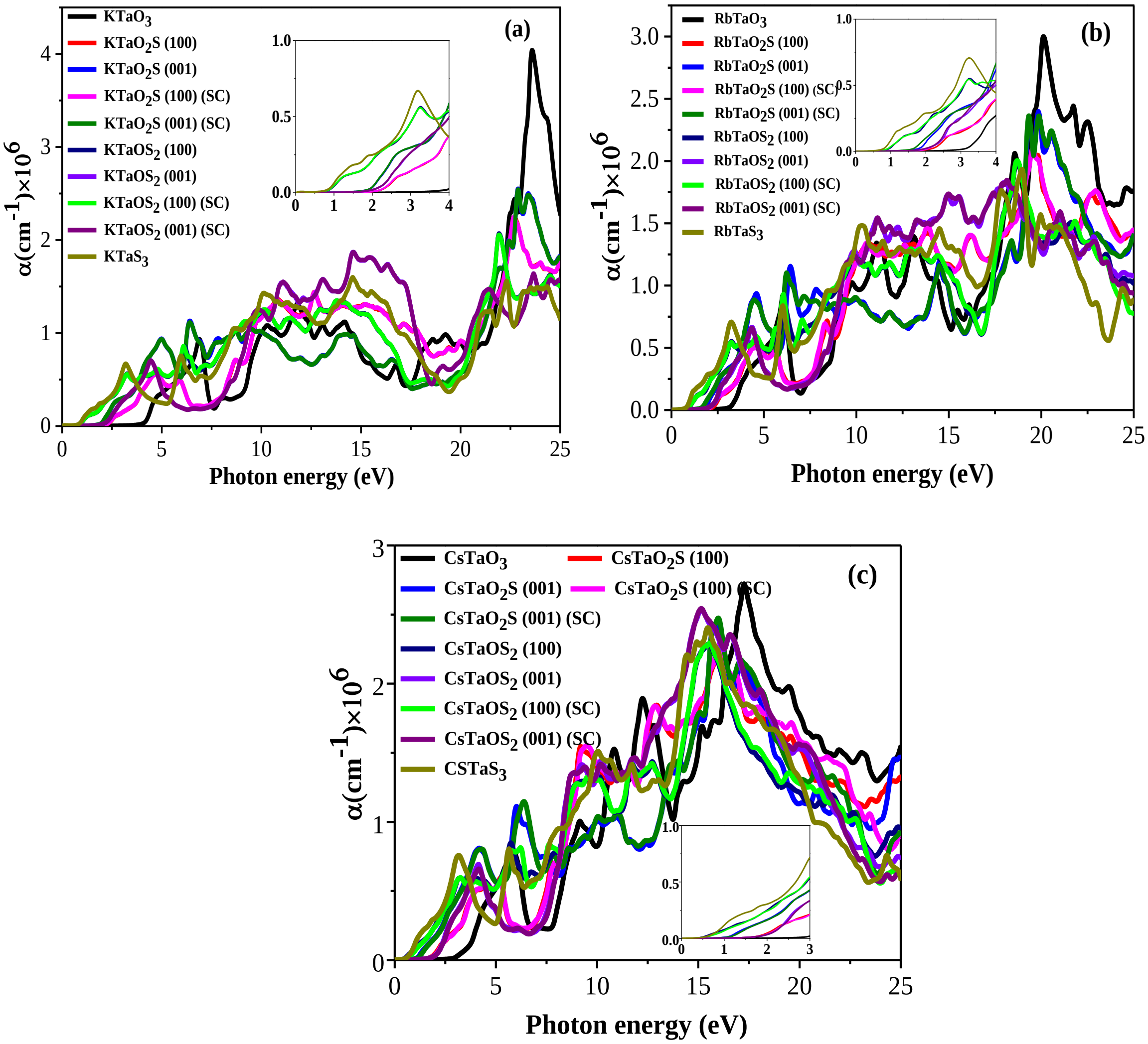

Fig. 4.20: The calculated absorption coefficient of (a) $KTaO_{3-x}S_x$, (b) $RbTaO_{3-x}S_x$, and (c) $CsTaO_{3-x}S_x$ compounds.

Figure 4.20(c) shows absorption edges occurred at 2.8 eV, 1.8 eV, 1.1 eV, 0.4 eV, 0.8 eV, 0.2 eV for $CsTaO_3$, $CsTaO_2S$ [100], $CsTaO_2S$ [001], $CsTaOS_2$ [100], $CsTaOS_2$ [001], and $CsTaS_3$, respectively. Therefore, both the cubic and tetragonal phases demonstrate remarkable efficiency in absorbing visible and ultraviolet light. The absorption coefficient of $KTaO_2S$ and $RbTaO_2S$ displays a notable peak, comparable to highly efficient solar cell perovskite materials like $CsPbI_3$, $CH_3NH_3PbCl_3$, and $MAPbCl_3$. This positions $KTaO_2S$ and $RbTaO_2S$ as highly promising candidates for high-performance solar cell applications [26–28].

4.4.3 Optical Reflectivity

Figure 4.21 depicts the optical reflectivity values for $KTaO_{3-x}S_x$ compounds. The static reflectivity values are as follows: 9% for KTaO3, 12% for $KTaO_2S$ [100], 19% for $KTaO_2S$ [001], 26% for $KTaOS_2$ [100], 15% for $KTaOS_2$ [001], and 35% for $KTaS_3$. And 12%, 13%, 20%, 25%, 15%, and 29% for $RbTaO_3$, $RbTaO_2S$ [100], $RbTaO_2S$ [001], $RbTaOS_2$ [100], $RbTaOS_2$ [001], and $RbTaS_3$, respectively. Furthermore, $CsTaO_{3-x}S_x$ reflects 13% for $CsTaO_3$, 18% for $CsTaO_2S$ [100], 26% for $CsTaO_2S$ [001], 32% for $CsTaOS_2$ [100], 19% for $CsTaOS_2$ [001], and 36% for $CsTaS_3$ respectively. The reflectivity is poor – implying that these materials have the potential to be used as anti-reflection coatings. The study found that the optical properties of $KTaO_2S$ and $RbTaO_2S$ are comparable to those of $CsPbI_3$ [29] along with their band gap values, which makes it a promising material for optoelectronic applications, such as solar cells. The results suggest that solar cell technology can utilize the calculated compounds.

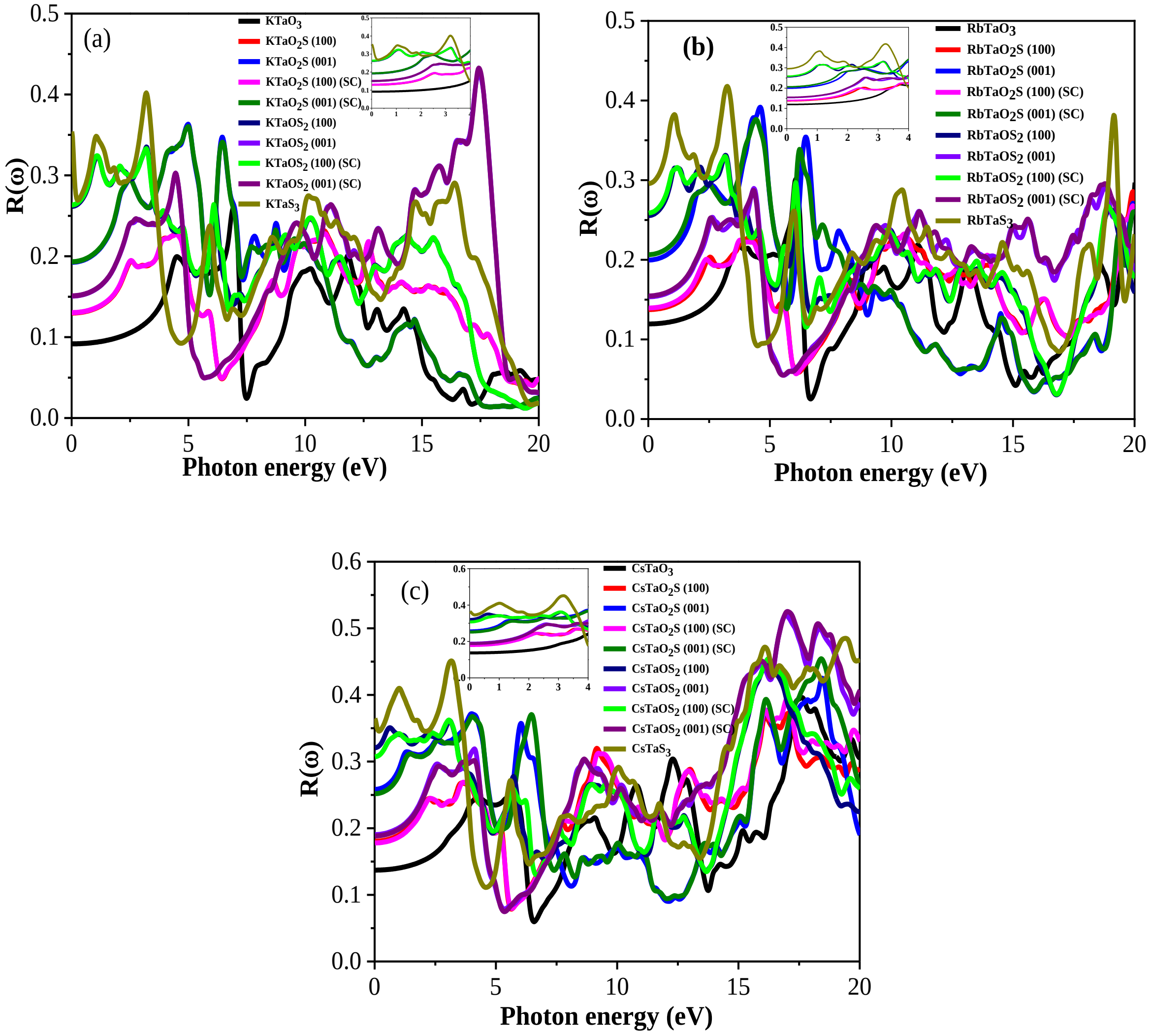

Fig. 4.21: The calculated Reflectivity of (a) KTaO$_{3-x}$S$_x$, (b) RbTaO$_{3-x}$S$_x$, and (c) CsTaO$_{3-x}$S$_x$ compounds.

4.4.4 Loss Function

The energy loss function L(ω) describes the dissipation of energy within the compound due to interactions between electrons and photoelectrons, which are attributed to plasma losses [30]. Fig. 4.22 shows the energy loss functions for ATaO$_{3-x}$S$_x$ compounds. All calculated compounds' energy loss begins at around 1 to 4 eV. With increased photon energy, the optical energy loss gradually increases and reaches its highest peak for $ATaS_3$. Of all the compounds studied, $ATaO_3$ shows the least electron loss in the higher energy range compared to the others.

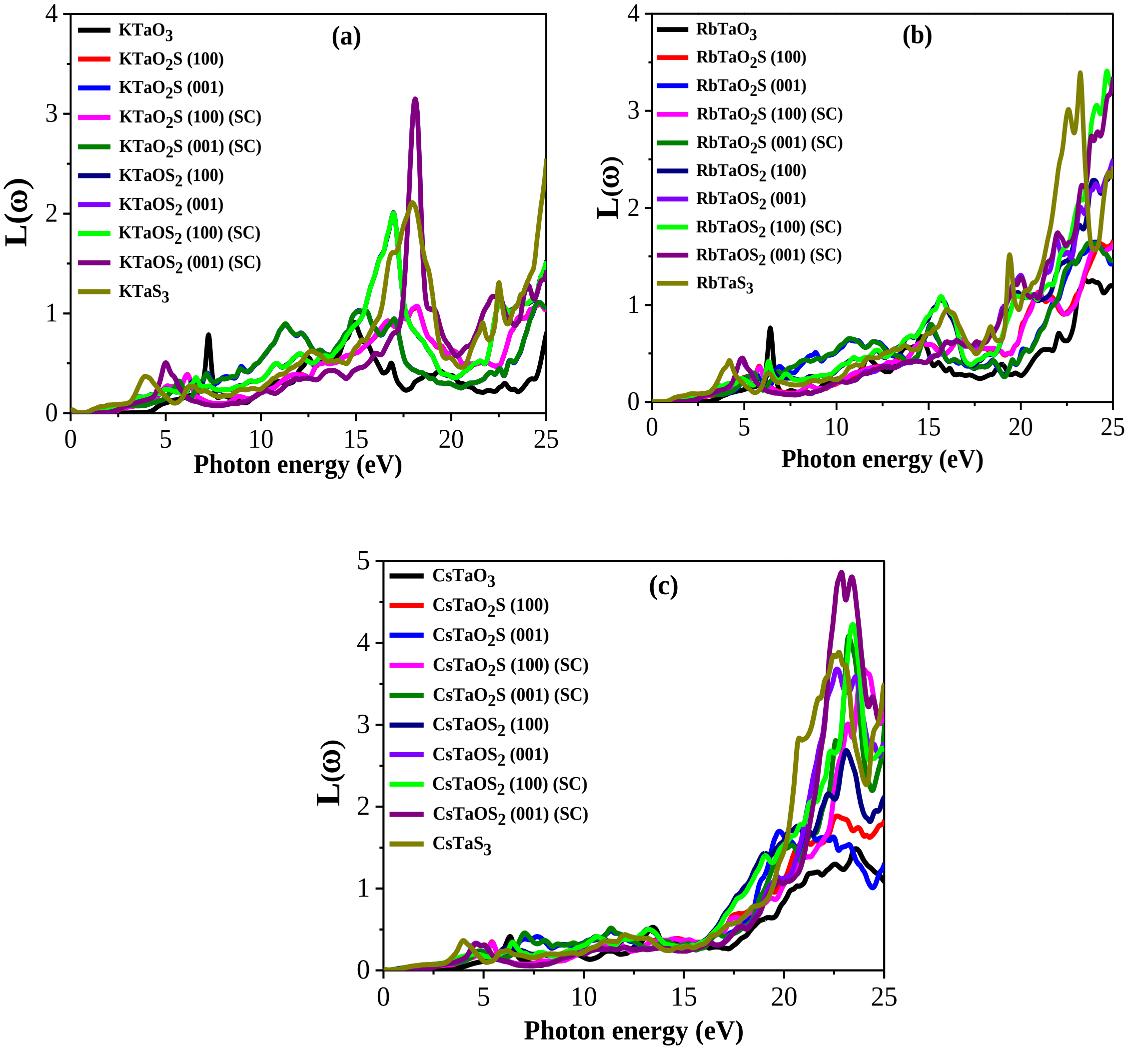

Fig. 4.22: The calculated loss function of (a) $KTaO_{3-x}S_x$, (b) $RbTaO_{3-x}S_x$, and (c) $CsTaO_{3-x}S_x$ compounds.

4.4.5 Optical Conductivity

The optical conductivity of a solid quantifies the extent of electron transport influenced by light and correlates directly with the refractive index and absorption coefficient. In all cases examined here, it is observed that the optical conductivity is zero at the energy band gap, consistent with expectations. Beyond the threshold frequency, a noticeable rise in optical conductivity is observed, with initial peaks occurring at 6.75 eV, 4.51 eV, 4.84 eV, 3.21 eV, 4.34 eV, and 3.09 eV for $KTaO_3$, $KTaO_2S$ [100], $KTaO_2S$ [001], $KTaOS_2$ [100], $KTaOS_2$ [001], and $KTaS_3$, respectively. Upon surpassing the threshold frequency, optical conductivity increases to values of 3.37, 2.48, 5.02, 3.12, 2.98, and 3.73 for $RbTaO_3$, $RbTaO_2S$ [100], $RbTaO_2S$ [001], $RbTaOS_2$ [100], $RbTaOS_2$ [001], and $RbTaS_3$, respectively, marking the onset of the first peak. And 3.4, 2.8, 4.39, 3.5, 3.3 and 4.31 for $CsTaO_3$, $CsTaO_2S$ [100], $CsTaO_2S$ [001], $CsTaOS_2$ [100], $CsTaOS_2$ [001], and $CsTaS_3$ respectively, as the first peak.

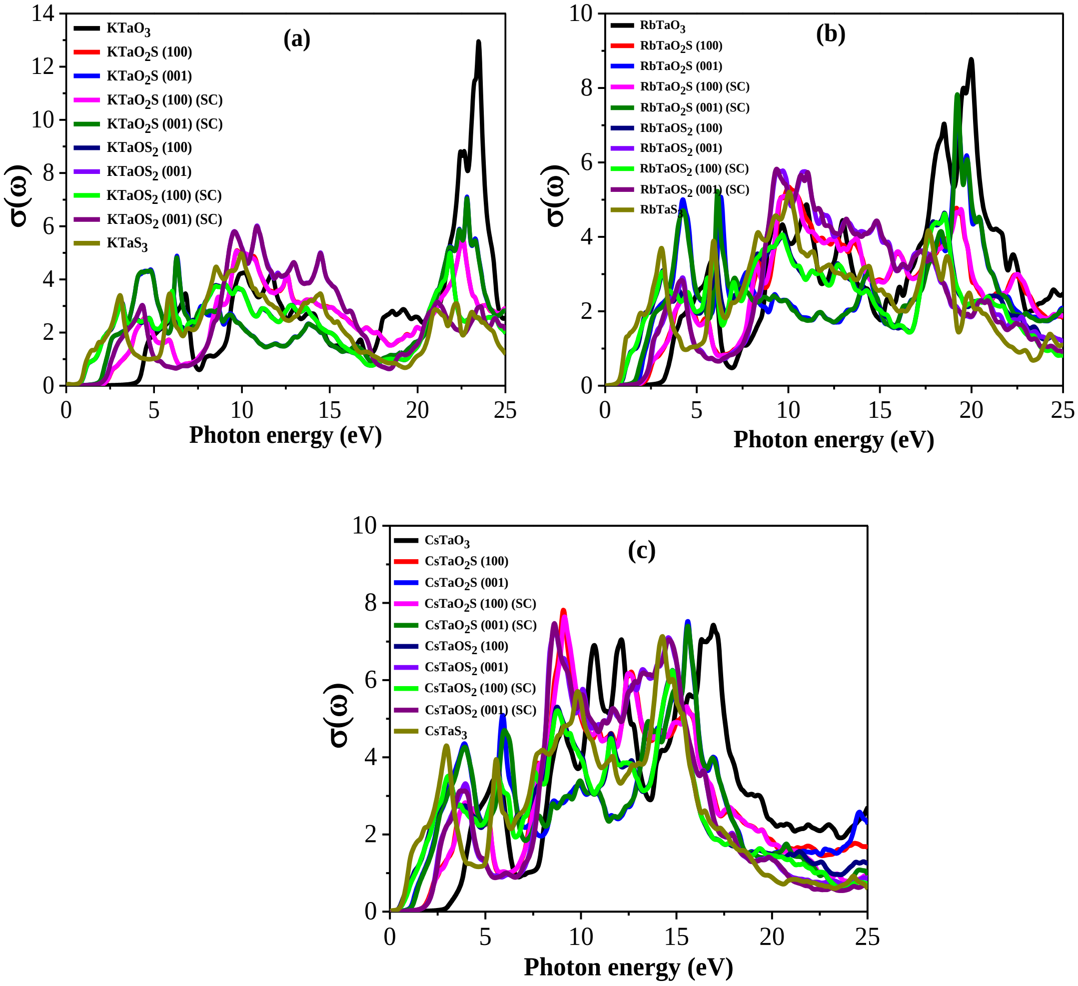

Fig. 4.23: Calculated optical conductivity of (a) $KTaO_{3-x}S_x$, (b) $RbTaO_{3-x}S_x$, and (c) $CsTaO_{3-x}S_x$.

Afterward, the optical conductivity decreases abruptly around the energy range of 4-8 eV for all the compounds, which is associated with the plasmon frequency. The optical conductivity reaches peaks, which are presented in Table 4.3.

4.4.6 Reflective index and extinction coefficient

The extinction coefficient k(ω) and refractive index n(ω) of a material represent its capacity to absorb incident photons and its velocity, respectively. The refractive index (n(ω)) of $ATaO_3$-xS_x, as illustrated in Figure 4.24, exhibits a notable similarity in trend across various energy ranges to the real dielectric tensor.

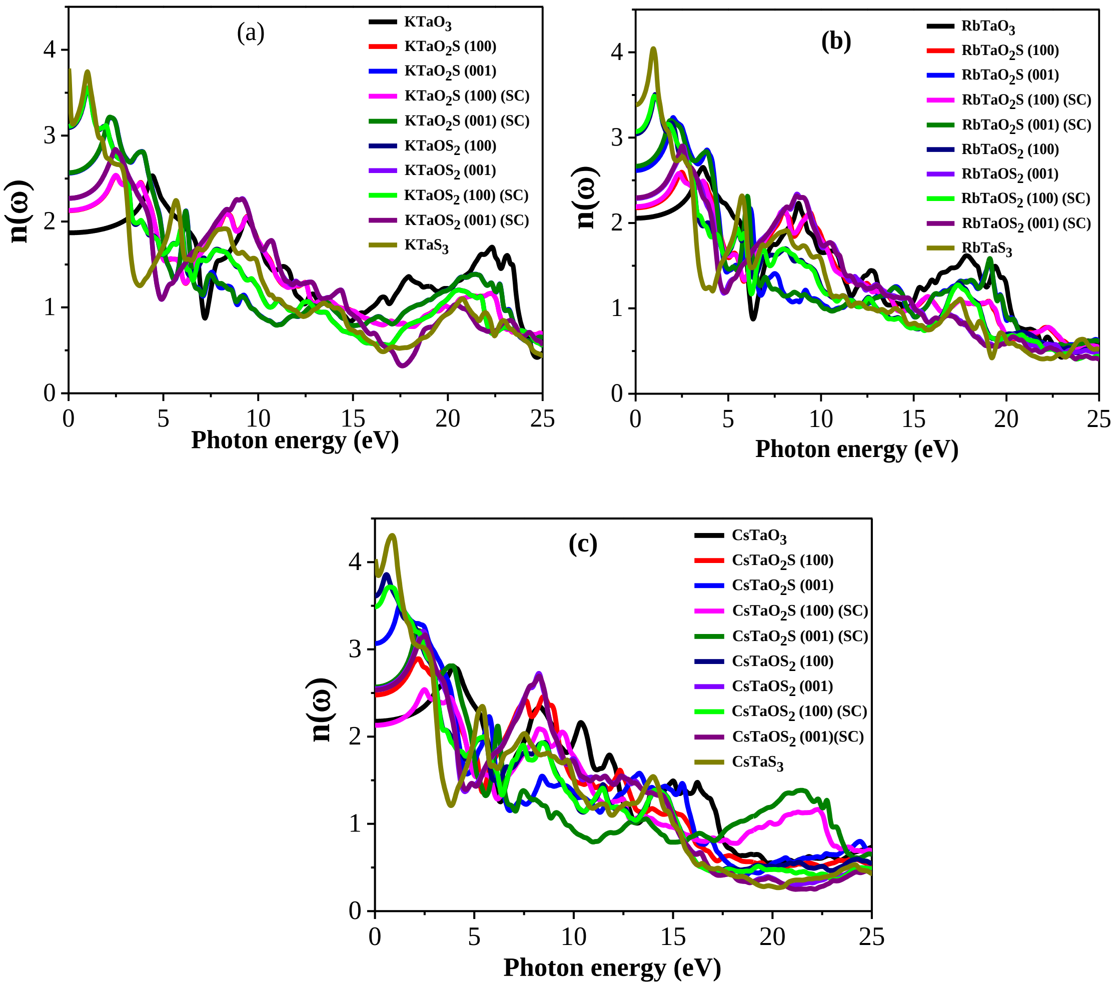

Figure 4.24: Refractive index of (a) $KTaO_{3-x}S_x$, (b) $RbTaO_{3-x}S_x$, and (c) $CsTaO_{3-x}S_x$ compounds.

This observation underscores the intimate connection between the optical properties and electronic structure of materials. Notably, the calculated values for the static point n(0) are meticulously documented in Table 4.3, provides perspective into the material's behavior under specific conditions. Semiconductor materials with wide band gaps generally possess a lower refractive index value at static points.

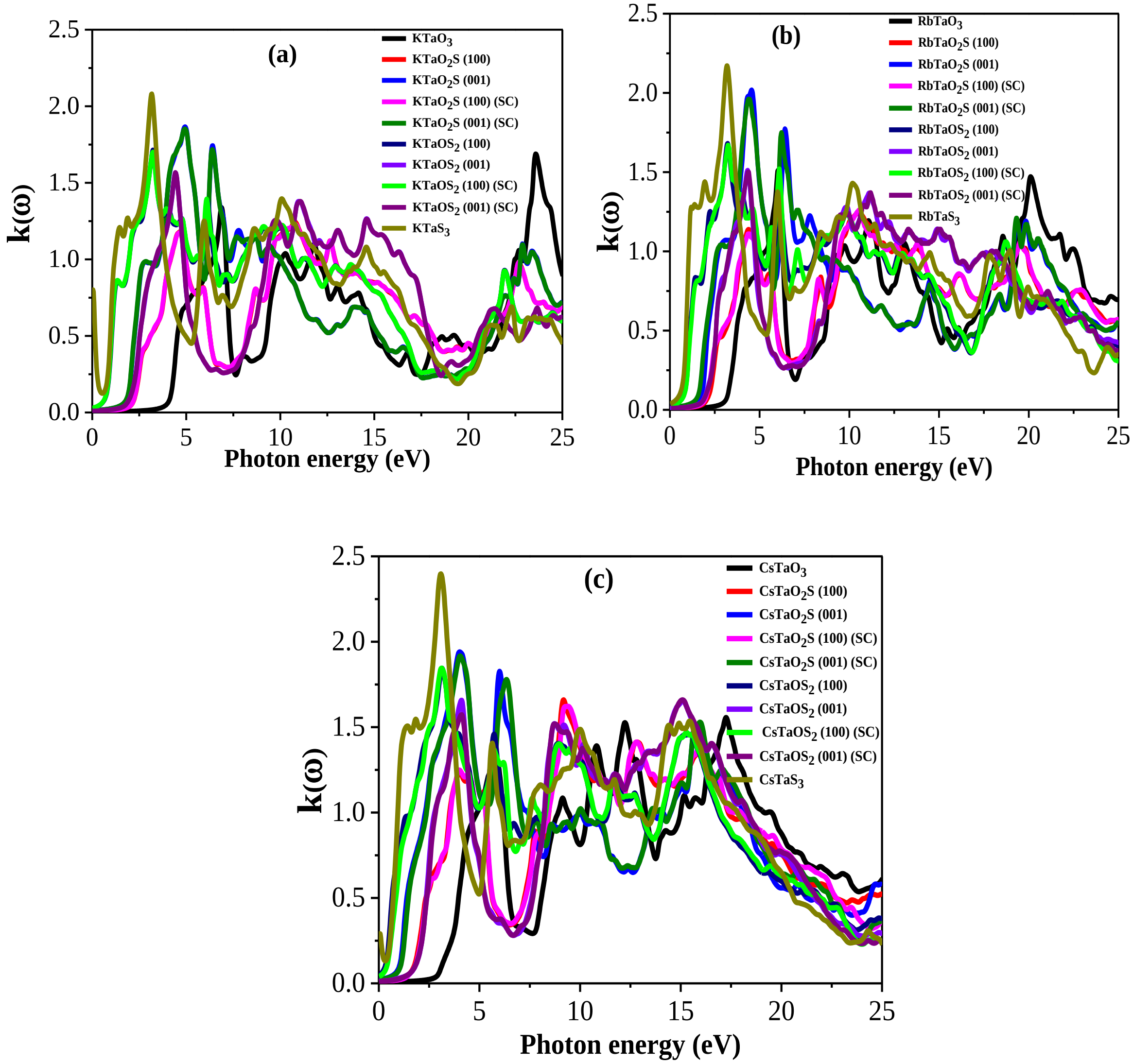

Fig. 4.25: Calculated extinction coefficient of (a) $KTaO_{3-x}S_x$, (b) $RbTaO_{3-x}S_x$, and (c) $CsTaO_{3-x}S_x$ compounds.

Table 4.3: The calculated optical parameters of perovskite $ATaO_{3-x}S_X$ compounds.

phases	$\boldsymbol{\varepsilon_1(0)}$	$\boldsymbol{\varepsilon_{1max}(eV)}$	$\boldsymbol{\varepsilon_{2max}(eV)}$	$\boldsymbol{R(0)}$	$\boldsymbol{n\ (0)}$	$\boldsymbol{\sigma_{max}(eV)}$
$KTaO_3$	3.48	4.39	6.81	0.09	1.87	23.05
$RbTaO_3$	4.23	3.56	4.85	0.12	2.07	19.90
$CsTaO_3$	4.79	3.92	10.37	0.13	2.16	16.93
$KTaO_2S$ (100)	4.54	4.42	4.42	0.12	2.12	22.66
$KTaO_2S$ (001)	6.58	4.05	4.13	0.19	2.55	22.75
$RbTaO_2S$ (100)	4.61	2.52	5.85	0.13	2.16	10.04
$RbTaO_2S$ (001)	6.79	1.23	4.76	0.20	2.37	19.21
$CsTaO_2S$ (100)	6.15	2.27	9.09	0.18	2.47	9.07
$CsTaO_2S$ (100)	9.40	1.38	3.80	0.26	3.06	15.58
$KTaOS_2$ (100)	9.56	3.09	3.02	0.26	3.09	21.87
$KTaOS_2$ (001)	5.10	4.34	4.32	0.14	2.28	10.88
$RbTaOS_2$ (100)	9.21	1.17	3.13	0.25	3.05	18.56
$RbTaOS_2$ (001)	5.23	0.87	4.19	0.15	2.31	9.54
$CsTaOS_2$ (100)	13.01	0.57	2.93	0.32	3.62	14.75
$CsTaOS_2$ (001)	6.53	2.37	4.23	0.19	2.53	8.62
$KTaS_3$	13.73	3.05	3.01	0.35	3.78	5.04
$RbTaS_3$	11.42	0.91	3.03	0.29	3.38	10.10
$CsTaS_3$	16.11	0.79	2.92	0.36	3.04	14.26

This precisely agrees with our calculated result, where $ATaO_3$ has the highest band gap and the lowest refractive index. Similarly, the band gap of $ATaS_3$ is the lowest, and its n(ω) is the highest among the studied compositions. Fig. 4.25 shows the plot of the extinction coefficient. The k(ω) values for $ATaO_{3-x}S_x$ remain at 0 within the energy band gap range. As the light frequency exceeds the energy band gap, the maximum values for all compounds reach approximately 3 eV to 8 eV. However, in the [100] directions of $KTaO_2S$, $RbTaO_2S$, and $CsTaO_2S$, the maximum peak is observed at 10.8 eV, 10.5 eV, and 9.2 eV, respectively. The spectra of k(ω) closely mirror the imaginary dielectric tensor $\varepsilon_2(\omega)$ as depicted in the figure.

4.5 Mechanical Properties

The elastic properties of solids encompass the material's capacity for deformation under various stresses and revert to its initial form upon stress removal. Exploring elastic properties provides reliable insights into a material's mechanical traits, including stability, strength, ductility/brittleness, Young's modulus (Y), bulk modulus (B), shear modulus (G), anisotropy factor, and other elastic parameters. [31].

Our investigation into mechanical characteristics commenced by employing the strain-stress approach to calculate independent elastic constants. These elastic constants, along with Hill's approximation, were utilized to determine the average values of elastic moduli's upper and lower limits for polycrystalline materials [32]. Subsequently, both elastic moduli and elastic constants were employed to estimate fracture toughness, ductility or brittleness, and anisotropic characteristics of the perovskite systems under discussion. The calculated elastic moduli with unit cell and supercell exhibit almost similar results, which confirms the calculation accuracy. The obtained elastic constants of $ATaO_{3-x}S_x$ are shown in Table 4.4. The results obtained for $ATaO_3$ and $ATaS_3$ satisfy three fundamental criteria widely accepted for evaluating the elastic stability of cubic crystals, proving the mechanical stability of these compounds. For tetragonal crystals, the capacity to withstand linear compression is assessed by C_{11} along the x-axis and C_{33} along the z-axis [33].

Table 4.4: Calculated stiffness constants (GPa) of $ATaO_{3-x}S_x$ compounds with cubic and tetragonal structures.

Compound	C_{11}	C_{12}	C_{13}	C_{44}	C_{33}	C_{66}
$KTaO_3$	366	71	-	107	-	-
$RbTaO_3$	406	76	-	111	-	-
$CsTaO_3$	383	54	-	118	-	-
$KTaO_2S$	280	76	42	55	258	100
$KTaO_2S$ (SC)	279	77	39	53	259	98
$RbTaO_2S$	241	91	43	56	262	111
$RbTaO_2S$ (SC)	252	95	37	58	266	112
$CsTaO_2S$	292	82	47	61	251	125
$CsTaO_2S$ (SC)	228	114	38	59	252	122
$KTaOS_2$	198	37	38	55	219	37
$KTaOS_2$ (SC)	197	40	38	53	219	35
$RbTaOS_2$	184	19	30	62	197	36
$RbTaOS_2$ (SC)	177	31	36	60	203	35
$CsTaOS_2$	185	25	25	69	159	34
CsTaOS2 (SC)	204	45	77	68	208	36
$KTaS_3$	198	52	-	49	-	-
$RbTaS_3$	226	44	-	44	-	-
$CsTaS_3$	157	42	-	48	-	-

Table 4.5: Computed bulk modulus *B* (GPa), Young's modulus *Y* (GPa), shear modulus *G* (GPa), Pugh's ratio (*B/G*), Poisson's ratio *ν* and machinability index *B*/*C*$_{44}$ for $ATaO_{3-x}S_x$ compounds.

Compound	*B*	*G*	*Y*	*B*/*G*	*ν*	*B*/*C*$_{44}$
$KTaO_3$	169	121	294	1.39	0.21	1.58
$RbTaO_3$	186	130	316	1.43	0.22	1.68
$CsTaO_3$	164	135	318	1.21	0.18	1.38
$KTaO_2S$	126	81	201	1.55	0.23	2.30
KTaO2S (SC)	124	80	198	1.55	0.23	2.33
$RbTaO_2S$	122	79	194	1.55	0.23	2.17
$RbTaO_2S$ (SC)	123	82	201	1.50	0.23	2.11
$CsTaO_2S$	131	89	217	1.47	0.22	2.15
$CsTaO_2S$ (SC)	120	78	192	1.55	0.23	2.05
$KTaOS_2$	93	60	148	1.56	0.24	1.69
KTaOS2 (SC)	94	58	145	1.61	0.24	1.79
$RbTaOS_2$	81	62	148	1.30	0.19	1.29
$RbTaOS_2$ (SC)	89	59	146	1.50	0.23	1.49
$CsTaOS_2$	75	62	146	1.21	0.18	1.08
$CsTaOS_2$ (SC)	112	60	152	1.59	0.27	1.62
$KTaS_3$	101	57	144	1.76	0.26	2.07
$RbTaS_3$	104	59	150	1.76	0.26	2.35
$CsTaS_3$	80	52	128	1.55	0.23	1.66

We can see that the elastic constants are all positive, C_{11} is larger than C_{12}, and $2C_{13}$ is smaller than $C_{11}+C_{33}$, thereby indicating that these $ATaO_{3-x}S_x$ compounds meet the mechanical stability criterion and these compounds are mechanically stable. Table 4.4 displays the calculated values, demonstrating their mechanical stability. Notably, our results exhibit a significant concurrence with previously calculated values, thereby substantiating the accuracy of our calculations [2,13].

Young's modulus (Y), bulk modulus (B), and shear modulus (G) are indicators of the hardness and stiffness of materials. Among the elastic constants, C_{44} is considered the most reliable predictor of solid hardness [34]. In our analysis, we observe that the shear moduli of $ATaO_3$, reflecting the material's hardness, exhibit larger bulk values. Additionally, higher Young's modulus values contribute to increased stiffness. Table 4.5 demonstrates that upon substituting S for O, the elastic moduli of $ATaO_2S$, $ATaOS_2$, and $ATaS_3$ decrease in comparison to $ATaO_3$.

Pugh's B/G ratio helps to categorize the brittle and ductile class of solids. The ratio $B/G > 1.75$ indicates that the material is ductile; otherwise, ($B/G < 1.75$) it reveals brittleness [35]. Another significant elastic parameter is the Poisson ratio ν, which helps to confirm brittleness and ductility. If the Poisson ratio $\nu > 0.26$, according to Frantsevich's rule, it will present ductility; lower than this value suggests brittleness [36]. Table 4.5 shows that $ATaO_3$, $ATaO_2S$, and $ATaOS_2$ exhibit brittleness, while $KTaS_3$ and $RbTaO_3$ display ductile characteristics. However, $CsTaS_3$ was found to be brittle. The ratio B/C_{44} gives the machinability index an important mechanical performance indicator [37]. A material with low shear resistance and a small C_{44} value tends to have high machinability. In the case of $ATaO_2S$, it exhibits higher machinability compared to the other compounds.

4.5.1 Elastic anisotropy

Elastic anisotropy plays a crucial role in understanding a crystal's mechanical properties when subjected to mechanical stress. Numerous crystals with low symmetry display significant elastic anisotropy. Their elastic anisotropic behaviors were investigated to determine the elastic properties of these compounds in different crystallographic directions.

Table 4.6: Calculated elastic anisotropy indices (A^U, A_B, A_G, A_1, and A_3) of $ATaO_{3-x}S_x$.

Phase	**A_1**	**A_3**	**A_B**	**A_G**	**A^U**
$KTaO_3$	-	-	-	-	0.72
$RbTaO_3$	-	-	-	-	0.67
$CsTaO_3$	-	-	-	-	0.71
$KTaO_2S$	0.49	1.01	0.40	5.40	0.57
$RbTaO_2S$	0.53	1.48	0.10	4.86	0.51
$CsTaO_2S$	0.53	1.19	0.69	5.05	0.54
$KTaOS_2$	0.64	0.58	0.12	4.75	0.50
$RbTaOS_2$	0.78	0.43	0.16	4.31	0.45
$CsTaOS_2$	0.94	0.42	0.23	4.62	0.48
$KTaS_3$	-	-	-	-	0.66
$RbTaS_3$	-	-	-	-	0.48
$CsTaS_3$	-	-	-	-	0.83

For cubic crystals, the value of 'A^U' being equal to unity implies the isotropic nature, while 'A^U' less/greater than 1 shows an anisotropic character [38]. The values of $ATaO_3$ and $ATaS_3$ that were obtained are smaller than '1', indicating the anisotropic nature.

Table 4.6 shows that the values obtained for the tetragonal compounds $ATaO_2S$ and $ATaOS_2$ exhibit an anisotropic nature. The parameters A_{100} and A_{001}, whether smaller or greater than unity, quantify the extent of anisotropy, with values equal to unity indicating completely isotropic properties. Anisotropy is indicated by non-zero values for A_B and A_G, while zero values denote the crystal's isotropy. When the universal anisotropic index (A^U) is zero, the crystal is isotropic. Any deviation from zero determines the degree of elastic anisotropy. Therefore, our obtained universal anisotropy index (A^U) for $ATaO_2S$ and $ATaOS_2$ declares that the tetragonal phase of the materials is anisotropic.

To confirm the presence of anisotropic characteristics in all the compositions under investigation, we have employed two-dimensional (2D) and three-dimensional (3D) plots. These plots were generated using the ELATE code [39]. Additionally, we have included a summary of all the elastic properties, including Young's modulus (Y), linear compressibility ($K=1/B$), shear modulus (G), and Poisson's ratio (ρ), along with their corresponding minimum and maximum values in Table 4.7. This table offers a comprehensive overview of the elastic properties of the analyzed materials and facilitates quick comparisons between different compositions. In Figures 4.26, 4.27, 4.28, and 4.29, we can observe the three-dimensional (3D) and two-dimensional (2D) diagrams representing the properties of $KTaO_{3-x}S_x$ compounds. A spherical shape in the plot, whether in 3D or 2D, indicates perfect isotropic behavior in the respective dimensional space. Conversely, any deviation from a spherical shape signifies varying degrees of anisotropy in different directions within the three-dimensional space. The same principle applies to the 2D case, where anisotropy is observed on specific crystal planes. The Young's modulus (Y), shear modulus (G), and Poisson's ratio (v) of these materials exhibit substantial anisotropy in all planes. However, for cubic crystals like $KTaO_3$ and $KTaS_3$, the linear compressibility of the material is isotropic, being the same in all directions, as depicted in Figures 4.26 and 4.29. In contrast, for $KTaO_2S$ and $KTaOS_2$, as shown in Figures 4.27 and 4.28, the linear compressibility displays pronounced anisotropic behavior in the *xz*- and *yz*-planes. At the same time, it demonstrates isotropic behavior in the *xy*-plane.

Table 4.7: The lower and upper limits of Young's modulus, compressibility, shear modulus, and Poisson's ratio of $ATaO_{3-x}S_x$ perovskites.

Phases	$Y_{\text{min.}}$ **(GPa)**	$Y_{\text{max.}}$ **(GPa)**	A_Y	K_{min} (TPa^{-1})	K_{max} (TPa^{-1})	A_K	$G_{\text{min.}}$ **(GPa)**	$G_{\text{max.}}$ **(GPa)**	A_G	$v_{\text{min.}}$	$v_{\text{max.}}$	A_v
$KTaO_3$	264.09	342.94	1.29	1.97	1.972	1.00	106.52	147.58	1.38	0.132	0.315	2.38
$RbTaO_3$	276.99	382.23	1.38	1.79	1.79	1.00	110.65	165.13	1.49	0.122	0.344	2.81
$CsTaO_3$	285.93	370.11	1.29	2.03	2.038	1.00	118.29	164.81	1.39	0.100	0.281	2.79
$KTaO_2S$	177.5	255.5	1.43	2.44	3.08	1.26	64.64	112.4	1.74	0.113	0.376	3.32
$RbTaO_2S$	154.84	261.73	1.69	2.62	2.96	1.12	56.00	113.43	2.02	0.095	0.449	4.72
$CsTaO_2S$	170.82	294.07	1.72	2.289	3.130	1.36	60.68	125.28	2.06	0.095	0.433	4.54
$KTaOS_2$	105.43	276.55	2.62	1.348	3.923	2.90	35.94	86.72	2.41	0.104	0.466	4.47
$RbTaOS_2$	105.29	187.2	1.77	3.72	4.34	1.16	36.13	82.473	2.28	0.080	0.457	5.65
$CsTaOS_2$	102.36	178.44	1.74	4.182	4.989	1.19	34.31	80.09	2.33	0.010	0.491	4.25
$KTaS_3$	125.25	177.05	1.41	3.316	3.316	1.00	48.46	73.38	1.51	0.157	0.394	2.50
$RbTaS_3$	116.61	211.93	1.81	3.191	3.191	1.00	44.374	91.201	2.05	0.100	0.480	4.78
$CsTaS_3$	120.2	140.04	1.16	4.154	4.154	1.00	48.07	57.91	1.20	0.186	0.296	1.59

(a) Young’s Modulus

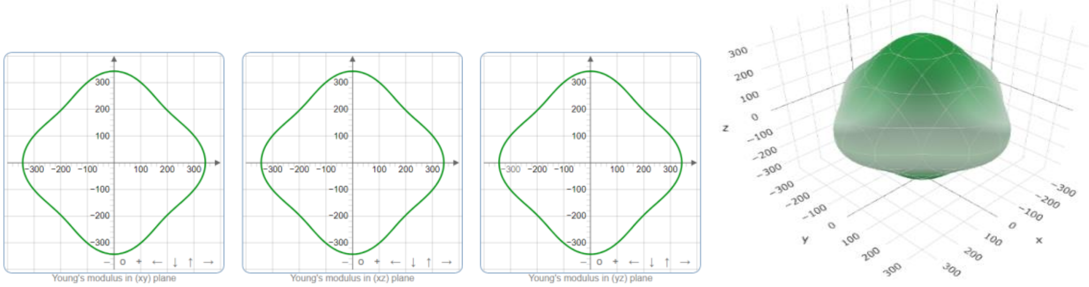

(b) Compressibility

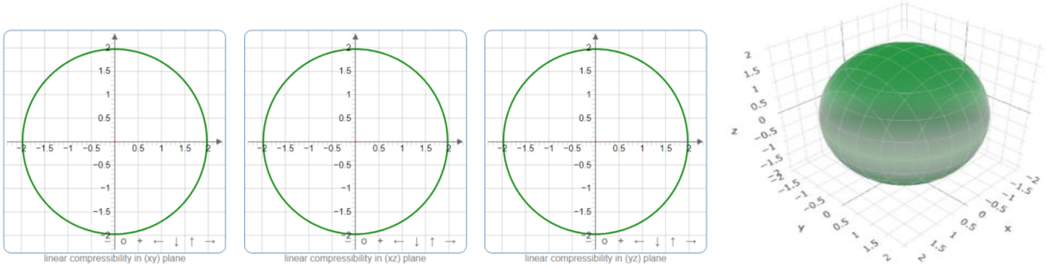

(c)Shear Modulus

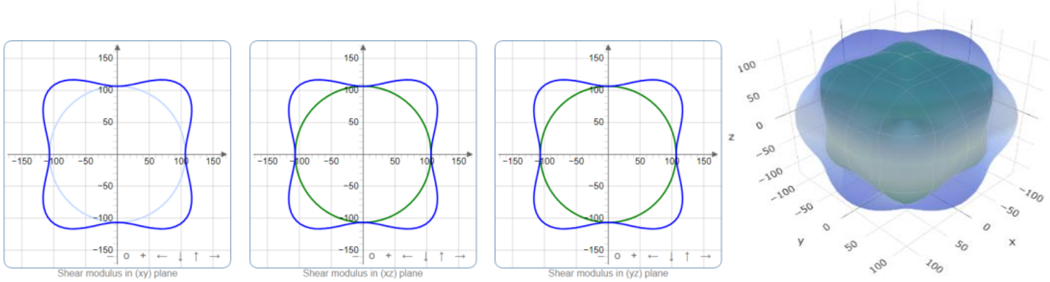

(d) Poisson’s ratio

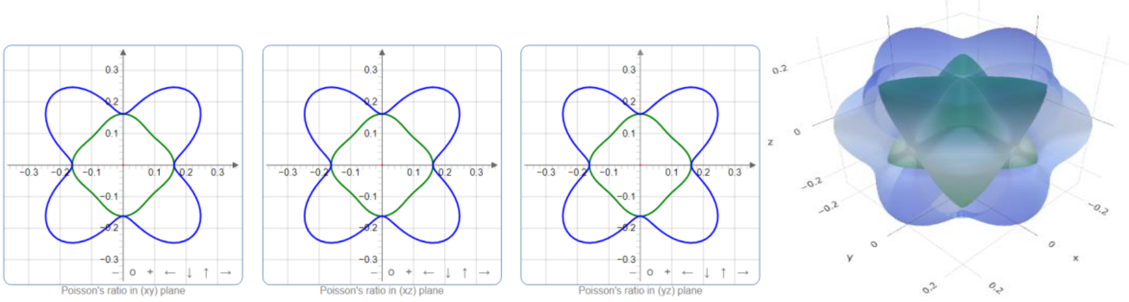

Figure 4.26: The 2D and 3D plots of (a) Y, (b) K, (c) G, and (d) υ of the $KTaO_3$ compounds.

(a) Young’s Modulus

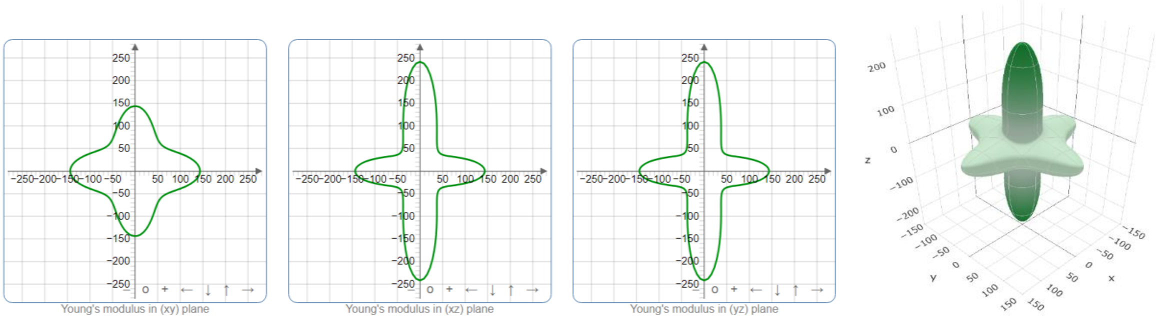

(c) Compressibility

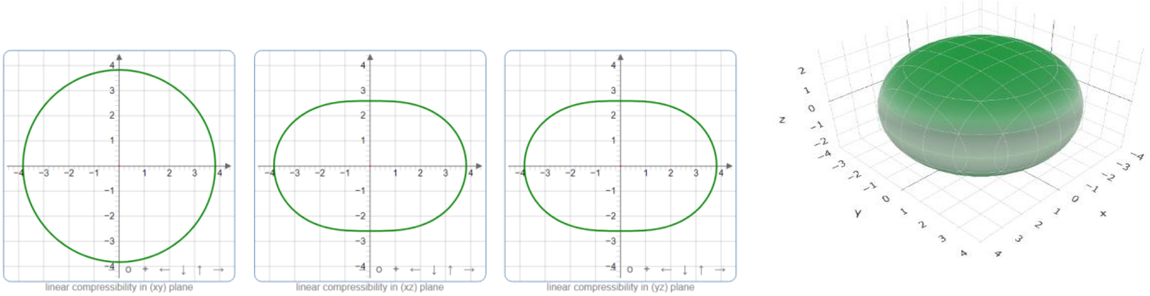

(c) Shear Modulus

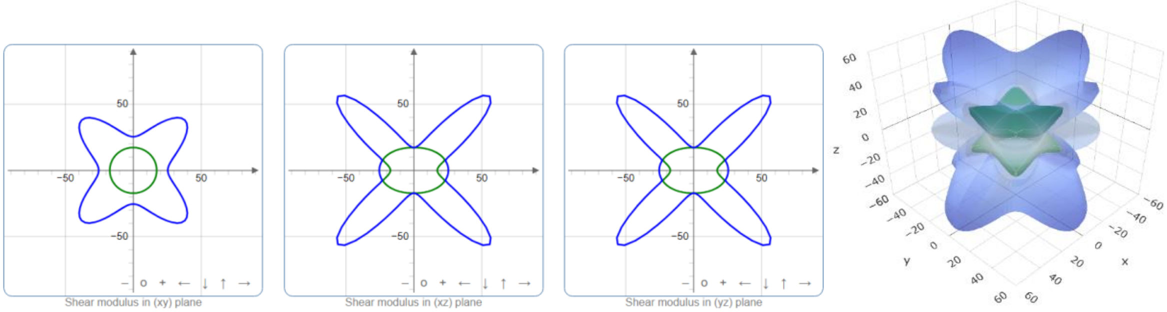

(d) Poisson’s ratio

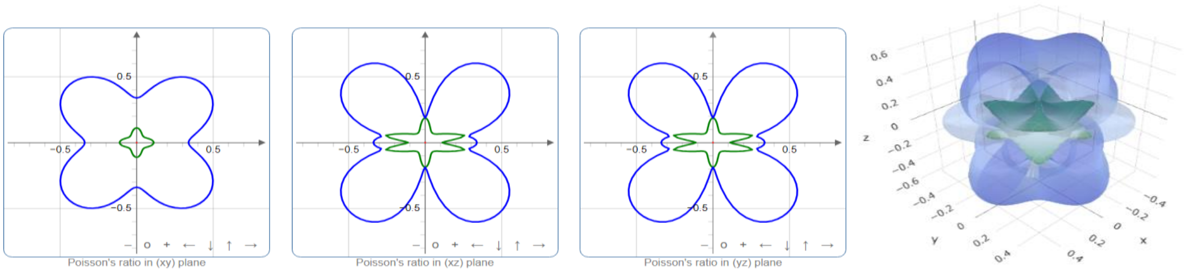

Figure 4.27: The 2D and 3D plots of (a) Y, (b) K, (c) G, and (d) υ of the $KTaO_2S$ compounds.

(a)Young's Modulus

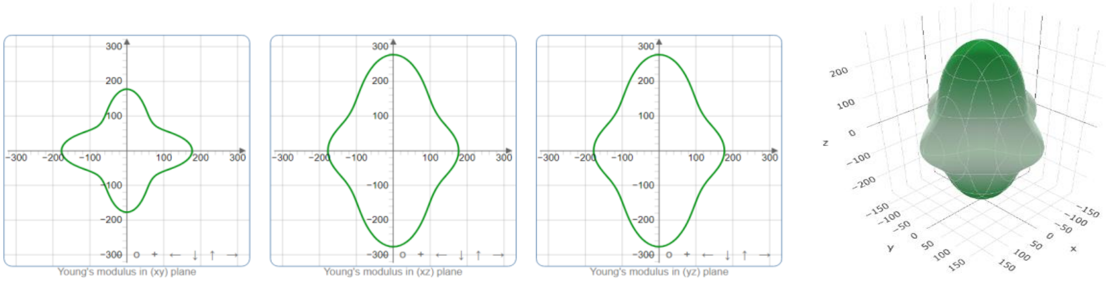

(b) Compressibility

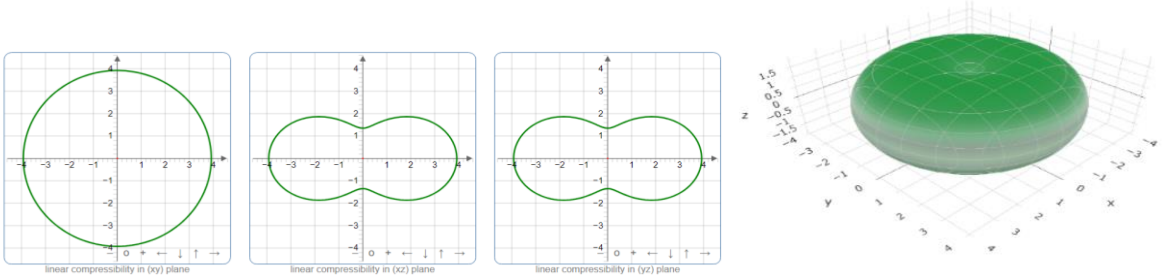

(c) Shear Modulus

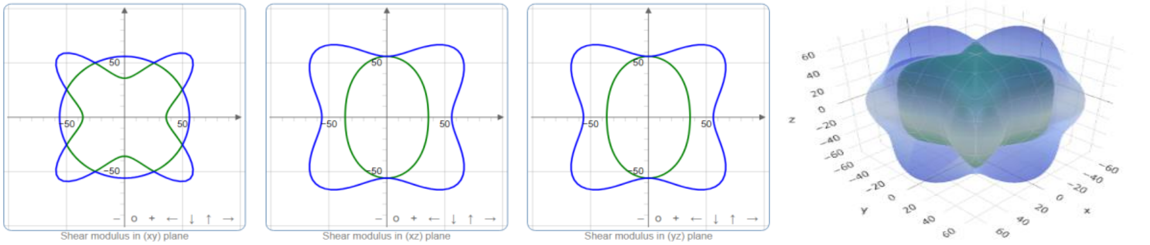

(d) Poisson's ratio

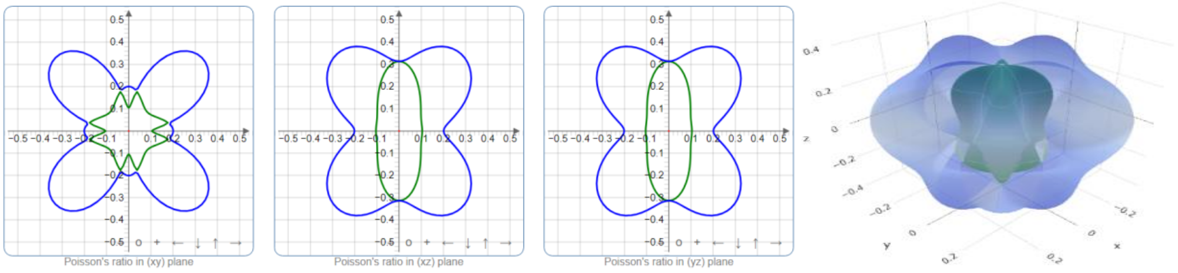

Figure 4.28: The 2D and 3D plots of (a) Y, (b) K, (c) G, and (d) υ of the $KTaOS_2$ compounds.

(a) Young’s Modulus

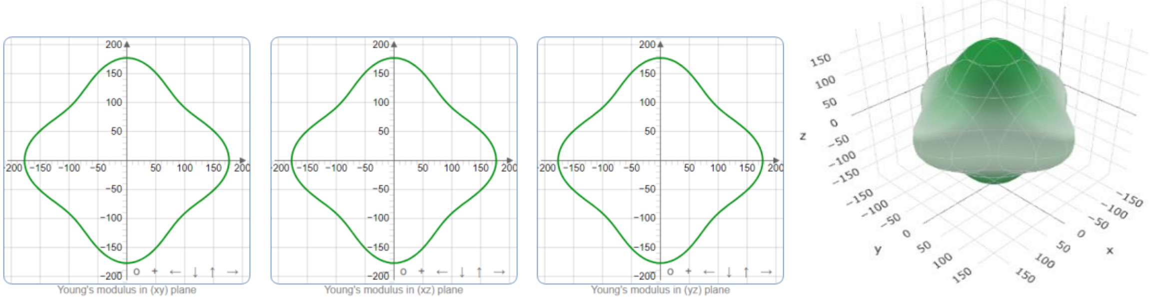

(b) Compressibility

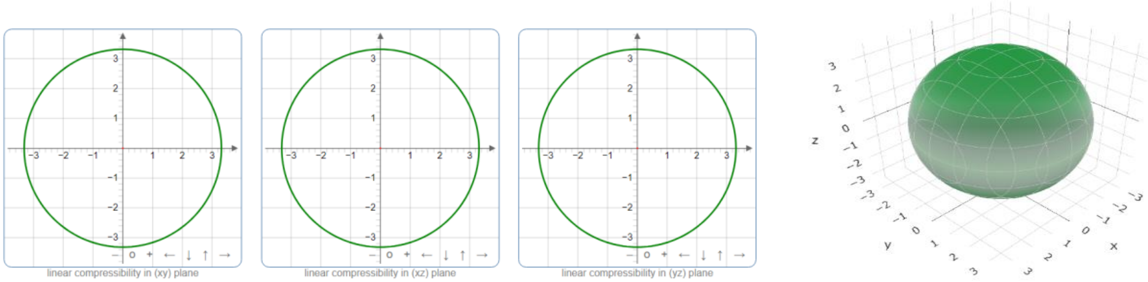

(c) Shear Modulus

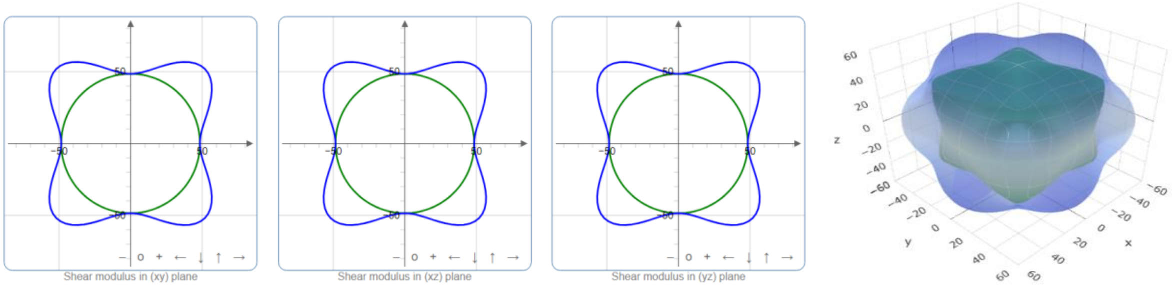

(d) Poisson’s ratio

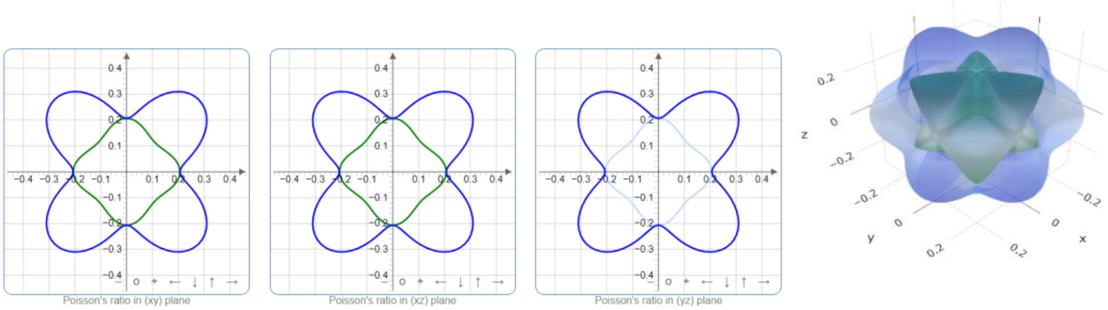

Figure 4.29: The 2D and 3D plots of (a) Y, (b) K, (c) G, and (d) υ of the $KTaS_3$ compounds.

4.6 Thermal Properties

This section comprehensively explores the fundamental thermodynamic properties related to $ATaO_{3-x}S_x$ compounds. The Debye temperature (θ_D) serves as a fundamental physical parameter intricately linked to various physical characteristics, including melting temperature, specific heat, and elastic constants. It plays a pivotal role in distinguishing the response of solids at high and low temperatures. When the temperature (T) exceeds the Debye temperature, all modes are expected to have energy levels roughly equivalent to K_BT. Conversely, when T falls below θ_D, high-frequency modes are anticipated to become frozen [40]. At lower temperatures, vibrational excitation primarily stems from acoustic modes. As a result, the Debye temperature, when computed from elastic constants, closely aligns with the value determined through specific heat measurements.

The computed Debye temperature, acoustic speeds, and density for the $ATaO_{3-x}S_x$ compound are presented in Table 4.8, where we compared the results obtained for the ordered unit cell with those of the supercell. The calculated values are reasonably consistent with the reported data [13] and exhibit good agreement with supercell calculation. Our findings suggest that substituting S results in a decrease in the Debye temperature. Typically, harder solids exhibit higher θ_D, and a low value of θ_D indicates lower lattice thermal conductivity and minimum thermal conductivity [41]. $ATaO_3$ has the highest θ_D values, while $ATaS_3$ has the lowest compared to the others.

The melting temperature of perovskite semiconductors is an important property that can impact their thermal stability and suitability for various applications, particularly those that involve high-temperature processing or operation. The obtained values for T_m are presented in Table 4.9. When we compare these calculated T_m values, we observe that $ATaO_3$ has a higher melting temperature compared to $ATaO_2S$, $ATaOS_2$, and $ATaS_3$ compounds. This suggests that $ATaO_3$ is well-suited for high-temperature applications.

This observation aligns with the behavior of Young's modulus, as T_m and Young's modulus exhibit a strong correlation.

Table 4.8: Calculated crystal density(ρ), transverse, longitudinal, and average sound velocities (v_l, v_t, and v_m), Debye temperature (θ_D) for $ATaO_{3-x}S_x$ compounds.

Compound	**ρ(kg/m^3)**	**ν_l(m/s)**	**ν_t(m/s)**	**ν_m(m/s)**	**Θ_D(K)**
$KTaO_3$	6788.94	6981.49	4228.76	4673.66	590.4
$RbTaO_3$	7695.15	6832.00	4109.52	4545.01	567.6
$CsTaO_3$	8457.68	6374.84	3997.02	4401.58	541.3
$KTaO_2S$	5601.99	6464.66	3809.03	4220.99	490.5
$KTaO_2S$ (SC)	5601.9	6420.2	3785.1	4194.2	487.2
$RbTaO_2S$	6370.7	5965.2	3513.4	3893.5	449.0
$RbTaO_2S$ (SC)	6370.7	6033.2	3512.0	3966.6	442.7
$CsTaO_2S$	6996.9	5966.2	3562.8	3943.2	448.7
$CsTaO_2S$ (SC)	6996.9	5653.5	3329.6	3689.8	419.7
$KTaOS_2$	4945.4	5916.8	3480.7	3857.7	422.2
$KTaOS_2$ (SC)	4945.8	5894.3	3431.3	3806.6	416.4
$RbTaOS_2$	5604.1	5394.2	3321.3	3664.6	398.6
$RbTaOS_2$ (SC)	5604.1	5481.7	3255.8	3605.2	391.9
$CsTaOS_2$	6175.6	5052.3	3166.9	3487.5	375.4
$CsTaOS_2$ (SC)	6175.6	5573.9	3110.4	3462.9	372.6
$KTaS_3$	4548.4	6235.3	3547.9	3943.8	412.5
$RbTaS_3$	5136.2	5981.4	3402.8	3782.6	393.7
$CsTaS_3$	5669.8	5131.3	3022.5	3349.5	345.8

Understanding the phonon transport properties is essential for comprehending a material's characteristics and predicting its practical applications in micro or nanotechnology. Lattice thermal conductivity (K_{ph}) is a critical factor in this context, as it describes how heat is conducted due to the contributions of phonons at various frequencies. Materials with lower thermal conductivity are often used as insulators, while phases with high K_{ph} find application in materials designed for efficient heat dissipation, such as heat sinks. The practical formula for calculating lattice thermal conductivity (K_{ph}) in $ATaO_{3-x}S_x$ considers heat conduction arising from the vibrations of lattice ions within a solid, originally developed by Slack [42]. Materials that exhibit high values of the Grüneisen parameter (γ) typically have substantial anharmonic contributions, resulting in low phonon thermal conductivity. The results of this study have indicated that all compositions of $ATaO_{3-x}S_x$ possess a moderate value of the Grüneisen parameter (γ), as shown in Table 4.9.

The results for $K_{\min}$ values are presented in Table 4.9. It is crucial to note that all these substances demonstrate low values of minimum thermal conductivity. The computed minimum thermal conductivity ($K_{\min}$) for our materials are as follows: $KTaO_3$ (1.16 W mK^{-1}), $RbTaO_3$ (1.10 W mK^{-1}), $CsTaO_3$ (1.03 W mK^{-1}), $KTaO_2S$ (0.88 W mK^{-1}), $RbTaO_2S$ (0.80 W mK^{-1}), $CsTaO_2S$ (0.79 W mK^{-1}), $KTaOS_2$ (0.71 W mK^{-1}), $RbTaOS_2$ (0.67 W mK^{-1}), $CsTaOS_2$ (0.62 W mK^{-1}), $KTaS_3$ (0.67 W mK^{-1}), $RbTaS_3$ (0.63 W mK^{-1}) and $CsTaS_3$ (0.55 W mK^{-1}). These values are comparable to those of widely recognized thermal barrier coating (TBC) materials like $Y_4Al_2O_9$ [43] and Yb_2SiO_5 [44].

In Fig. 4.30, we observe the temperature-dependent behavior of thermal conductivity (K_{ph}) for $ATaO_{3-x}S_x$. The findings reveal a distinct pattern in which K_{ph} undergoes a sharp decline in the temperature range of 0-1200 K, pursued by a more gradual decrease spanning 500-1800 K, ultimately stabilizing at a constant level at higher temperatures for $KTaO_{3-x}S_x$ compounds. In the case of $RbTaO_{3-x}S_x$ compounds, Kph demonstrates a sharp reduction in the 0-1000 K range, followed by a gradual decrease of 1000-2000 K, and ultimately reaches a constant value at elevated temperatures. Similarly, for $CsTaO_{3-x}S_x$ compounds, K_{ph} shows a notable decrease in the 0-1500 K range, followed by a gradual decline of 600-18000 K, and eventually stabilizes at a constant value at elevated temperatures. The specific values of K_{ph} can be found in Table 4.9.

Table 4.9: Calculated melting temperature (T_m), Grüneisen parameter (γ), lattice thermal conductivity (K_{ph}), minimum thermal conductivity (K_{min}), specific heat (C_v, C_p), and the thermal expansion coefficient (α) of $ATaO_{3-x}S_x$ perovskite compounds.

Phases	T_m	γ	K^*_{ph} (W/mK)	K_{min} (W/mK)	C_V	C_P	α ($10^{-6}k^{-1}$)
$KTaO_3$	2714.96	1.324	71.43	1.16	103	103.27	6.81
$RbTaO_3$	2952.95	1.349	72.31	1.10	104	104.81	6.18
$CsTaO_3$	2818.27	1.198	94.79	1.03	113	113.66	6.47
$KTaO_2S$	1580.16	1.426	40.78	0.88	108	109.29	8.11
$RbTaO_2S$	1470.88	1.426	36.11	0.80	114	114.52	8.58
$CsTaO_2S$	1605.65	1.374	44.71	0.79	106	106.88	6.91
$KTaOS_2$	1275.07	1.432	27.12	0.71	109	109.80	9.22
$RbTaOS_2$	1201.60	1.263	36.56	0.67	104	104.89	8.82
$CsTaOS_2$	1146.65	1.198	39.32	0.62	111	111.87	9.29
$KTaOS_3$	1725.21	1.549	24.40	0.67	112	113.43	8.34
$RbTaS_3$	1889.01	1.549	27.54	0.63	110	110.42	7.40
$CsTaS_3$	1483.49	1.426	22.85	0.55	115	115.69	9.43

$ATaO_3$ exhibits the highest lattice thermal conductivity owing to its high Debye temperature(θ_D). Among the materials under consideration, $KTaO_3$ demonstrates the highest lattice thermal conductivity. This can be attributed to its higher θ_D value and relatively low γ. A lower value of the Grüneisen parameter indicates reduced phonon scattering compared to the other three compounds.

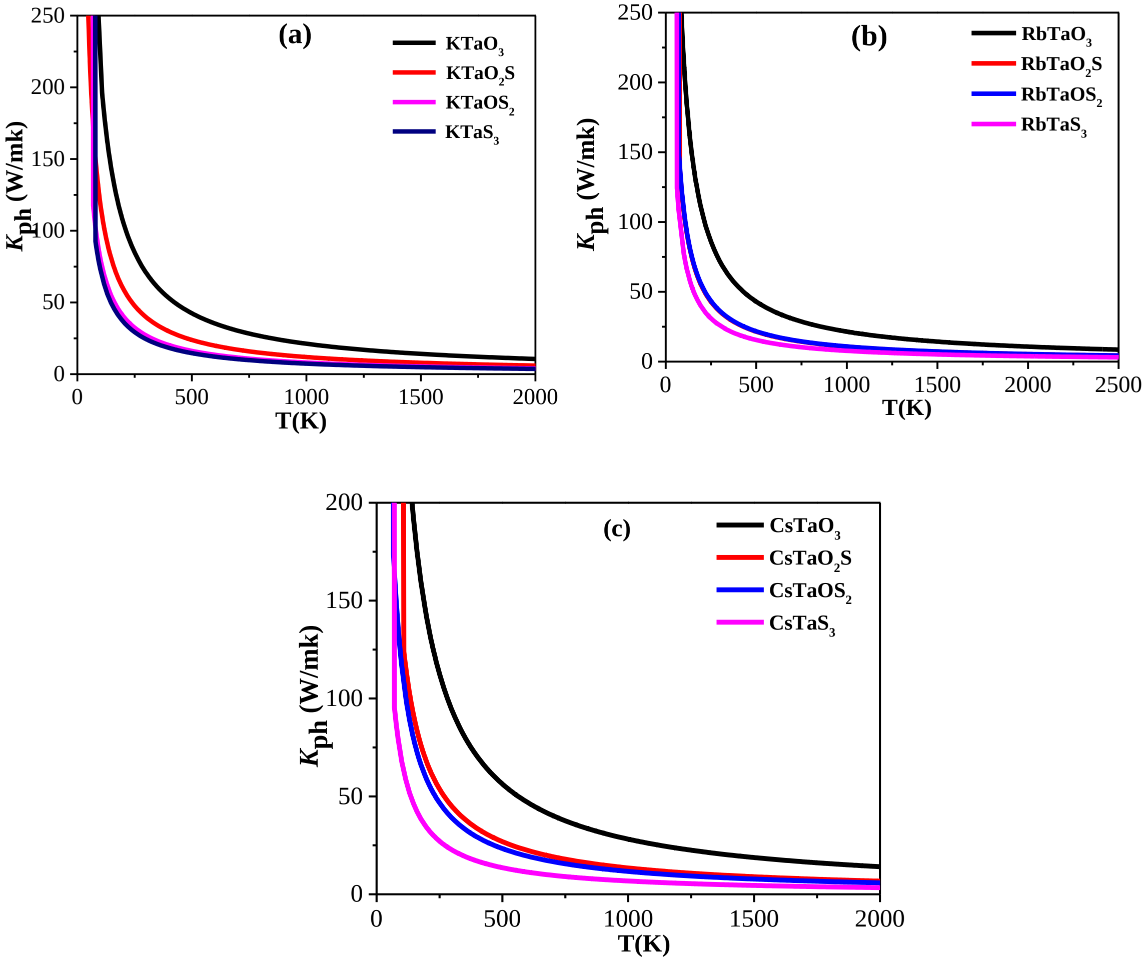

Figure 4.30: The temperature-dependent lattice thermal conductivity for (a) $KTaO_{3-x}S_x$, (b) $KTaO_{3-x}S_x$, and (c) $KTaO_{3-x}S_x$ compounds.

This value is comparable to other materials like B_6X (X = S, Se) [45], copper, aluminum alloys/aluminum, boron-aluminum, aluminum nitride, SiC, diamond, and certain other materials with thermal conductivity exceeding 145 W/mK [46]. These materials are widely recognized for their applications as heat sinks in laptops and various microelectronic devices that generate heat. It's worth mentioning that the estimated thermal conductivity (K_{ph}) at 300 K exceeds that of popular MAX phase compounds like bronze, and it's in a similar range as the thermal conductivity of aluminum bronze and red brass [46–48].

4.6.1 Specific heat and thermal expansion coefficient:

Specific heat is a vital thermal property essential in casting and heat treatment processes, determining the amount of heat required for these operations. It quantifies a substance's capacity to retain heat, with the provision of heat leading to a proportional temperature increase in the material. For temperatures above 300 K, the quasi-harmonic Debye model accurately explains the specific heat at constant volume (C_V). It considers the lattice vibrations of atoms and their anharmonicity, treating them as a collection of coupled harmonic oscillators [49–52] with variable volume. In Fig. 4.31, we can observe the temperature dependence of specific heats, C_v and C_p, within the range of 0-2000 K. The increase in specific heat with the temperature rise is called thermal softening. At temperatures lower than 600 K, the heat capacities follow the Debye T^3 power-law, whereas at temperatures exceeding 1000 K, they nearly conform to the Dulong-Petit (DP) model. It is common for solid materials that although C_v approaches the DP limit [53] at higher temperatures (1000 K), the DP model slightly underestimates C_p at these temperatures. However, the deviations of C_p values from the DP model for all titled compounds at 2000 K were always less than around 2.9-3.9%. Table 4.8 presented our calculated values of C_v and C_p for $ATaO_{3-x}S_x$.

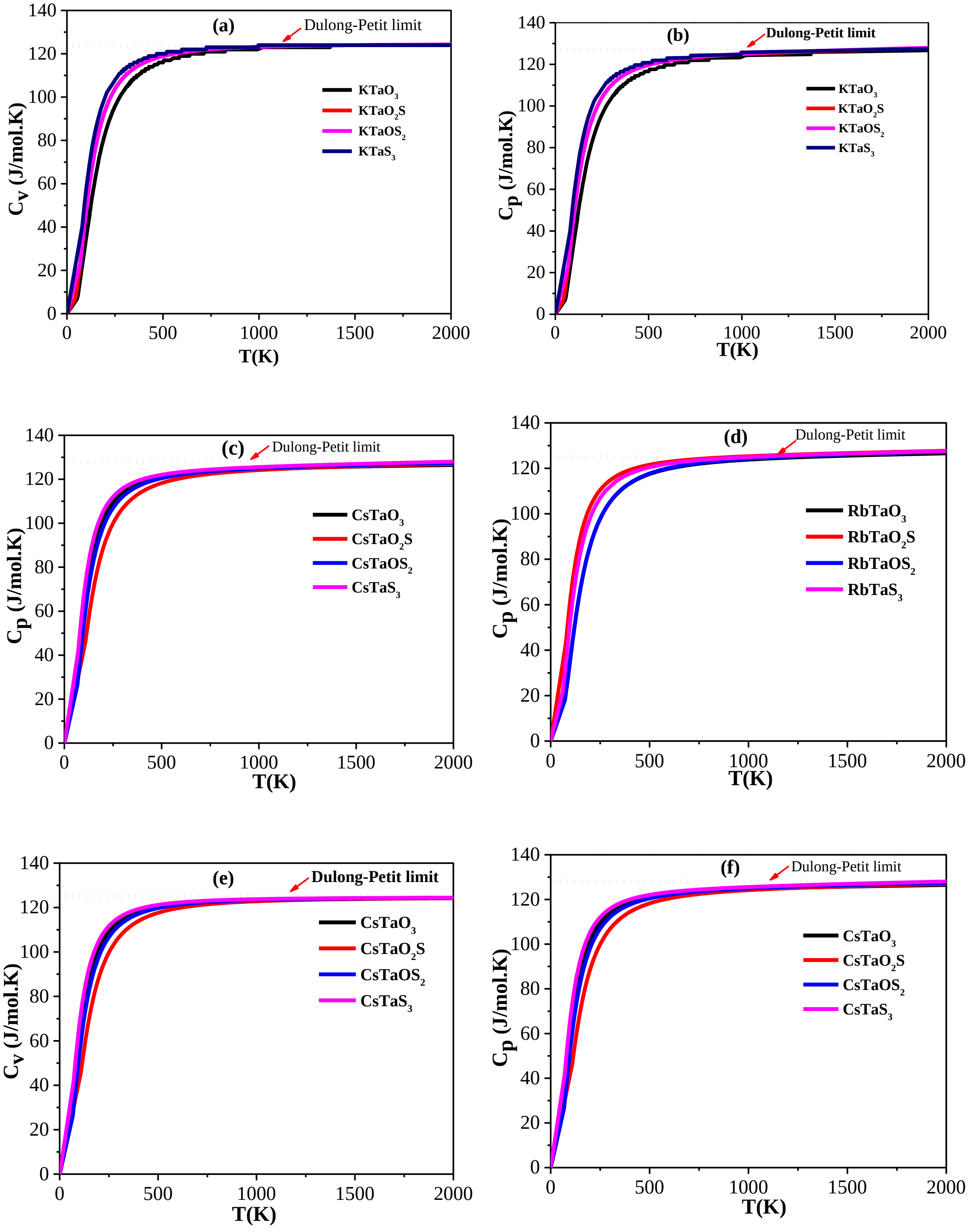

Fig. 4.31: The temperature-dependent specific heats for the $ATaO_{3-x}S_x$ solid solutions are reported in C_v at constant volume and C_p at constant pressure.

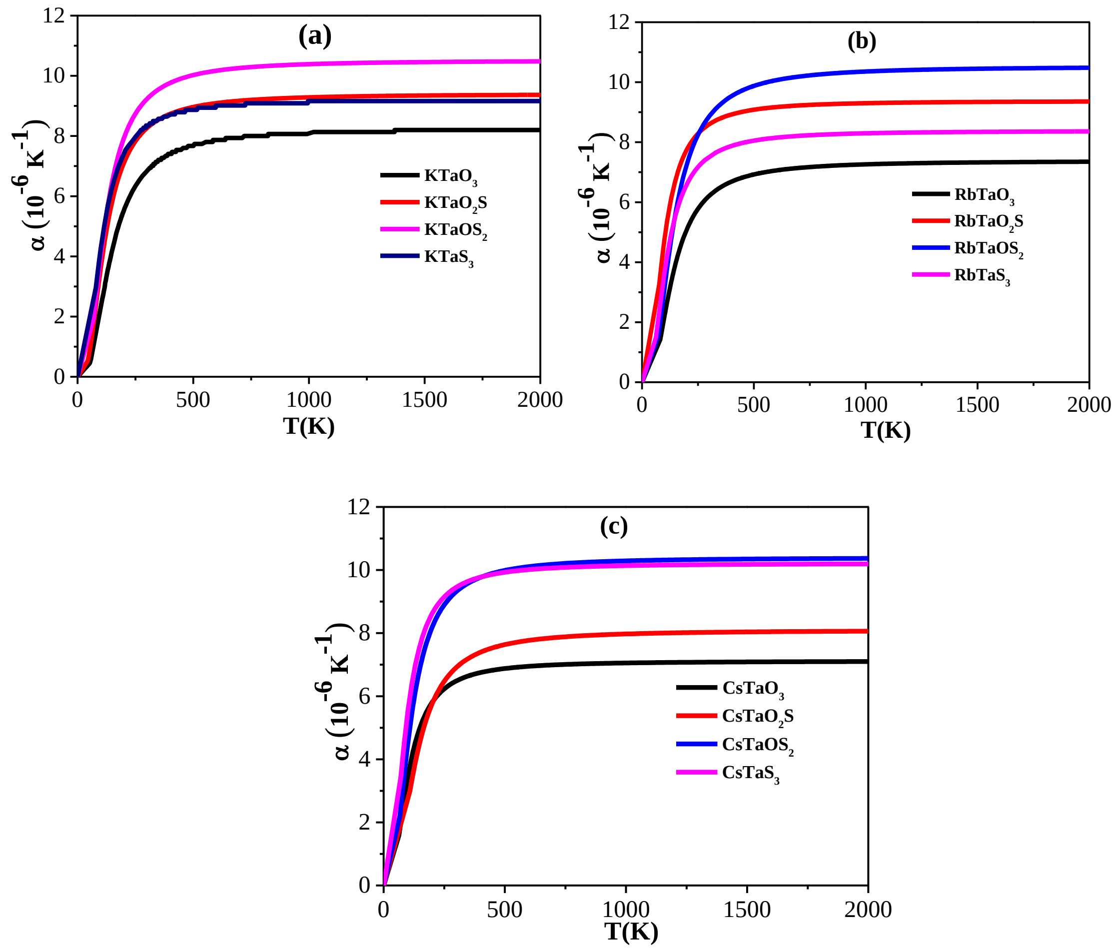

Fig. 4.32: Temperature-dependent linear thermal expansion coefficient (α) of (a) $KTaO_{3-x}S_x$, (b) $RbTaO_{3-x}S_x$, and (c) $CsTaO_{3-x}S_x$ compounds.

Fig. 4.32 illustrates the relationship between temperature and the coefficient of thermal expansion (α) for $ATaO_{3-x}S_x$ solid solutions. Our research shows that α rapidly increases until it reaches a specific temperature for $KTaO_{3-x}S_x$ compounds around 200 to 500 K; for $RbTaO_{3-x}S_x$ compounds, this increase occurs within the specified temperature range of 600 to 800 K, while for $CsTaO_{3-x}S_x$ compounds, the rise is evident in the temperature range of 100 to 400 K. Afterward, α gradually increases, reaching an almost constant value. At a temperature of 300 K, the coefficients of thermal expansion for these solid solutions are 6.81×10^{-6} K^{-1} for $KTaO_3$, 6.18×10^{-6} K^{-1} for $RbTaO_3$, 6.47×10^{-6} K^{-1} for $CsTaO_3$,

8.11×10^{-6} K^{-1} for $KTaO_2S$, 8.58×10^{-6} K^{-1} for $RbTaO_2S$, 6.91×10^{-6} K^{-1} for $CsTaO_2S$, 9.22×10^{-6} K^{-1} for $KTaOS_2$, 8.82×10^{-5} K^{-1} for $RbTaOS_2$, 9.29×10^{-6} K^{-1} for $CsTaOS_2$, 8.34×10^{-6} K^{-1} for $KTaS_3$, 7.40×10^{-5} K^{-1} for $RbTaS_3$ and 9.43×10^{-6} K^{-1} for $CsTaS_3$.

All of its thermal properties suggest that $ATaO_3$ emerges as a promising heat sink material because of its favorable linear thermal expansion coefficient (α), lattice thermal conductivity (K_{ph}), high melting point (T_m), and impressive minimum thermal conductivity (K_{min}). These characteristics position $ATaO_3$ as a strong contender for efficient heat dissipation applications. This is similar to another material, Ti_2BC [54], which has been predicted to have heat sink properties.

References

[1] Cabuk S, Akkus H, Mamedov AM. Electronic and optical properties of $KTaO_3$: Ab initio calculation. Physica B: Condensed Matter 2007;394:81–5. https://doi.org/10.1016/j.physb.2007.02.012.

[2] Sarwan M, Shukla P, Singh S. Structural stability, electronic and elastic properties of cubic $RbTaO_3$ perovskite oxide. AIP Conference Proceedings 2020;2265:030341. https://doi.org/10.1063/5.0017058.

[3] Berri S, Bouarissa N. First-principle calculations to investigate structural, electronic, optical, thermodynamic, and thermoelectric properties of ABO_3 (A=Cs, Rb and B= Ta, Nb) compounds. Emergent Mater 2022;5:1831–47. https://doi.org/10.1007/s42247-021-00324-0.

[4] Birch F. Finite Elastic Strain of Cubic Crystals. Phys Rev 1947;71:809–24. https://doi.org/10.1103/PhysRev.71.809.

[5] Murnaghan FD. The Compressibility of Media under Extreme Pressures. Proceedings of the National Academy of Sciences 1944;30:244–7. https://doi.org/10.1073/pnas.30.9.244.

[6] Vousden P. A study of the unit-cell dimensions and symmetry of certain ferroelectric compounds of niobium and tantalum at room temperature. Acta Cryst 1951;4:373–6. https://doi.org/10.1107/S0365110X5100115X.

[7] Jellison GE, Paulauskas I, Boatner LA, Singh DJ. Optical functions of $KTaO_3$ as determined by spectroscopic ellipsometry and comparison with band structure calculations. Phys Rev B 2006;74:155130. https://doi.org/10.1103/PhysRevB.74.155130.

[8] Hassan M, Liaqat M, Mahmood Q. Pressure dependence of electronic, optical and thermoelectric properties of $RbTaO_3$ perovskite. Appl Phys A 2021;127:287. https://doi.org/10.1007/s00339-021-04433-9.

[9] Baroni S, de Gironcoli S, Dal Corso A, Giannozzi P. Phonons and related crystal properties from density-functional perturbation theory. Rev Mod Phys 2001;73:515–62. https://doi.org/10.1103/RevModPhys.73.515.

[10] Togo A, Tanaka I. First principles phonon calculations in materials science. Scripta Materialia 2015;108:1–5. https://doi.org/10.1016/j.scriptamat.2015.07.021.

[11] lyorzor B. E ESO. Investigating the Effect of Hydrostatic Pressure on the Structural, Electronic, Mechanical, Lattice Dynamics and Optical Propert n.d. https://scholar.googleusercontent.com/scholar?q=cache:vB5Y9u3VnxgJ:scholar.google.com/+Iyorzor+B.+E.+et+al,+NIPES+J.+of+Sc.+and+Tech.+R.+4(2)+pp.324-333+(2022).&hl=en&as_sdt=0,5 (accessed October 3, 2023).

[12] Traoré B, Bouder G, Lafargue-Dit-Hauret W, Rocquefelte X, Katan C, Tran F, et al. Efficient and accurate calculation of band gaps of halide perovskites with the Tran-Blaha modified Becke-Johnson potential. Phys Rev B 2019;99:035139. https://doi.org/10.1103/PhysRevB.99.035139.

[13] Xu Y-Q, Wu S-Y, Zhang L-J, Wu L-N, Ding C-C. First-principles study of structural, electronic, elastic, and optical properties of cubic $KNbO_3$ and $KTaO_3$ crystals. Physica Status Solidi (b) 2017;254:1600620. https://doi.org/10.1002/pssb.201600620.

[14] Eng HW, Barnes PW, Auer BM, Woodward PM. Investigations of the electronic structure of d0 transition metal oxides belonging to the perovskite family. Journal of Solid State Chemistry 2003;175:94–109. https://doi.org/10.1016/S0022-4596(03)00289-5.

[15] Kato H, Kudo A. Water Splitting into H_2 and O_2 on Alkali Tantalate Photocatalysts $ATaO_3$ (A = Li, Na, and K). J Phys Chem B 2001;105. https://doi.org/10.1021/jp004386b.

[16] Sarwan M, Singh S. Theoretical analysis of structural stability and allied properties of new brittle perovskites: $RbTaO_3$ and $RbNbO_3$. Indian J Phys 2023;97:2061–76. https://doi.org/10.1007/s12648-022-02557-z.

[17] Shockley W, Queisser HJ. Detailed Balance Limit of Efficiency of *p-n* Junction Solar Cells. Journal of Applied Physics 1961;32:510–9. https://doi.org/10.1063/1.1736034.

[18] Tyunina M, Yao L, Chvostova D, Dejneka A, Kocourek T, Jelinek M, et al. Concurrent bandgap narrowing and polarization enhancement in epitaxial ferroelectric nanofilms. Sci Technol Adv Mater 2015;16:026002. https://doi.org/10.1088/1468-6996/16/2/026002.

[19] Liu JW, Chen G, Li ZH, Zhang ZG. Hydrothermal synthesis and photocatalytic properties of $ATaO_3$ and $ANbO_3$ (A=Na and K). International Journal of Hydrogen Energy 2007;32:2269–72. https://doi.org/10.1016/j.ijhydene.2006.10.005.

[20] Piskunov S, Kotomin EA, Heifets E, Maier J, Eglitis RI, Borstel G. Hybrid DFT calculations of the atomic and electronic structure for ABO_3 perovskite (001) surfaces. Surface Science 2005;575:75–88. https://doi.org/10.1016/j.susc.2004.11.008.

[21] Hussain MI, Khalil RMA, Hussain F, Imran M, Rana AM, Kim S. Investigations of structural, electronic and optical properties of TM-GaO_3 (TM = Sc, Ti, Ag) perovskite oxides for optoelectronic applications: a first principles study. Mater Res Express 2020;7:015906. https://doi.org/10.1088/2053-1591/ab619c.

[22] Novakovic R, Zivkovic D. Thermodynamics and surface properties of liquid Ga-X (X = Sn, Zn) alloys. J Mater Sci 2005;40:2251–7. https://doi.org/10.1007/s10853-005-1942-7.

[23] Kittel C. Introduction to Solid State Physics. John Wiley & Sons, Inc; 2005.

[24] Delerue C, Allan G, Niquet YM. Collective excitations in charged nanocrystals and in close-packed arrays of charged nanocrystals. Phys Rev B 2005;72:195316. https://doi.org/10.1103/PhysRevB.72.195316.

[25] Hilal M, Rashid B, Khan SH, Khan A. Investigation of electro-optical properties of InSb under the influence of spin-orbit interaction at room temperature. Materials Chemistry and Physics 2016;184. https://doi.org/10.1016/j.matchemphys.2016.09.009.

[26] Gao L-K, Tang Y-L. Theoretical Study on the Carrier Mobility and Optical Properties of $CsPbI_3$ by DFT. ACS Omega 2021;6:11545–55. https://doi.org/10.1021/acsomega.1c00734.

[27] Baikie T, Barrow NS, Fang Y, Keenan PJ, Slater PR, Piltz RO, et al. A combined single crystal neutron/X-ray diffraction and solid-state nuclear magnetic resonance study of the hybrid perovskites $CH_3NH_3PbX_3$ (X = I, Br and Cl). J Mater Chem A 2015;3:9298–307. https://doi.org/10.1039/C5TA01125F.

[28] Mosconi E, Umari P, Angelis FD. Electronic and optical properties of MAPbX3 perovskites (X = I, Br, Cl): a unified DFT and GW theoretical analysis. Phys Chem Chem Phys 2016;18:27158–64. https://doi.org/10.1039/C6CP03969C.

[29] Wu M, Yan K, Wang Y, Kang X. High crystallinity and photovoltaic performance of $CsPbI_3$ film enabled by secondary dimension. Journal of Energy Chemistry 2020;48:181–6. https://doi.org/10.1016/j.jechem.2020.01.009.

[30] Hussain Reshak A, Charifi Z, Baaziz H. Ab-initio calculation of structural, electronic, and optical characterizations of the intermetallic trialuminides $ScAl_3$ compound. Journal of Solid State Chemistry 2010;183:1290–6. https://doi.org/10.1016/j.jssc.2010.03.029.

[31] Yong-Qiang Xu. First-principles study of structural, electronic, elastic, and optical properties of cubic $KNbO_3$ and $KTaO_3$ crystals - Xu - 2017 - physica status solidi (b) - Wiley Online Library. https://onlinelibrary.wiley.com/doi/full/10.1002/pssb.201600620 (accessed October 3, 2023).

[32] Hill R. The Elastic Behaviour of a Crystalline Aggregate. Proc Phys Soc A 1952;65:349. https://doi.org/10.1088/0370-1298/65/5/307.

[33] Yan H, Wei Z, Zhang M, Wei Q. Exploration of stable stoichiometries, ground-state structures, and mechanical properties of the W–Si system. Ceramics International 2020;46:17034–43. https://doi.org/10.1016/j.ceramint.2020.03.290.

[34] Jhi S-H, Ihm J, Louie SG, Cohen ML. Electronic mechanism of hardness enhancement in transition-metal carbonitrides. Nature 1999;399:132–4. https://doi.org/10.1038/20148.

[35] Pugh SF. XCII. Relations between the elastic moduli and the plastic properties of polycrystalline pure metals. The London, Edinburgh, and Dublin Philosophical Magazine and Journal of Science 1954;45. https://doi.org/10.1080/14786440808520496.

[36] N FI. Elastic constants and elastic moduli of metals and insulators. Reference Book 1982.

[37] Music D, Sun Z, Ahuja R, Schneider JM. Electronic structure of M_2AlC (0001) surfaces (M = Ti,V,Cr). J Phys: Condens Matter 2006;18. https://doi.org/10.1088/0953-8984/18/39/017.

[38] Zener CM, Siegel S. Elasticity and Anelasticity of Metals. ACS Publications 2002. https://doi.org/10.1021/j150474a017.

[39] Gaillac R, Pullumbi P, Coudert F-X. ELATE: an open-source online application for analysis and visualization of elastic tensors. J Phys: Condens Matter 2016;28:275201. https://doi.org/10.1088/0953-8984/28/27/275201.

[40] Christman JR. Fundamentals of solid state physics. (No Title) n.d.

[41] Ali MA, Jahan N, Islam AKMA. Sulvanite Compounds Cu_3TMS_4 (TM= V, Nb and Ta): Elastic, Electronic, Optical and Thermal Properties using First-principles Method. J Sci Res 2014;6:407–19. https://doi.org/10.3329/jsr.v6i3.19191.

[42] Slack GA. The Thermal Conductivity of Nonmetallic Crystals. In: Ehrenreich H, Seitz F, Turnbull D, editors. Solid State Physics, vol. 34, Academic Press; 1979, p. 1–71. https://doi.org/10.1016/S0081-1947(08)60359-8.

[43] Zhou Y, Xiang H, Lu X, Feng Z, Li Z. Theoretical prediction on mechanical and thermal properties of a promising thermal barrier material: $Y_4Al_2O_9$. J Adv Ceram 2015;4:83–93. https://doi.org/10.1007/s40145-015-0140-6.

[44] Xiang H, Feng Z, Zhou Y. Mechanical and thermal properties of Yb_2SiO_5: First-principles calculations and chemical bond theory investigations. Journal of Materials Research 2014;29:1609–19. https://doi.org/10.1557/jmr.2014.201.

[45] Hossain MM, Ali MA, Uddin MM, Islam AKMA, Naqib SH. Origin of high hardness and optoelectronic and thermo-physical properties of boron-rich compounds B_6X (X = S, Se): A comprehensive study via DFT approach. Journal of Applied Physics 2021;129:175109. https://doi.org/10.1063/5.0047139.

[46] Ekpu M, Bhatti R, Ekere N, Mallik S. Advanced thermal management materials for heat sinks used in microelectronics. 18th European Microelectronics & Packaging Conference, 2011, p. 1–8.

[47] Ali MA, Hossain MM, Uddin MM, Hossain MA, Islam AKMA, Naqib SH. Physical properties of new MAX phase borides M_2SB (M = Zr, Hf and Nb) in comparison with conventional MAX phase carbides M_2SC (M = Zr, Hf and Nb): Comprehensive insights. Journal of Materials Research and Technology 2021;11:1000–18. https://doi.org/10.1016/j.jmrt.2021.01.068.

[48] Hadi MA, Kelaidis N, Naqib SH, Chroneos A, Islam AKMA. Mechanical behaviors, lattice thermal conductivity and vibrational properties of a new MAX phase Lu_2SnC. Journal of Physics and Chemistry of Solids 2019;129:162–71. https://doi.org/10.1016/j.jpcs.2019.01.009.

[49] Blanco MA, Francisco E, Luaña V. GIBBS: isothermal-isobaric thermodynamics of solids from energy curves using a quasi-harmonic Debye model. Computer Physics Communications 2004;158:57–72. https://doi.org/10.1016/j.comphy.2003.12.001.

[50] Delaire O, May AF, McGuire MA, Porter WD, Lucas MS, Stone MB, et al. Phonon density of states and heat capacity of $La_{3-x}Te_4$. Phys Rev B 2009;80:184302. https://doi.org/10.1103/PhysRevB.80.184302.

[51] Plirdpring T, Kurosaki K, Kosuga A, Day T, Firdosy S, Ravi V, et al. Chalcopyrite $CuGaTe_2$: A High-Efficiency Bulk Thermoelectric Material. Advanced Materials 2012;24:3622–6. https://doi.org/10.1002/adma.201200732.

[52] Xue L, Ren Y-M, He J-R, Xu S-L. First-principles investigation of the effects of strain on elastic, thermal, and optical properties of $CuGaTe_2$*. Chinese Phys B 2017;26:067103. https://doi.org/10.1088/1674-1056/26/6/067103.

[53] Sarwan M, Shukoor V A, Shareef M F, Singh S. A first principle study of structural, elastic, electronic and thermodynamic properties of Half-Heusler compounds; YNiPn (Pn=As, sb, and bi). Solid State Sciences 2021;112:106507. https://doi.org/10.1016/j.solidstatesciences.2020.106507.

[54] Islam R, M. Hossain M, Ali MA, M. Uddin M, H. Naqib S. Metallic boro-carbides of A_2BC (A = Ti, Zr, Hf and W): a comprehensive theoretical study for thermo-mechanical and optoelectronic applications. RSC Advances 2022;12:32994–3007. https://doi.org/10.1039/D2RA05448E.

Chapter 5: CONCLUSIONS

5.1 General:

Our systematic analysis of $ATaO_{3-x}S_x$ Perovskite semiconducting compounds, employing advanced first-principles methods, revealed intriguing insights. Sulfur substitution for oxygen induced structural transitions, from cubic to tetragonal and back to cubic phases. These compounds exhibited semiconducting behavior, with varying band gaps influenced by the S substitution. Remarkably high light-absorption capabilities were evident, particularly in $ATaO_2S$, making it a promising material for solar cell technology. Anisotropic optical properties and diverse mechanical behaviors were observed. Additionally, S substitution significantly impacted thermal properties. This research serves as a foundational reference for future explorations in advanced materials science, offering potential in renewable energy and various technological applications.

5.2 Key Findings:

5.2.1 Structural and Thermodynamic Stability:

Our research on $ATaO_{3-x}S_x$ perovskite semiconductors revealed some important things about their structure and stability. When we swapped out some oxygen with sulfur, the crystal structure changed, going from cubic to tetragonal shapes. We also figured out how stable these materials are by calculating their formation energies, showing which ones are more likely to form. For practical use, we looked at their dynamic stability by studying their phonon dispersions. The good news is that we didn't find any bad signs – no unstable vibrations – so these materials can handle some movement without falling apart. All of these findings are a solid starting point for more research and applications of these materials. They might have a bright future in material design and various technologies, showing their potential in the world of science and beyond.

5.2.2 Elastic Behavior and Mechanical Properties:

Elastic properties provide valuable insights into a material's ability to withstand stress and deformations, influencing its stability, strength, ductility, and more. For cubic crystals, our analysis showed that $ATaO_3$ and $ATaS_3$ satisfied the established elastic stability criteria, confirming their mechanical stability. Furthermore, for tetragonal crystals, the computed elastic constants met the criteria, illustrating the structural integrity of $ATaO_2S$ and $ATaOS_2$. Notably, the Poisson's ratio and Pugh's ratio concurred with these results, further affirming the mechanical characteristics of these compounds. We observed that the substitution of sulfur for oxygen influenced the mechanical properties, resulting in changes in bulk modulus, shear modulus, hardness, and shear resistance. Anisotropic characteristics were evident, with values like Poisson's ratio, shear modulus, linear compressibility and Young's modulus displaying varying anisotropy in different crystallographic directions. This anisotropy was particularly pronounced in $ATaO_2S$ and $ATaOS_2$, highlighting their complex mechanical behavior. Our study has provided comprehensive insights into the elastic and mechanical properties of $ATaO_{3-x}S_x$ compounds, shedding light on their stability, brittleness, ductility, and anisotropic behavior.

5.2.3 Optical and Electronic Properties:

In our comprehensive exploration of $ATaO_{3-x}S_x$ Perovskite semiconducting compounds, our focus on the electronic and optical properties has yielded significant key findings. These materials exhibit a clear semiconducting nature, as evident from the distinct band gap observed between valence and conduction bands around the Fermi level. The substitution of sulfur for oxygen leads to a decrease in the band gap, enhancing their suitability for electronic transitions. Our study also confirms the coexistence of ionic and covalent bonds within these compounds, as demonstrated by partial density of states and charge density plots. Notably, these materials showcase a remarkably high absorption coefficient and low reflectivity, making them exceptional candidates for applications that require efficient light absorption, notably in solar cell technology.

5.2.4 Thermal Characteristics:

Our thorough analysis of $ATaO_{3-x}S_x$ Perovskite compounds, thermal properties has uncovered pivotal insights. Sulfur substitution resulted in a notable decrease in the Debye temperature, indicative of altered thermal characteristics. This led to reduced minimum thermal conductivity and lattice thermal conductivity. The compounds exhibited moderate anharmonicity as indicated by the Grüneisen parameter. When considering factors such as linear thermal expansion coefficient (α), lattice thermal conductivity (K_{ph}), minimum thermal conductivity (K_{min}), and melting point (T_m), $ATaO_3$ (A = K, Rb, Cs) stands out as a promising candidate for efficient heat sink materials.

5.3 Limitations of the Study

While our investigation of $ATaO_{3-x}S_x$ compounds highlights their potential for applications like solar cell technology, recognizing certain limitations is crucial. This study predominantly concentrated on particular compositions, and the findings are based on theoretical calculations without experimental validation. A more comprehensive exploration of a wider compositional space would provide a fuller understanding of these materials. Additionally, experimental work is essential to verify the predicted properties. These limitations open avenues for future research to further uncover the vast potential of $ATaO_{3-x}S_x$ compounds.

5.4 Practical Implication

Our discovery of $KTaO_2S$ and $RbTaO_2S$ as an exceptional material for solar cell technology, with its exceptional light absorption properties and low reflectivity, holds significant promise for advancing the field of renewable energy. This finding offers the potential for cost-effective and more efficient solar cell designs, playing a role in the transition toward sustainable energy sources. Additionally, our insights into the electronic properties and band gap modification through S substitution offer a route for custom-tailoring semiconductors for various electronic and optoelectronic applications. Furthermore, the characterization of mechanical behavior, anisotropic properties, and thermal characteristics equips materials scientists and engineers with essential data for selecting and designing materials in fields such as structural engineering, optics, and heat management. Overall, our research provides a valuable reference for future experimental endeavors, underpinning the development of novel materials and technologies with improved functionality and efficiency.

5.5 Recommendation for Further Study

This comprehensive investigation of $ATaO_{3-x}S_x$ Perovskite semiconducting compounds has unveiled valuable insights into their multifaceted properties. As we move forward, it is essential to recommend avenues for further research to expand upon our findings. Firstly, experimental validation of our theoretical predictions is imperative to confirm the practical feasibility of these materials as well as theoretical calculation on the measurement of the energy conversion efficiency and thermoelectric properties. Additionally, exploring a broader range of compositions within the $ATaO_{3-x}S_x$ system will provide a more comprehensive understanding of their properties. Investigating the potential applications of these compounds, such as their use in solar cell technology. Lastly, a deeper exploration of the anisotropic characteristics and their impact on practical applications is warranted. These recommendations aim to propel the field of advanced materials science and technology and further unlock the potential of $ATaO_{3-x}S_x$ compounds.